GEOLOGICA ULTRAIECTINA

Mededelingen van het
Instituut voor Aardwetenschappen der
Rijksuniversiteit te Utrecht

No. 47

THE NARS ARRAY

A SEISMIC EXPERIMENT IN WESTERN EUROPE

BERNARD DOST

STELLINGEN

-1-

Toepassing van a priori informatie in de "stacking" procedure, gebruikt by de analyse van oppervlaktegolven, leidt tot verbetering van de identificatie van individuele boventonen van oppervlaktegolven, niet tot een nauwkeuriger bepaling van fase- of groepssnelheid van goed geidentificeerde boventonen.

-2-

Metingen van fasesnelheden van grond- en boventonen van Love golven in West-Europa zijn tot dusver onbetrouwbaar.

Cara, M., Nercessian, A. and Nolet, G., 1980.
Geophys. J. R. Astron. Soc., **61** , 459-478.
Dit proefschrift

-3-

Een mogelijke inversie van de dichtheid op een diepte van ca. 220 km (Nolet, 1977) wordt niet gevonden onder het Westeuropees platform.

Nolet, G., 1977.
Z. Geophys., **43,** 265-286.
Cara et al., 1980
Dit proefschrift

-4-

Het ontbreken van een lage snelheidslaag voor "S"- golven en de aanwijzingen voor de aanwezigheid van een lage dichtheidslaag op een diepte tussen 200 en 350 km diepte onder het Scandinavische schild zijn in overeenstemming met de tectosphere hypothese.

Jordan, T. H., 1978.
Nature., **274,** 544-548.
Dit proefschrift

-5-

By de interpretatie van aardmodellen, bestaande uit gegevens over de "S"- snelheid en dichtheid, in termen van mineralogie verdient het de voorkeur ontbrekende informatie omtrent elastische parameters van mantel-mineralen als onbekende te beschouwen in plaats van te vertrouwen op extrapolatie van bekende gegevens.

-6-

Micro-electronica wordt sneller ontwikkeld dan getest.

-7-

De hoeveelheid problemen die onstaat bij niet-gestandaardiseerde douanehandelingen is evenredig aan het aantal verdragen tussen de landen in kwestie.

-8-

Het aantal projecten dat gestimuleerd wordt door de Europese Gemeenschap is geen maat voor de de bereidheid tot samenwerking van de diverse landen.

-9-

Met het verdwijnen van studierichtingen door toedoen van de huidige bezuinigingsgolf rijst de vraag of de aanduiding Universiteit in de betekenis van "het geheel der wetenschappen" nog wel op zijn plaats is.

-10-

De kritiek dat popmuziek inhoudsloos zou zijn wordt weerlegd door teksten als: "brown shoes don't make it" (*F. Zappa*).

Utrecht, 13 mei 1987 B. Dost

Stellingen behorende bij het proefschrift: "The NARS array".

GEOLOGICA ULTRAIECTINA

Mededelingen van het
Instituut voor Aardwetenschappen der
Rijksuniversiteit te Utrecht

No. 47

THE NARS ARRAY

A SEISMIC EXPERIMENT IN WESTERN EUROPE

THE NARS ARRAY

A SEISMIC EXPERIMENT IN WESTERN EUROPE

HET NARS ARRAY

EEN SEISMISCH EXPERIMENT IN WEST-EUROPA

(met een samenvatting in het Nederlands)

PROEFSCHRIFT

TER VERKRIJGING VAN DE GRAAD VAN DOCTOR IN DE WISKUNDE EN NATUURWETENSCHAPPEN AAN DE RIJKSUNIVERSITEIT TE UTRECHT, OP GEZAG VAN DE RECTOR MAGNIFICUS PROF. DR. J.A. VAN GINKEL VOLGENS BESLUIT VAN HET COLLEGE VAN DEKANEN IN HET OPENBAAR TE VERDEDIGEN OP WOENSDAG 13 MEI 1987 DES NAMIDDAGS TE 12.45 UUR

DOOR

BERNARD DOST

GEBOREN OP 15 JANUARI 1956 TE HAARLEM

PROMOTOR: PROF. DR. A.M.H. NOLET

voor Wil en de beestenboel

The research described in this thesis was carried out at the:

Institute of Earth Sciences,
Department of Theoretical Geophysics
PO. Box 80.025
3508 TA Utrecht
The Netherlands

SUMMARY

Due to the rapid development of portable, digital seismographs it has recently become possible in global seismology to install and operate a large scale temporary array of seismic stations. This thesis describes the design and operation of the first experiment of this kind: the Network of Autonomous Recording Stations (NARS). The aim of NARS is to measure the dispersion of surface waves, especially higher modes, and to obtain through linearized inversion a shear-velocity and density model for the upper mantle under the West European platform. The existence of such a regional model opens the possibility to test different current hypotheses about the structure and composition of the upper mantle. Inversion of previous measurements of the dispersion of surface waves in Western Europe resulted in an average model for the West European platform including the Scandinavian shield. Combination of the measurements presented in this thesis with the older dataset opens the possibility to investigate differences between the shield and platform structure.

In the first chapter the design and a technical description of a NARS station is given. Furthermore NARS installation and operation is discussed. Inadequate sampling due to instrument failures and absence of strong Japanese/Kurile events at intermediate depth, which excite most efficiently higher mode surface waves, are the main sources of error in the presented dispersion measurements. These facts motivated us to develop methods to enhance the signal to noise ratio in the stacking technique applied to separate higher modes of surface waves.

An inventory of possibile methods to obtain this enhancement followed by a test of the proposed methods on a synthetic dataset is the subject of chapter 2. Introduction of a priori information in the stacking procedure increases the signal to noise ratio and facilitates the identification of a mode, but does not improve the average error in the phase velocity determination of higher mode Rayleigh waves. However, the use of the CLEAN-algorithm in removing disturbing aliasing lobes from well excited modes, is demonstrated to produce a bias in phase velocity measurements at frequencies greater than 35 mHz.

Chapter 3 describes the dataset that has been collected by the NARS array and could be used in the stacking procedure. In addition phase velocity measurements for fundamental and higher Rayleigh and Love waves are presented. Higher mode Rayleigh wave phase velocities could be obtained in the frequencyband of 20-70 mHz, an extension of 30 mHz to the high frequency part with respect to earlier measurements, and fundamental mode phase velocities from 6-50 mHz. Because of the very limited amount of reliable transverse components, the Love wave phase velocity dataset has been rejected for further use in the inversion procedure. An independent dataset, consisting of Sn traveltimes from selected European events and recorded by European stations, is presented in order to constrain the shear velocity in the uppermost mantle.

Inversion of the phase velocity dataset is the subject of chapter 4. A detailed shear velocity and density model for the West European platform has been obtained. Major features are a high velocity lid from 80-140 km depth, followed by a pronounced low velocity zone between 160 and 220 km depth. The transition zone (400-650 km depth) is characterized by high shear velocity values with respect to a reference Earth model (PREM). Density shows a positive gradient coinciding with the high velocity lid, followed by a constant value down to the 400 km discontinuity. No low density zone is resolved. Combination of Nolet's (1977) higher mode phase velocity dataset for the West European platform and Scandinavian shield and the present phase velocities for the platform structure resulted in a model for the Scandinavian shield. Remarkable features are the absence of a low velocity layer, low velocities compared to the platform model in the upper part of the transition zone and low densities between 200 and 350 km depth.

The final chapter 5 gives an interpretation of the models discussed in chapter 4 in terms of mantle mineralogy. Interpretation of the platform model in terms of pyrolite or piclogite is not conclusive. Density, especially around the 400 km discontinuity, indicates that the pyrolite model is to be preferred. The high velocity layer associated with an increase in density is interpreted as an eclogite layer. The existence of this layer can be explained by the lithospheric doubling concept. Difference in structure between platform and shield, possibly down to 500 km depth, strongly supports the tectosphere hypothesis.

SAMENVATTING

Dankzij de snelle ontwikkeling van draagbare, digitale seismografen is in de globale seismologie de mogelijkheid geschapen om een tijdelijk netwerk van seismische stations te installeren en daarmee een experiment op grote schaal uit te voeren.
Dit proefschrift beschrijft de opzet en uitvoering van het eerste experiment dat met een dergelijk tijdelijk netwerk is uitgevoerd: het Netwerk van Autonoom Registrerende Stations (NARS).
Het doel van het hier beschreven experiment is om een gedetailleerd S-snelheids en dichtheids model voor het Westeuropees platform te verkrijgen door middel van inversie van dispersiemetingen van grondtoon en (met name) boventonen van oppervlaktegolven. Een zo verkregen regionaal model voor de bovenmantel kan gebruikt worden om heersende theorieen omtrent structuur en compositie van de bovenmantel te toetsen. Inversie van eerdere metingen van de dispersie van oppervlaktegolven in West-Europa leverde een gemiddeld model op van het Westeuropees platform en het Scandinavisch schild. Combinatie van deze eerdere metingen met de huidige geeft de mogelijkheid om verschillen tussen beide regio's te onderzoeken.

De opzet, het technisch ontwerp en de uitvoering van NARS is beschreven in hoofdstuk 1. Het ontbreken van sterke aardbevingen op intermediaire diepte, die een optimale excitatie van de boventonen geven, en het frequent ontbreken van data uit NARS-stations die tijdelijk defect geraakt waren, zijn de belangrijkste oorzaken van fouten in de dispersie metingen.
Dit heeft geleid tot de ontwikkeling van methoden om de signaal-ruis verhouding te vergroten in het stacking-algorithme dat gebruikt wordt om boventonen van elkaar te scheiden. Een inventarisatie van mogelijkheden hiertoe en een test op een synthetische dataset is het onderwerp van hoofdstuk 2. Introduktie van a priori kennis in de analyse geeft een belangrijke verhoging van de signaal-ruis verhouding, waardoor verschillende boventonen gemakkelijker te identificeren zijn, maar verkleint niet de gemiddelde fout in de metingen. Aangetoond wordt dat het CLEAN-algorithme, dat iteratief het effect van een niet optimale stationsbedekking corrigeert, fouten introduceert voor frequenties groter dan 35 mHz.
Een overzicht van de door NARS geregistreerde aardbevingen die gebruikt konden worden in de analyse staat in hoofdstuk 3. Ditzelfde hoofdstuk behandelt tevens de fasesnelheids metingen van grond- en boventonen van Rayleigh en Love golven. Fasesnelheden van Rayleighgolven worden gepresenteerd in de frequentieband van 20-70 mHz voor de boventonen en van 6-50 mHz voor de grondtoon. Dit is een extensie van 30 mHz naar hogere frequenties met betrekking tot eerdere metingen in West-Europa. Vanwege de geringe hoeveelheid betrouwbare transversale componenten en de grote spreiding in de gemeten fasesnelheden van Love-golven, zijn deze niet meegenomen in de inversie procedure. Een onafhankelijke dataset bestaande uit looptijden van Sn-golven, afkomstig van Europese aardbevingen en

geregistreerd door Europese stations, is geintroduceerd om de S-snelheid in het bovenste deel van de bovenmantel vast te leggen.
Het onderwerp van hoofdstuk 4 is de inversie van de in hoofdstuk 3 gepresenteerde dataset. Een gemiddeld model voor het Westeuropees platform wordt gekarakteriseerd door een zone met hoge snelheden tussen 80 en 140 km diepte, gevolgd door een geprononceerde lage snelheidslaag tussen 160 en 220 km diepte. De overgangszone (400-650 km diepte) bevat hoge snelheden ten opzichte van een referentie aardmodel (PREM). De dichtheid geeft een positieve gradient te zien die samenvalt met de zone van hoge snelheid, gevolgd door een gebied met een nagenoeg konstante dichtheid tot 400 km diepte. Er is geen aanwijzing voor een lage dichtheidslaag. Vergelijking met data van Nolet (1977) voor platform en schild tesamen resulteerde in een model voor het Scandinavisch schild. Opvallend is het ontbreken van een lage snelheidslaag, lagere snelheden ten opzichte van het platform model in het bovenste deel van de transitiezone en lagere waarden in dichtheid van ca. 200 tot 350 km diepte.
In hoofdstuk 5 wordt een mineralogische interpretatie van deze snelheids en dichtheidsmodellen gegeven. Er kan geen uitsluitsel gegeven worden omtrent de vraag of het platform model een pyrolitische ofwel een piclogitische samenstelling heeft. De dichtheid, en wel speciaal de dichtheidssprong bij de 400 km discontinuiteit, geeft echter aanwijzingen dat het pyroliet model de voorkeur geniet. De hoge snelheidszone van 80 tot 140 km diepte, die gepaard gaat met een verhoging van de dichtheid, wordt geinterpreteerd als een eclogietlaag. De aanwezigheid van deze laag kan verklaard worden door middel van de lithosfeerverdubbelings hypothese. Verschillen in structuur tussen platform en schild, mogelijk tot op 500 km diepte, zijn in overeenstemming met de tectosfeer hypothese.

CONTENTS

SUMMARY I
SAMENVATTING III
CONTENTS V
INTRODUCTION VII

PART 1: THE NETWORK

Chapter 1: DESCRIPTION OF THE NARS ARRAY 1

1.1 NARS system design 1
1.2 Instrumentation 3
1.2.1 Seismometers 3
1.2.2 Pre-Amplifier-filter 4
1.2.3 Digital event recorder 7
1.2.4 Time receiver 7
1.2.5 System response 9
1.3 System calibration 12
1.4 NARS installation and operation 15
1.4.1 Organisation 16
1.4.2 Installation 16
1.4.3 Data processing 18
1.4.4 NARS performance 20
1.5 Conclusion 24

PART 2: ANALYSIS OF HIGHER MODES OF SURFACE WAVES

Chapter 2: RESOLUTION ENHANCEMENT USING A PRIORI KNOWLEDGE 25

2.1 Optimum weights 27
2.2 Fourier estimators incorporating a priori information 33
2.3 Comparison of algorithm performance 36

Chapter 3: ANALYSIS OF NARS DATA 47

3.1 Data 47
3.2 Measurements 58
3.2.1 Higher mode surface wave measurements 58
3.2.2 Traveltimes 68

Chapter 4: INVERSION 71

4.1 Inversion for the West European platform 72
4.2 Inversion for the Scandinavian Shield 79

Chapter 5: INTERPRETATION AND CONCLUSIONS 83

5.1 Mineralogical models 83
5.2 Models involving mechanical properties 88
5.3 Petrological interpretation 89
5.4 Conclusions 92

Appendix A 94
Appendix B 96
Appendix C 98
Appendix D 104
References 110
Acknowledgements 115
Curriculum Vitae 117

INTRODUCTION

Layered models of the deep upper mantle structure summarize information on the average structure of the sampled region. Although there is a growing tendency in seismology to shift focus to laterally heterogeneous models and their implications for the dynamic and kinematic processes of plate tectonics, simplified models with horizontal layers shall continue to be useful for several reasons. First of all they may provide much-needed evidence for petrologic models of the upper mantle, especially in relatively undisturbed areas like the West European platform. Secondly, the density in the upper mantle is still badly constrained, and even the simple layered models coming from surface wave analyses may constitute an important step forward. Thirdly these layered models are needed as a starting model in more detailed studies, e.g. in linearized or non-linear waveform fitting (Lerner-Lam & Jordan, 1983; Nolet et al., 1986d), or as a description of the background medium in body wave (Malin & Phinney, 1985) and surface wave scattering calculations (Snieder, 1986). For the West European platform no deep layered model is available at present. A study by Mayer-Rosa and Mueller (1973) provided such a model for south West Europe derived from fundamental mode Rayleigh wave phase velocities and P and S delay times. The deep mantle models that have been derived from inversion of fundamental and higher mode Rayleigh wave phase velocities (Nolet, 1977) and Love and Rayleigh wave fundamental and higher mode phase velocities (Cara et al, 1980) averaged over platform and shield. Recently tomographic studies using longitudinal body waves (Spakman, 1986) give detailed pictures of the upper mantle structure. Shear wave tomography, however, has not yet produced accurate results.

Surface wave dispersion is mainly dependent on the shear wave velocity and density structure of the traversed medium, if one assumes the medium to be isotropic. Nolet (1977) showed that linearized inversion of higher mode phase velocities, taking averaged measurements from 7 events, for shear velocity alone did not produce accurate earth models. Addition of the density in the inversion resulted in the appearence of a low density layer starting at 190 km depth. However, resolution was not sufficient to constrain this low density layer and its existence was questioned by Cara et al. (1980) who took a subset of Nolet's data and added a Love wave dataset. The main reasons for this bad resolution are:

[a] In order to obtain data from a large enough number of stations, both Nolet (1977) and Cara et al. (1980) average over a heterogeneous structure;

[b] both used analogue WWSSN recordings are used with digitization errors increasing with frequency;

[c] the large separation between WWSSN stations leads to disturbing spatial aliasing effects so that phase velocity measurements could only be obtained at frequencies < 40 mHz.

If one wishes to measure higher-mode surface wave dispersion without the incorporation of a priori knowledge in the form of a starting model, stacking techniques should be applied. The higher mode stacking techniques developed by Nolet (1975,1977) and Cara (1978) require the existence of a dense, quasi-linear array of seismic stations. In an analysis of measurement errors in higher-mode phase velocity determinations, Nolet and Panza (1976) find that the largest source of errors is the interference of different modes with roughly the same group velocity combined with an inadequate array-response. Precision largely depends on the array span, which determines the width of the mainlobe of the array response function, and station density. Addition of temporary digital stations to the existing WWSSN network should improve the higher-mode dataset considerably.

Based on these conclusions and the wish to sample a geological unit like the West European platform, the Network of Autonomous Recording Stations (NARS; Nolet and Vlaar, 1982) was initiated. This thesis describes the design and set-up of the network, which consists of 14 digital, portable, 3 component stations located in a linear array from south Sweden to southern Spain. This gives a total array length of 2600 km, or an average station separation of 200 km. The array acts as an antenna directed towards the Kuriles/Japan region and was designed to deliver high quality data and a higher mode phase velocity dataset in the frequency range of 20-70 mHz.

The final aim of the research described in this thesis is to obtain a detailed picture of the average West European platform structure by measuring the dispersion of higher mode surface waves and increase the vertical resolution of shear velocity and density with respect to earlier studies. This enables us to test different hypotheses regarding the constitution of the upper mantle.

NARS is the Dutch contribution to the European Geotraverse (EGT).

PART 1: THE NETWORK

1. DESCRIPTION OF THE NARS ARRAY

For many years seismological observatories have been equipped with non-mobile seismometers and analogue recording. Maintenance could only be carried out by qualified personnel. A common seismic station consisted of a seismometer- galvanometer system, producing an output on photographic paper or ink-recorders. With the development of portable seismometers and, more recently, the replacement of galvanometers by an electronic amplifier-filter system (Wielandt and Mitronovas, 1976) and the introduction of commercially produced digital event recorders with triggered recording, it became possible to carry out a large scale seismic experiment using portable stations. In this chapter we will describe the NARS system design and give detailed technical information about the instrumentation. Furthermore we will discuss the operation of the array and the data processing in Utrecht. Because of recent developments in developing a large broad-band portable network in the US (IRIS, 1984b) and in Europe (Nolet et al., 1986c) a brief overview of our operational experience with the NARS instrumentation is included. For the upgrading of the WWSSN network (IRIS, 1984a) operational experience from the IDA network has recently been reviewed (Agnew et al., 1986). Parts of this chapter have been published in Dost et al. (1984) and Nolet et al. (1986a).

1.1. NARS SYSTEM DESIGN

The NARS instrumentation was selected with the following requirements in mind:

[a] The array should record large earthquakes with a good signal to noise ratio at 3 components. Since the aim of the network is to study Earth structure, not seismicity, we are not interested in events of small magnitude (m_b <6);

[b] The frequency band should include surface waves in the period range between 10 and 200 mHz, and give broad-band (< 2 Hz) recordings of body waves;

[c] Digital recording and a large dynamic range is necessary to allow for sophisticated data analysis techniques. Seismic signals of interest have a dynamic range of at least 120 dB;

[d] Mobility and ease in maintenance is required to make the network multi-purpose and low-cost.

From [b] a lower limit for the Nyquist frequency was determined (f_N= 4 Hz) to avoid aliasing. This means a minimum sampling rate of 8 samples per second. Continuous digital

recording at this sampling rate, however, implies approximately 1.1 Mbyte of data per channel per day. No event recorder was commercially available in 1981 that could store these large data volumes if we assume that point [d] requires station servicing at most once every week. In view of this we opted for triggered recording and a sampling rate of 125 msec.

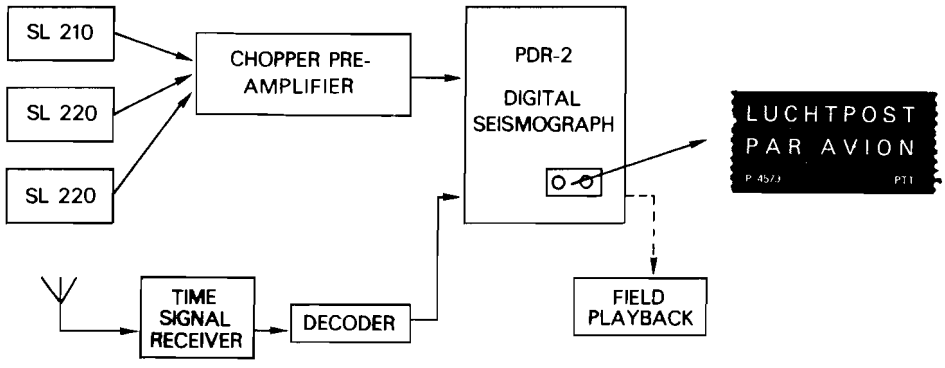

Figure 1.1.1 NARS station configuration

NARS station configuration is shown in figure 1.1.1. The central element of each station is formed by a Kinemetrics PDR-2 datalogger and 3 long period seismometers: one Teledyne Geotech SL 210 (vertical) and two SL-220 (horizontals). Matching the output of these seismometers to the PDR-2 necessitated the introduction of a pre-amplifier to take full advantage of the dynamic range of the PDR-2 (114 dB). The seismometers can be tuned to an eigenperiod of 10 to 30 seconds, but become increasingly unstable at longer periods. This made us decide to tune the seismometers to a 12 seconds eigenperiod and to introduce a response shaping filter after the pre-amplifier to enlarge the frequency band towards low frequencies. This pre-amplifier-filter was designed and built in the department of theoretical geophysics together with Arie van Wettum, who also built a time receiver for regular calibration of the internal PDR-2 quartz clock.

1.2 NARS INSTRUMENTATION

1.2.1. Seismometers

The history of the development of portable long period seismometers shows a large effort to diminish the length of the spring of the vertical sensor and weight of the mass. With the introduction of the zero-initial length spring the portable seismometer could be realized. Both vertical and horizontal seismometers can be tuned to a specific eigenperiod by tilting the base of the instruments. This tilting results in a change of the gravity component in the plane of motion by $\cos\theta$, where θ is the angle between the boom and the vertical (see e.g. Aki & Richards, 1980 pp 482-485). If the seismometer base is placed in a horizontal position ($\theta=\frac{\pi}{2}$) one can, theoretically, acquire an infinite eigenperiod. In practice there is a finite range of eigenperiods where the instruments are stable. For NARS this region is between 10 and 30 seconds. We can write the relation between eigenperiod and equivalent mathematical spring length as:

$$T = 2\pi \left(\frac{l}{g\cos\theta}\right)^{1/2} \tag{1.1}$$

where l denotes spring length [m], g gravity constant [ms^{-2}] and T the eigenperiod [s]. For 10 seconds eigenperiod the equivalent spring length ($l/\cos\theta$) is 25 m, but for 30 seconds the equivalent spring length is 225 m. Since the seismometer reacts to tilts of the base and extension of the spring, e.g. due to temperature fluctuations, as if the dimensions of the instrument are equal to the mathematical equivalent lengths (Willmore, 1979), one has to decide to tune the seismometers to a low eigenperiod for sake of stability, in our case 12.0 seconds.

The seismometer transferfunction (in Vm^{-1}) as function of complex circular frequency $s=i\omega$, defined as a response to a signal e^{+st} is given by:

$$T(s) = \frac{s^3 S}{s^2+2s\omega_0 h_0+\omega_0^2} = \frac{s^3 S}{(s-z_1)(s-z_2)}; \quad z_{1,2} = -\omega_0 h_0 \pm i\omega_0(1-h_0^2)^{1/2}$$

$$\omega_0 = 0.524\text{Hz} \qquad h_0 = 1. \tag{1.2}$$

S is the main coil constant in Vm^{-1}/Hz and is specified by the manufacturer to be $S=90\pm4$ Vm^{-1}/Hz for the vertical instrument (SL-210), and $S=93\pm4$ Vm^{-1}/Hz for the horizontal instrument (SL-220).

1.2.2. Pre-Amplifier-filter

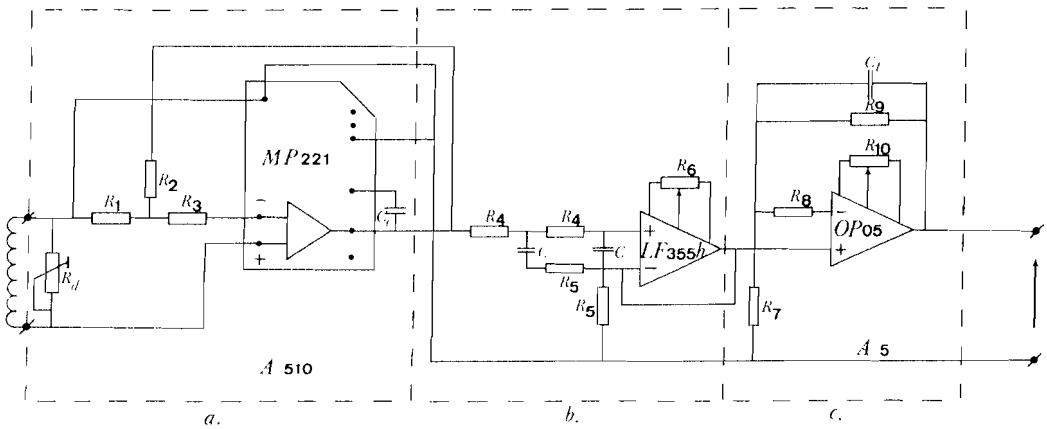

Figure 1.2.1 Pre-amplifier/filter circuit diagram. For explanation see text.

The pre-amplifier-filter can be divided into three parts (see figure 1.2.1):

[a] Pre-Amplifier,

[b] Response shaping filter,

[c] Additional amplification.

In order to take full advantage of the large dynamic range of the PDR-2 (114 dB) a pre-amplifier was needed. The gain of this pre-amplifier is chosen in such a way that clipping occurs for an Italian event of magnitude 7 or a magnitude 8 teleseismic event. This gain factor has a value of approximately 40. Introduction of the shape response filter, however, (see figure 1.2.3) decreases the signal level for frequencies higher than 0.1 Hz with a factor of about 65. A total gain of approximately 2600 should therefore be applied. If we apply this gain before filtering, the voltage after amplification can exceed the voltage of the

power supply of the chopper amplifier (±15V). This will introduce distortion of the signal. For this reason we restricted the amplifier gain to 510 before and 5 after filtering. A detailed description of the system, illustrated by figure 1.2.1, is as follows;

[a] *Pre-amplifier*

A central position is taken by the Analogic MP 221 chopper amplifier, with a specified noise level from DC to 1 Hz of less than 100 nV peak to peak and a drift less than 50nV/°C. R_d takes care of the critical damping of the seismometer. R_1 and R_2 determine the gain:

$$gain = \frac{R_1+R_2}{R_1}$$

and R_3 is used to diminish the DC offset. An offset error voltage is generated by the bias current flowing through the summing impedance of R_1 and R_2. If we choose:

$$R_3 = \frac{R_1 R_2}{R_1 + R_2}$$

it compensates the offset, provided the source impedance is much less than R_1. C_c is a compensation capacity, used to limit the bandwidth of the system. This is important because output noise generated by the amplifier varies as the square root of the bandwidth. Its value has been calculated from the empirical formula:

$$C_c = \frac{30}{gain} \cdot \frac{100}{f} \quad [\mu F]$$

where f is the cut-off frequency in Hz. This equation is determined by the manufacturer. Our choise of C_c, see table 1.1, is based on a cut-off frequency of 15-20 Hz (in reality f= 17.8 Hz).

[b] *Response shaping filter*

In Appendix A the transfer function of a general second order filter is shown to be:

$$\frac{U_u}{U_i} = \frac{Y_1 Y_2}{Y_1 Y_2 + Y_4(Y_1+Y_2+Y_3)} \tag{1.3}$$

U_u and U_i denote respectively the output and input voltage and Y_i admittance. If we identify Y_1 and Y_2 with R_4^{-1} (see figure 1.2.1) and Y_3 and Y_4 with sC one obtains the well-known formula of a biquadratic low-pas filter:

$$\frac{U_u}{U_i} = \frac{\omega_0^2}{s^2+2s\,\omega_0 h_1+\omega_0^2}\ ,\ \omega_0 = \frac{1}{R_4 C} \tag{1.4}$$

Incorporation of resistance R_5 in Y_3 and Y_4 results in an additional high pass filter.
In this case $Y_3 = Y_4 = \frac{sC}{1+sR_5C}$ and:

$$\frac{U_u}{U_i} = \frac{s^2+2s\,\omega_0 h_0+\omega_0^2}{s^2+2s\,\omega_1 h_1+\omega_1^2} \cdot \frac{\omega_1^2}{\omega_0^2} \tag{1.5}$$

where $\omega_1 = \frac{1}{(R_4+R_5)C}$, $h_1 = 1$, $\omega_0 = \frac{1}{R_5 C}$, $h_0 = 1$.
The total response of the system consisting of seismometer and shaping filter is equal to the product of (1.2) and (1.5). If we choose ω_0 in (1.5) to be identical with the eigenfrequency of the seismometer (ω_0 in (1.2)) we can change the eigenfrequency of the seismometer to any desired value ω_1.

[c] *Additional amplification*

Instead of a chopper amplifier we use for the second amplifying stage an OP05 operational amplifier. The offset problem is handled in the same manner as in [a]. C_t is introduced to cut off high frequencies, far outside the passband of the total system. Its value can be determined by:

$$C_t = \frac{1}{2\pi R_9 f}\ [\mathrm{F}]$$

f is the cut-off frequency in Hz, resistance in Ohm. The choise of C_t, displayed in table 1.1, implies a cut-off frequency of 39 Hz.

Table 1.1: Component values

R_1	.110 kΩ	R_2	56 kΩ
R_3	.110 kΩ	R_4	10000 kΩ
R_5	1400 kΩ	R_6	20 kΩ
R_7	6.8 kΩ	R_8	5.1 kΩ
R_9	27.2 kΩ	R_{10}	25 kΩ
R_d	3.8 kΩ		
C	1400 nF	C_c	330 nF
C_t	150 nF		

1.2.3. Digital event recorder

The PDR-2 digital event recorder is a low power multi-microcomputer based seismic data acquisition system. It operates with a triggering mechanism based on Short Term Average (STA) and Long Term Average (LTA) determination of the input signal. The parameter settings used are shown in table 1.2.
A Kinemetrics CTU-1 play back unit is used for station servicing in the field and for a rough impression on paper of the data on cassette tapes that arrive in Utrecht. To inspect data in the field for e.g. parity errors a Tandy TRS-80 model 100 portable microcomputer is used. Data can be transmitted from the PDR-2 to the Tandy computer in the field at 9600 Baud. To accomplish this the commands from the TRS-80 to the PDR-2 are given through an RS-232 interface, but the data from the PDR-2 to the TRS-80 are received via the cassette recorder entrance.

Table 1.2: PDR-2 parameter setting and general features

3 channel recording
125 msec sample period
Trigger:
- STA/LTA ratio; no LTA update
- Only effective at vertical component
- STA = 4 s; LTA = 128 s
- STA/LTA treshold = 4; Post event treshold = 2
- Post event time = 8*128 s

All channels have auto gain ranging.
Anti alias filter (2nd order Butterworth): -3dB point = 1.0 Hz
Sample: 12 bit mantisse and 3 bit exponent
Total number of samples per tape: 920.000 (app. 10 hours of data)
Recording :
- Standard 300 ft, 1667 bpi digital cassettes
- Blocks of 3072 samples (=6144 bytes)
- Header 114 bytes

1.2.4. Time receiver

Since our sampling rate is 125 msec, the clock precision needed is 63 msec or less. The PDR-2 can be equipped with a GOES-satellite time receiver, but signals from this satellite can not be received in Europe. We therefore had to build a time receiver ourselves and used a design published in Elektuur (Anonymus, 1981) that only needed a minor modification in order to synchronize the internal PDR-2 quartz clock. The role of this

instrument in the total system is shown in figure 1.2.2. By means of an active antenna a coded time signal emitted by the DCF-77 station in Frankfurt is received.

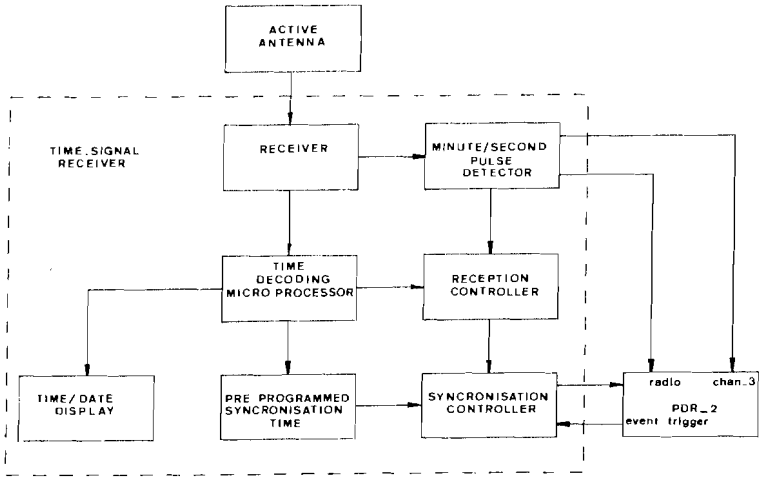

Figure 1.2.2 Block diagram of the function of the time-receiver in connection with the PDR-2.

At stations far away from Frankfurt an extra loop antenna is used, consisting of a coil (diameter of 107 cm, 78 windings) and capacitor (5-7 pF), tuned to 77.5 kHz. This increases the signal to noise ratio. The signal is decoded in a microprocessor unit and the time is shown on a display. With a modification of the PDR-2 we succeeded in establishing an automatical adjustment of the PDR-2 clock at pre-programmed time intervals. This procedure synchronizes the clock to the nearest second; in consequence the clock drift must not be more than 0.5 seconds between subsequent synchronizations. To check for larger drift a minutemark is superposed on the seismic signal, on the East-West channel, during the first two minutes before each triggering. Since the first two recorded minutes of each event consist only of microseismic noise, no signal of interest is disturbed by this procedure. In practice the drift of the internal PDR-2 clock can be more than 63 msec per week. Therefore the automatic time calibration is done twice a day (at 23.00 and 4.00 GMT) if reception is good and no earthquake is being recorded.

1.2.5. System response

The total system response is equal to the product of the individual responses of the seismometer, pre-amplifier/filter and anti-alias filter. The total transfer function $T(s)$ for displacement becomes:

$$T_D(s) = \frac{As^3}{\prod_{m=1}^{4}(s - z_m)} \quad [\frac{\text{Counts}}{\text{m}}] \tag{1.6}$$

$z_1 = (-.063, 0.i)$ rad/s $\qquad z_2 = (-.063, 0.i)$ rad/s

$z_3 = (-4.443, 4.443i)$ rad/s $\qquad z_4 = (-4.443, -4.443i)$ rad/s

$A = 1.23 * 10^{10} \quad [\frac{\text{Counts}}{\text{m}}/\text{Hz}]$

Comparison with other broad-band systems, e.g. the Graefenberg array (Seidl & Stammler, 1984), is simplified by showing the amplitude response to ground velocity in Vm^{-1}/Hz as well as the phase response in degrees and group delay in seconds. The transfer function $T_V(s)$ for velocity then becomes:

$$T_V(s) = \frac{T_D(s)}{Ds} \tag{1.7}$$

where D translates Volts to Counts (D= 104857.6 Counts/Volt). Figure 1.2.3 shows results. The main differences between the NARS and Graefenberg responses are compiled in table 1.3

Table 1.3 Comparison of broad-band systems

Parameter	Graefenberg	NARS
Gain	2400 Vs/m	3450 Vs/m
High frequency -3dB point	5.0 Hz	1.0 Hz
slope	42 dB/octave	12 dB/octave
Low frequency -3dB point	.05 Hz	.01 Hz
slope	12 dB/octave	12 dB/octave

NARS is in general more sensitive to the lower frequencies and has only a 2^{nd} order anti-alias filter compared to a 7^{th} order for the Graefenberg instruments. Seidl & Stammler (1984) show that the anti-aliasing filter determines mainly the leading edge of the onset of a phase on the seismogram. The use of a 7^{th} order anti-aliasing filter may introduce an apparent delay in the arrival time of 0.1 second at a noise level of 10%. This can be a serious drawback, especially for a mobile array like NARS. In practice a 2^{nd} order anti-aliasing filter has proved to be sufficient for NARS, and results in an apparent delay well below the sampling interval even for high noise levels.

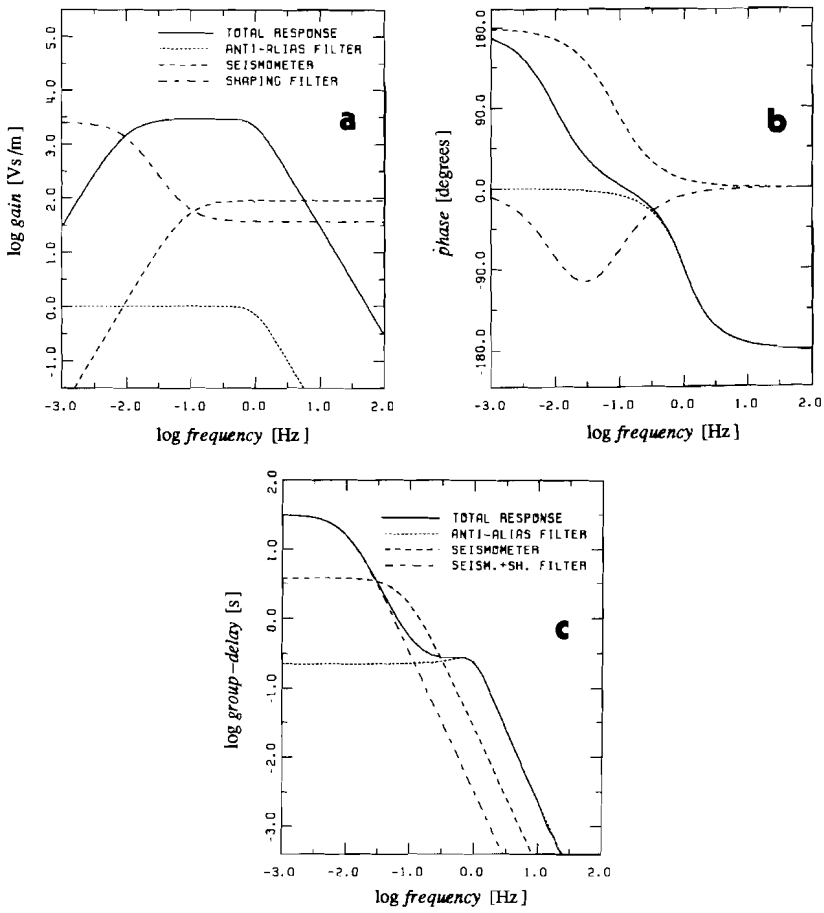

Figure 1.2.3 Individual instrument responses and total system response, showing: a. Amplitude of the transfer functions in *Vs/m* as a function of frequency. b. Phase shift in degrees as a function of frequency. c. Group delay in seconds as a function of frequency. The legenda shown in a. is also valid for b.

1.3 SYSTEM CALIBRATION

Calibration of the NARS stations is effected at every change of tape (roughly every 14 days). A blockpulse of -1.0 Volt, with a duration of 32 seconds, is applied to the calibration coil of the seismometers. Their response to this pulse, together with the pulse itself are recorded on cassette tape. An example of a recorded system calibration is given in figure (1.3.1)

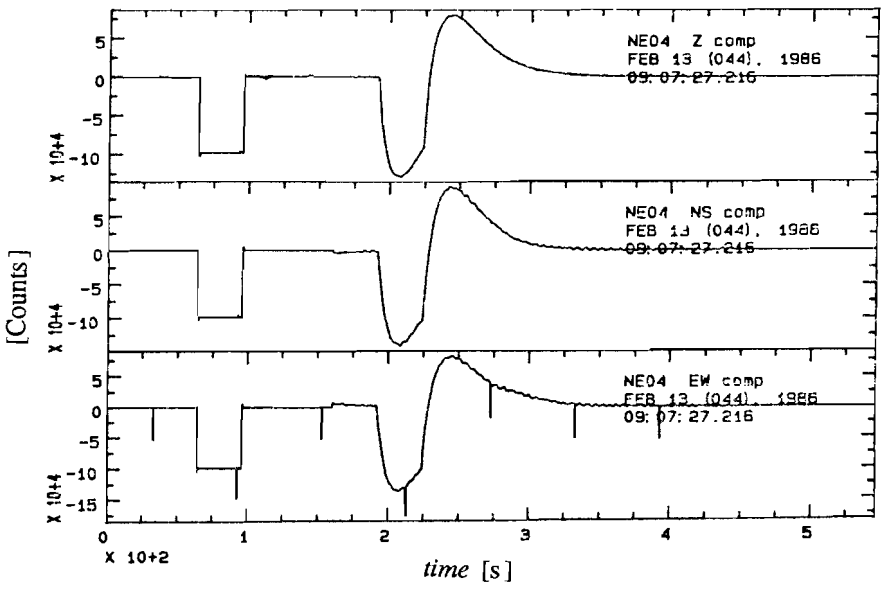

Figure 1.3.1 Recording of a system calibration. Ticks in the EW component are minutemarks to check the timing.

At system calibration the calibration coil applies a step in acceleration (Δa) to the system, followed after 32 seconds by a step ($-\Delta a$). This step in acceleration is given by:

$$\Delta a = \frac{G_{cal}\, I_{cal}}{M} \tag{1.8}$$

I_{cal}, the current through the calibration coil has a value of 4.5 mA. G_{cal} denotes the motor constant of the calibration coil with a value of 0.029±.002N/A and M stands for the weight

of the inertial mass of the seismometer, i.e. 2.0 kg. The system response to Δa is:

$$A(s) = \frac{\Delta a \; T_D(s)}{s^3} \tag{1.9}$$

and is given in Counts/Hz.

There are a number of methods (see Rasson & de Meyer, 1983 for references) to measure the instrument parameters from the calibration pulse, so a check on instrument performance can be made. For the in this thesis presented higher-mode surface wave phase velocity measurements differences in magnification between subsequent stations are not important, since the spectra of each station used in the stacking procedure, see chapter 2, are normalized. However, for body wave modelling studies this is of crucial importance. We will show how one can calculate the magnification parameter A from the measured peak-to-peak amplitude of the calibration curve provided that one knows ω_0,ω_1,h_0 and h_1 from, e.g. , a steady state calibration. Equation (1.9) can be written as:

$$A(s) = \frac{\Delta a A}{(s+\omega_0)^2[(s+\omega_1 h_1)^2+\omega_1^2 h_1^2]} \qquad \omega_0 = .063\text{Hz} \; ; \omega_1 = 6.283\text{Hz} \; ; h_1 = 0.707 \tag{1.10}$$

In the time domain this gives (Jarosh and Curtis, 1973):

$$a(t) = \frac{A\Delta a}{(\xi^2+\eta^2)^2}\,[2\xi+t(\xi^2+\eta^2)]\,e^{-\omega_0 t}+[-2\xi\cos\eta t + \frac{(\xi^2-\eta^2)}{\eta}\sin\eta t]\,e^{-\eta t}$$

$$\xi = (\omega_0-\omega_1 h_1) \quad \eta = \omega_1 h_1 \tag{1.11}$$

Since $\omega_0 \ll \omega_1 h_1$ the term $e^{-\omega_0 t}$ is dominant after the first three samples for the NARS instrumentation, thus we can make the approximation:

$$a(t) = \frac{A\Delta a}{(\xi^2+\eta^2)^2}\,[2\xi+t(\xi^2+\eta^2)]\,e^{-\omega_0 t} \qquad (t>0.375s) \tag{1.12}$$

having a maximum at

$$t_{\max} = \frac{1}{\omega_0} - \frac{2\xi}{(\xi^2+\eta^2)}$$

For the NARS instrumentation the foregoing analysis has to be modified since the total calibration curve consists of two parts: A negative peak from the application of -1 Volt to the system, followed after τ (=32) seconds by a positive peak from switching off the calibration voltage. This sequence can be described by:

$$a'(t) = a(t)H(t) - a(t-\tau)H(t-\tau) \tag{1.13}$$

where H(t) denotes the Heaviside function. Differentiation with respect to t gives extrema

for this function.
For $0 \leq t < \tau$:

$$t_{min1} = \frac{1}{\omega_0} - \frac{2\xi}{\xi^2+\eta^2} \quad \textit{assuming} \quad t_{min1} < \tau \quad (\textit{see fig } 1.3.2.);$$

and for $t \geq \tau$:

$$t_{max2} = t_{min1} + \frac{\tau}{1 - e^{-\omega_0 \tau}} = t_{min1} + b\tau$$

The peak to peak amplitude A_{pp} is given by:

$$A_{pp} = | a'(t_{min1}) - a'(t_{max2}) |$$

$$= | \frac{A \Delta a}{(\xi^2+\eta^2)^2} e^{-\omega_0 t_{min1}} [2\xi\lambda + t_{min1}(\xi^2+\eta^2)\lambda + b\tau(\xi^2+\eta^2)[\lambda-1]$$

$$-\tau(\xi^2+\eta^2)\ e^{-\omega_0 \tau[b-1]}\ ] |$$

$$\lambda = 1 - [1 - e^{\omega_0 \tau}] e^{-\omega_0 b \tau} \tag{1.14}$$

τ is known accurately, $\tau = 32.0$s, and from t_{min1} and t_{max2} we can even check the parameter ω_0. Unfortunately the parameters t_{min1} and t_{max2} are hard to measure accurately since the calibration curve is very flat near its extrema. Microseismic noise disturbes the measurements considerably, especially in the stations in the Netherlands and Denmark. In practice the measured peak-to-peak amplitude of the calibration curve shows variations of up to 25% at the same station. This is due to station conditions, especially temperature and athmospheric pressure fluctuations. Figure 1.3.2 shows a calibration curve recorded in station NE06 (Witteveen) together with the theoretical response calculated from equation (1.11). Apart from a difference in absolute magnification the curves match well. Synthetic seismograms of fundamental mode Rayleigh waves, calculated for NARS instruments, show that the amplitudes are consistent with the recorded data within 20% (Snieder, pers. comm.), as was expected from the calibration results. A steady state calibration of all the stations is planned for early 1987.

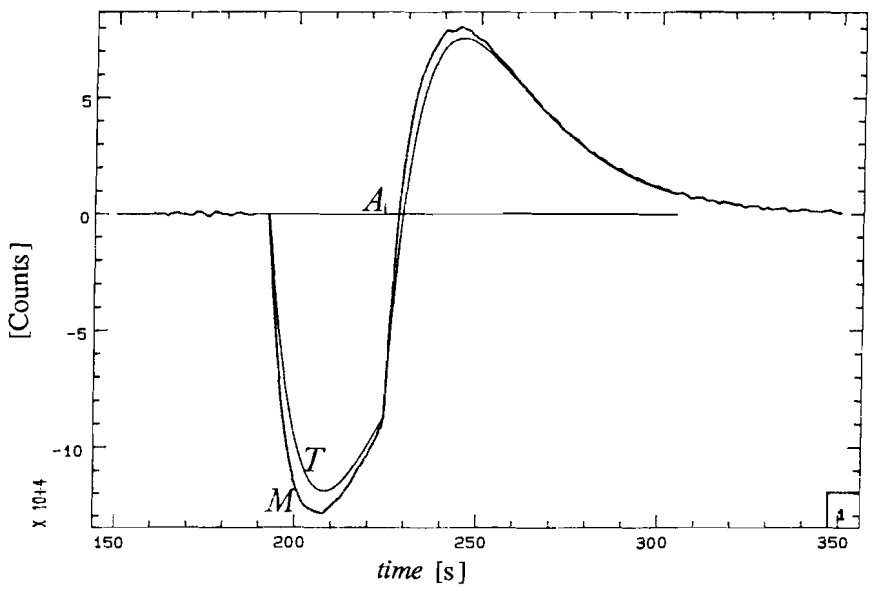

Figure 1.3.2 Comparison between theoretical (T) and measured (M) calibration curve. (A) is the neglected factor [..] $e^{-\eta t}$ in equation (1.11).

1.4 NARS INSTALLATION AND OPERATION

As described in the general introduction, the NARS experiment has as its primary aim the measurement of the dispersion of higher-mode surface waves of the west-European platform. The higher-modes appear as an interference pattern in recorded seismograms and the dispersion of the individual modes can only be directly measured in the wavenumber domain through a stacking procedure (see chapter 2). For an optimum result it is necessary that all NARS stations are functioning at the occurence of an event. Therefore the installation and operation of NARS described in this chapter is focussed on keeping as many stations as possible functioning at the same time.

1.4.1 Organisation

Thanks to the generous cooperation of institutes, station managers and country supervisors listed in table 1.4, we were able to carry out the NARS experiment. The task of a station manager is to change a cassette tape once every 14 days and sent it to the data centre in Utrecht. In case a station malfunctioning is detected the datacentre should be contacted as soon as possible, directly or with the aid of the country supervisor.

Table 1.4 NARS station managers and country supervisors

Station	Station Manager
NE01	G. Lind;
NE02	V. A. Glargaard;
NE03	J. Sorensen;
NE04	L. Beuving; T. Jipping; P.J.M. Wit;
NE05	A. van Wettum;
NE06	J. Rasson;
NE07	A. Simonin;
NE08	J.-H. Pelletier;
NE09	R. and B. Darchen; Mr. Bages
NE10	M. Vadell; J. Esprabens; J. Bouillon;
NE11	G. Cremades; M. Diez;
	M.A. and M.-J. Bordeje Muguerza;
NE12	M. Herraiz; B. Benito;
NE13	D. Hergueta;
NE14	F. Vidal-Sanchez; F. de Miguel; G. Alguacil; J.M. Guirao and G Olivares
NE15	F.L.M.V. Bergsteijn;
NE16	J. Dorel; J. Fourvel;
NE17	G. Payo;
NE18	S. Dujancourt;

Country	Supervisor
Denmark	S. Gregersen; E. Jensen;
France	A. Simonin; N. Jobert
Spain	M. Herraiz; A. Udias

1.4.2. Installation

NARS began its operation in March 1982 with the installation of an experimental station in Utrecht (NE05). Within 4 months also the station in Dourbes (Belgium, NE06),

and Witteveen (NE04) were installed. With these three stations within a radius of 200 km from the datacentre in Utrecht we were able to gain some experience with the instrumentation (and with possible customs problems in west European countries).

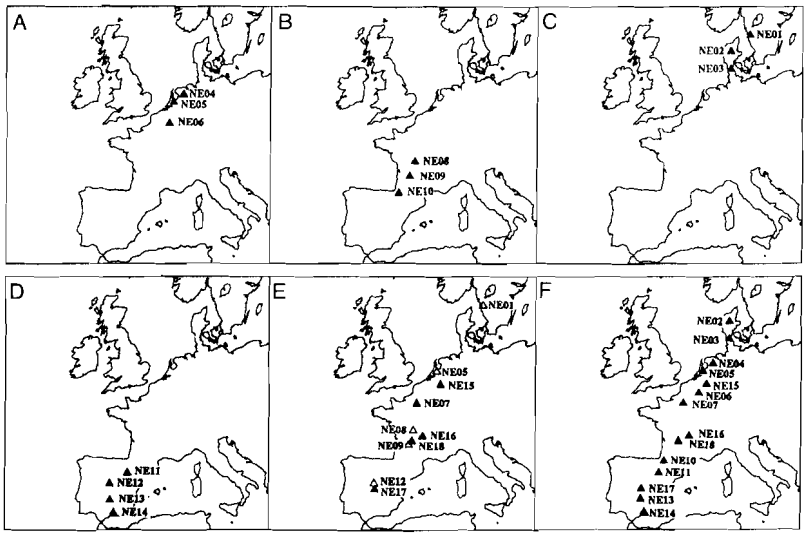

Figure 1.4.1. Installation scheme of the NARS array. [A] June 1982, [B] November 1982, [C] January 1983, [D] May 1983, [E] November 1983 array complete. Open triangles denote stations that were closed during 1983-1986 and moved to stations NE15-NE18, [F] December 1986.

In November 1982 three stations could be placed in France, NE08-NE10, in January 1983 two stations in Denmark and one in Sweden, NE01-NE03, and in May 1983 four stations in Spain, NE11-NE14. Finally the array became complete with the installation of NE07 in November 1983. Figure 1.4.1 shows the different stages of installation and table 1.5 the station locations and their period of operation. In six cases:NE01,NE05,NE08,NE09,NE11 and NE12, station locations proved to be inadequate after some time and alternative locations had to be found.

Table 1.5: NARS station coordinates.				
	Station	Coordinates	Elevation [m]	Period of operation
NE01	Gothenborg	57.801N 12.132E	55.0	Feb. 83- Jan. 86
NE02	Monsted	56.459N 9.170E	60.0	Feb. 83
NE03	Logumkloster	55.045N 9.153E	25.0	Feb. 83
NE04	Witteveen	52.813N 6.668E	17.0	Jul. 82
NE05	Utrecht	52.088N 5.172E	2.0	Mar. 82[1]
NE06	Dourbes	50.097N 4.595E	225.0	Jul. 82
NE07	Villiers-Adam	49.074N 2.232E	70.0	Nov. 83
NE08	Aigurande	46.420N 1.730E	360.0	Nov. 82- Dec. 84
NE09	Les Eyzies	44.852N 0.981E	160.0	Nov. 82- Feb. 86
NE10	Arette	43.086N 0.699W	480.0	Nov. 82
NE11	La Almunia	41.477N 1.372W	370.0	May 83- Nov. 83
NE11	Ainzon	41.814N 1.517W	440.0	Nov. 83
NE12	Valle de los Caidos	40.642N 4.155W	1280.0	May 83- Feb. 85
NE13	Puertollano	38.685N 4.091W	700.0	May 83
NE14	Granada	37.190N 3.595W	774.0	May 83
NE15	Valkenburg	50.867N 5.785E	100.0	Jun. 84
NE16	Clermont Ferrand	45.763N 3.103E	80.0	Nov. 84
NE17	Toledo	39.881N 4.049W	480.0	Feb. 85
NE18	Rejaudoux	45.304N 1.516E	410.0	Feb. 86

[1] Station closed between June 1984 and Januari 1986

1.4.3. Data processing

Until May 1985 NARS data have been processed on a HP-1000 mini computer with limited disk space (120 Mbyte) and one 1600 bpi tape unit. The NARS data format had been chosen to satisfy our needs within these constraints, but was incompatible with other existing data formats.

In May 1985 the HP-1000 was exchanged for a GOULD PN6080, a 32 bit machine equipped with a UNIX Berkely 4.2 operating system, 1020 Mbyte disk space and two 1600/6250 bpi tape units.

The data format in use since then is compatible with the Global Digital Seismograph Network (GDSN) format (Hoffman, 1980). This facilitates the exchange of data and enables us to use all data distributed by the GDSN together with NARS data, without any format conversions. Furthermore, a vast amount of software developed by the GDSN for retrieval of the data could be used. Because NARS is the first large scale broad-band experiment in

global seismology, we will describe the data processing in detail.
After the cassette tapes with the data are received by mail, a rough print-out of the data is made with the aid of the play-back unit (CTU-1). Obvious instrumental problems are immeadiately detected and action can be taken for repair. Cassette tapes are subsequently read on a Micro-Sol microcomputer equipped with an CP/M operating system and C-compiler. Data are stored on a 20 Mbyte Winchester disk and some preliminary calculations are made. These calculations provide insight in the nature of the recorded triggering. Routinely a check is made on:

[1] The calibration, peak-to-peak amplitude is calculated.

[2] Microseismic noise, dominant frequency is calculated

[3] Parasitic signals, dominant frequency is calculated.

[4] Identification of the seismic event.

For each triggering start and end times, instrument status information and parameter settings are written to a report file together with outcome of the preliminary calculations mentioned above. Report files are printed and kept in a binder. Valid data are transmitted from the MicroSol to the Gould system and converted to GDSN format. This means that the 114 byte PDR-2 header is converted to a 20 byte GDSN header. No information is lost, since most of the PDR-2 header contains status information on the PDR-2 system and this information is kept in the report files. Data remain in 16 bit multiplexed format. The mantisse is converted to a two's complement code and the exponent changed from a maximum of 2^7 to 2^{10}. After conversion data are stored on disk in station directories and plots of the first 400 seconds of all accepted events are made and kept in binders. When data from all stations of a certain time period are processed event tapes are constructed. Apart from the data, preceded by a data-log that contains information on system response and calibration, a station-log and event-log are constructed.
The station-log contains not only the location of the station, but also the type of data (intermediate period) and time corrections to be applied to the data. Time corrections are routinely determined by measuring the onsets of the minute pulses on the EW channel.
The event-log gives a list of station names that recorded this event together with the position of the recordings at the tape. Selection criteria for events to be stored on event tapes are:

[1] Events with magnitude ≥ 5.8

[2] Events of magnitude <5.8, but recorded at 3 or more stations.

[3] All European events that are reported by the Preliminary Determination of Epicenters (PDE), compiled by the U.S. Geological Survey.

These criteria are in use from 1985 onward. Event tapes from 1983 to 1985 are assembled without the third criterium and with the treshold magnitude for the first and second criterium

set to 6.0. Apart from using the event tapes in our own laboratory, event tapes are shipped to the USGS, where the data are incorporated in the GDSN data base and distributed.
For NARS data a separate disk of 300 Mbytes is available at the Gould system. In practice approximately 80 Mbyte is used for PDR-2 data handling and 200 Mbytes can be used for data analysis. Selected events can be retrieved from tape and are permanently available to users. For graphical display and simple data manipulation of the data the Seismic Analysis Code (SAC) developed by the Lawrence Livermore Laboratories is in use. Data retrieved from event tape are converted to the SAC format for this purpose.
For handling of file errors (such as polarity reversals or misorientation of horizontal components) a patch file is maintained that contains all information needed to correct the data when being converted to SAC format. This way, the original data (on tape) are always left untouched.

1.4.4. NARS Performance

The performance of the NARS array is measured by selection of events with a body wave magnitude higher than a specified treshold and counting the number of stations that recorded this event. The use of event logs greatly facilitates this search procedure. Figure 1.4.2 shows results of this procedure.
In the installing phase our policy was to carry out station repair as soon as possible. This resulted in a high average return rate with a peak at approximately 400 days (early 1984). The return rate is defined as the number of stations that succesfully recorded one specific event. In this period station repair was too time consuming and we changed to a system where station servicing was limited to two or three times a year. In this way all stations were expected to work optimally at least one to two months after servicing and most continued doing so for a larger time span. This change resulted in a lower return rate, but still a considerable number of events were recorded in 7 or more stations. This is a minimum requirement for higher mode surface wave analysis using NARS.
In the new set up, as explained in the last chapter, European events are incorporated even if they are recorded in only one station. This is the reason why a concentration of mainly low magnitude events recorded in less than 3 stations is visible after 800 days. A catalogue of all recorded events presently available on event tape is presented in appendix C.

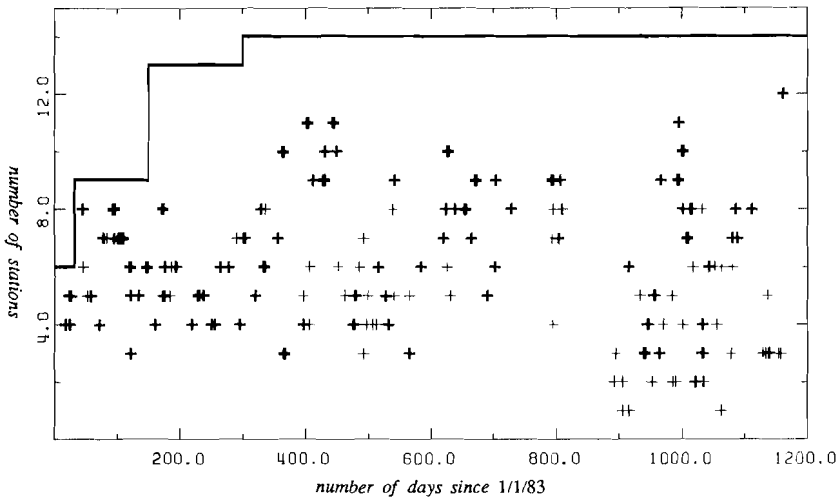

Figure 1.4.2. NARS performance. Symbols with increasing degree of blackness indicate events with body wave magnitude [1] >4.0; [2] >6.0; [3] >6.4. The black line indicates the number of stations that were installed at the time of measurement.

Station repair has been necessary because of many instrument failures. A description of the major problems is given below.

Event recorder,

Software problems:

During the initial stage of the project (3 stations running) two problems were detected:

[1] The original idea that the triggering algorithm should work on all three components simultaneously turned out to produce too many false triggers. It was decided to change the trigger to work on the vertical seismometer only.

[2] STA/LTA ratio triggering is sensitive to a DC offset of the pre-amplifier output. A modification of the algorithm, consisting of subtraction of the true LTA before taking the absolute value of the samples to calculate the absolute LTA, described by Prothero (1980), can solve the problem in a next generation event recorders.

Hardware problems:

During 1982,1983 and 1984 station operation was hindered by many failures in micro-electronic components. Especially EPROMs (Erasable Programmable Read Only Memory) and data RAMs (Random Access Memory) broke down regularly. In the first 500 days of operation at least 8 EPROMs and 10 data RAMs had to be replaced. An additional source of trouble is the use of sockets to mount the EPROMs and data RAMs. Pins incorrectly mounted occasionally make contact and generate errors. Sockets were removed for the data RAMs in 12 PDR-2's. During 1985 and 1986 the EPROM problems diminished, but RAM defects kept troubling us.
Installation of stations in a very humid surrounding, like a cave or old mine, causes corrosion troubles. Some parts of the tape-drive of the event recorder were originally not plated. Replacement with plated parts in subsequently all stations solved this problem.
Information is recorded on cassette tape using four tracks, three signal and one parity track. Early 1986 wires connected to the write-head of the recorder came loose in two stations. When reading these tapes at the data centre the play- back unit showed good quality data for two of the three channels, the third one showing no data at all. Data transfer to the micro computer however was not possible, the recorder could not find any data. This problem could be solved by sharing the fourth track with the absent channel, so the recorder could synchronize at the start of a cassette tape. Since the header is (partly) unreadable in this procedure, the recording date and time is not present. If the absent channel is the EW component, time can only be roughly reconstructed by lining up of onsets from different stations.

Seismometers,

The sudden appearance of parasites in the seismic signal, in several cases after two years of operation, did upset our triggering and resulted in filling one cassette in one day. These parasites only occur on the vertical channel. An example of such a feature can be seen in figure 1.4.3. The fact that only the vertical instrument was affected limited the problem to the spring or flexures. This problem is under study at the manufacturer.
Humidity caused oxidation problems mainly for the horizontal seismometers. These instruments are not sealed with a rubber ring as the vertical component. The casing of the instruments was modified as that of the vertical seismometer and the horizontal instruments were

replaced. An additional effect of humidity on seismometers is the generation of an offset. The connection between the seismometer suspension and the casing consists of very thin copper wires mounted on a terminal strip. Condensation of water particles on this strip results in leakage between the three components. Humidity problems could also be diminished by surrounding the seismometers and pre-amplifier with a blanket made of very thin aluminum foil. The small amount of heat produced by the power supply of the pre-amplifier prevents condensation of water particles on the seismometers.

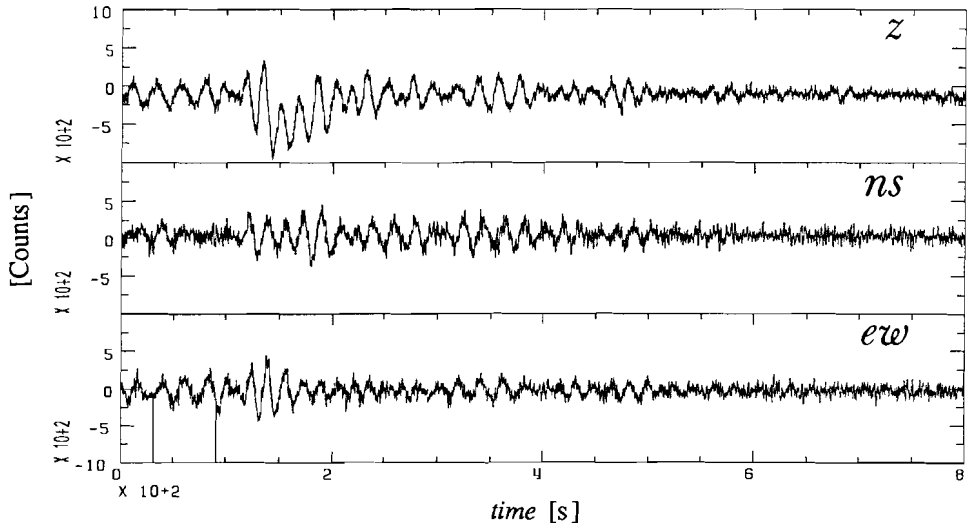

Figure 1.4.3. An example of a long period parasitic signal, only visible on the vertical component.

The sensitivity of the vertical seismometer to temperature changes is a major hindrance in station operation. A change of only 3° C is sufficient to move the mass so far out of its equilibrium that proper functioning is impossible. The change in outside temperature from summer to winter and vice versa can easily be 30° C along the array. Since the array should be portable and therefore not restricted to well isolated environments we had to find a solution that can be installed and removed in one day.

For this purpose a temperature isolation box has been developed that consists of two polystyrene covers with a small heating cell inside the top of the outer cover in order to minimize turbulent air currents (see Willmore, 1979). Direct radiation from the heating cell sometimes disturbed the seismic signal. This problem has been overcome by using tiles glued to

the outside of the inner box. A detailed description of the box is given by van der Meer (in prep.).

1.5 CONCLUSION

From our experience in deploying a mobile, digital, broad-band seismograph network like NARS we conclude that it is feasible to carry out a seismic experiment with only a very limited staff. The help of station managers and country supervisors in maintaining the stations and establishing a good communication between the datacentre and the seismic stations is of vital importance.

One drawback of the very rapid development of (digital) instrumentation is the fact that the products seem to be not very well tested. The continuous problems we encountered in failing components like EPROMs and data RAMs and some construction errors support this conclusion. As a consequence we think it very important to be able to monitor the status of a remote station directly from the data centre. This will be a future development for the NARS instrumentation.

For this study the consequences of the instrument failures are that the original idea of a sufficient station coverage is not fulfilled. Therefore it is advisable to look for algorithms that can enhance resolution in the process of stacking of higher mode surface waves using sparse datasets. This will be explored in the next chapter.

PART 2: ANALYSIS OF HIGHER MODES OF SURFACE WAVES

As was discussed in the general introduction, the measurement of higher-mode surface wave dispersion became possible with the introduction of a stacking technique (Nolet, 1975). A prerequisite for the application of this technique is the existence of a linear array of seismographs like NARS. In an analysis of the possibilities and limitations of this technique, Nolet and Panza (1976) came to the conclusion that for regions of mild lateral heterogeneity the main source of error in the measurement of phase velocities was due to the inadequacy of the array response. Since the array response is fully determined by the position of the stations, NARS has been designed as to minimize the influence of an inadequate array response. In the design a return rate of 80% was expected for NARS. However, in practice the average return rate of the data did not exceed 60-70% (see chapter 1.5.4). Therefore we decided to investigate methods to enhance resolution.

2.1 RESOLUTION ENHANCEMENT USING A PRIORI KNOWLEDGE

Higher mode surface waves show up in the seismogram as a pattern of interfering waves arriving in the time interval between the S onset and the fundamental mode surface wave. In order to separate the different modes we have to transform the frequency spectrum $w(\Delta,\omega)$ of the signal $s(\Delta,t)$ to the complex wavenumber spectrum $W(k,\omega)$:

$$W(k,\omega) = \int_{-\infty}^{\infty} w(\Delta,\omega)\, e^{-ik\Delta}\, d\Delta \tag{2.1}$$

where k denotes the wavenumber, ω angular frequency and Δ epicentral distance. By showing the equivalence between surface waves and normal modes in the limit for large radial orders, Nolet (1976) derived an expression for the frequency spectrum:

$$w(\Delta_j,\omega) = \sum_{n=1}^{M} F_{nj}(\omega)\, e^{ik_n(\omega)\Delta_j + i\phi_{nj}(\omega)} \tag{2.2}$$

$F_{nj}(\omega)$ is the amplitude of mode n in station j and $k_n(\omega)$ the wavenumber of mode n. ϕ_{nj} is the initial phase and depends on the azimuth from the source. The most important approximation made in the derivation of equation (2.2) is the asymptotic representation of a Legendre polynominal for $\Delta \gg 0$. This approximation imposes limits to the location of the array with respect to the source. Panza et al (1973) determined as condition for a 3 figure accuracy in amplitude and phases: $k\Delta > 10$, which is appropriate for the measurements presented in this thesis. If stations do not differ considerably in azimuth and if the array is not situated near a minimum of the radiation pattern we can neglect the variations of $\phi_{nj}(\omega)$ in the different stations (Nolet and Panza, 1976). Amplitude F_{nj} is a function of station position, but the effect of dissipation over the array is small. We will therefore neglect the station

dependence in the amplitude. If necessary, we can correct for the geometrical spreading. Combination of equation (2.1) and equation (2.2) without station dependence of amplitude and initial phase gives:

$$W(k,\omega) = 2\pi \sum_{n=1}^{M} F_n(\omega)\, e^{i\phi_n(\omega)}\, \delta(k_n - k) \tag{2.3}$$

The complex wavenumber spectrum consists of a set of M delta functions $\delta(k_n - k)$, centered around the modes n. Unfortunately, we have a finite amount of recording stations and therefore we can only make an estimate $\overline{W}(k)$ of $W(k)$:

$$\overline{W}(k,\omega) = \frac{1}{N} \sum_{j=1}^{N} a(\Delta_j,\omega)\, w(\Delta_j,\omega)\, e^{-ik\Delta_j} \tag{2.4}$$

The contribution of each station j is weighted by a factor $a(\Delta_j,\omega)$. Combination of equation (2.4) and (2.2) gives at constant frequency:

$$\overline{W}(k) = \sum_{n=1}^{M} F_n\, e^{i\phi_n}\, H(k_n - k)$$

$$H(k) = \frac{1}{N} \sum_{j=1}^{N} a(\Delta_j)\, e^{ik\Delta_j} \tag{2.5}$$

$|H(k)|^2$ is called the array response function and its shape determines the resolution in the measurements. Because the number of stations is very limited, $H(k)$ does not resemble a delta function as in (2.3)- which we try to approximate. Although $|H(k)|$ is peaked in $k=0$, there are many secondary maxima. This is essentially an effect of spatial aliasing and we shall refer to these peaks as 'aliasing lobes'. See figure 2.1.1 for a typical example of an array response function shape. Since we know the location of the stations, and thus the shape of the array response function, we can correct the wavenumber spectrum for the effect of spatial aliasing and possible non-equidistant sampling. The CLEAN algorithm, introduced in seismology by Nolet and Panza (1976), iteratively carries out this procedure. Cara (1978) shows the usefulness of choosing weights $[a(\Delta_j)]$ in order to manipulate the array response function. To achieve this he designed a penalty function that was subsequently minimized. Accurate determination of the phase velocity of mode n can be obtained if the number of modes present in the signal is small. Therefore small segments of the seismic signal are selected in the time domain around a traveltime $\tau = \Delta_j / v_g$ and estimator (2.4) calculated at a chosen frequency (ω_0). This procedure is repeated for a suite of group velocities and results in a mode separation diagram of phase- versus group- velocity for ω_0 (see figure 2.3.8).

Our present aim is to investigate whether the above described stacking technique can be improved by using optimum filtering techniques to determine the weights $a(\Delta_j)$ or by

modifying the estimator equation (2.4).

2.1.1. Optimum weights

A comparison with classical deconvolution provides insight in the role of the weights $a(\Delta_j)$ in equation (2.5). For this purpose we will introduce a stationary time series $a(t)$ that can be written as a convolution of a wavelet $B(t)$ with a series of spikes C_n:

$$a(t) = \sum_{n=1}^{M} C_n B(t-t_n)$$

$$\overline{W}(k) = \sum_{n=1}^{M} F_n' G(k-k_n), \quad G(k) = H^*(k), \quad F_n' = F_n e^{i\phi_n} \tag{2.6}$$

From equation (2.6) one can observe a strong analogy of the estimator $\overline{W}(k)$ with $a(t)$. As a consequence our problem of recovering the modes from our estimator is equivalent with wavelet deconvolution. The complex conjugate of the array response function $[G(k)]$ is analogous to the wavelet. This allows us to apply a vast amount of well known filtering techniques (e.g. Robinson and Treitel, 1980; Oldenburg, 1981). One important difference we should keep in mind in this comparison is that the station location of NARS is not equidistant. In Appendix B we will show the importance of choosing non-equidistant patterns and how an optimum array configuration can be determined.
The role of $G(k)$ can be clarified with a well known excercise from Fourier theory. If we define the discrete Fourier transform of the finite series $x(\Delta_j), j=1,....,N$ as:

$$\bar{X}(k) = \frac{1}{N} \sum_{j=1}^{N} x(\Delta_j) e^{-ik\Delta_j} \tag{2.7}$$

$$x(\Delta_j) = \int_{-\infty}^{\infty} X(k) e^{ik\Delta_j} \frac{dk}{2\pi} \tag{2.8}$$

it can be shown by substitution of (2.8) in (2.7), that the true $X(k)$ can not be uniquely reconstructed from the estimated $\bar{X}(k)$, due to the (un)weighted array response function or its complex conjugate $G(k)$:

$$\bar{X}(k) = \int_{-\infty}^{\infty} X(k') G(k-k') \frac{dk'}{2\pi} \tag{2.9}$$

We assume that $X(k)$ is bandlimited ($-\kappa \leq k \leq \kappa$). This assumption is not unreasonable in seismological practice and serves to avoid or reduce problems of spatial aliasing. The shape of the array response function (or its complex conjugate) is essential in our reconstruction and we can try to manipulate it by minimizing a form like:

$$\int_{-\kappa}^{\kappa} |G(k)-L(k)|^2 \, dk \tag{2.10}$$

where $L(k)$ is the target function we want $G(k)$ to resemble. Usually, this function is chosen as a delta function or a Gaussian function with prescribed width.

Before we treat this problem in detail it is important to understand the relation between the choice of weights in the Δ domain and a filter operation in the wavenumber domain. It will be shown explicitely that these two operations are equivalent. In the rest of this chapter we will write functions in the wavenumber domain with a capital, their representation in the Δ-domain in lower case.

If we denote the unweighted 'wavelet' with $G'(k)$:

$$G'(k) = \frac{1}{N} \sum_{j=1}^{N} e^{-ik\Delta_j} \tag{2.11}$$

we can show that the application of weights $a(\Delta_j)$ is a filtering operation in the k-domain and can be written as a convolution with a filter response $V(k)$:

$$G(k) = G'(k) * V(k) \tag{2.12}$$

$$= \int_{-\infty}^{\infty} G'(\kappa)\, V(k-\kappa)\, d\kappa$$

Substitution of (2.11) and using (2.7) leads to:

$$G(k) = \frac{1}{N} \sum_{m=1}^{N} v(\Delta_m)\, e^{-ik\Delta_m}\, 2\pi\, \delta(\Delta_m-\Delta_j)$$

$$= \frac{2\pi}{N} \sum_{j=1}^{N} v(\Delta_j)\, e^{-ik\Delta_j} \tag{2.13}$$

And we see that the factor $2\pi v(\Delta_j)$ can be identified with the weights $a(\Delta_j)$ in equation (2.5). We will now follow the theory of Byrne and Fitzgerald (1982,1984) to show the influence of the band-limitness of a signal in an elegant way. A function $P(k)$ is introduced, which contains a priori known information of the spectral density of the signal. Furthermore we consider the Hilbert space $H = L^2(-\infty,\infty;1/P(k))$ with inner product

$$< Y(k), Z(k) >_p = \int_{-\infty}^{\infty} Y(k)\, Z^*(k)\, \frac{1}{P(k)}\, \frac{dk}{2\pi} \tag{2.14}$$

Suppose $G(k)$ is band-limited on $[-\kappa;\kappa]$, then we can minimize the weighted norm:

$$\int_{-\infty}^{\infty} |P(k)\,G(k) - L(k)|^2 \frac{1}{P(k)}\,dk \qquad P(k) = 1 + \varepsilon \text{ for } -\kappa \leq k \leq \kappa$$

$$= \varepsilon \text{ for } k \textit{ elsewhere} \tag{2.15}$$

ε is introduced to incorporate an average level outside the limited bandwidth. This parameter plays the role of a damping parameter. After minimization of equation (2.15) with respect to $a^*(\Delta_m)$ we obtain:

$$\sum_{m=1}^{N} a(\Delta_m)\, p(\Delta_n - \Delta_m) = N\, l(\Delta_n) \tag{2.16}$$

with $p(\Delta_j)$ and $l(\Delta_j)$ the inverse Fourier transform of $P(k)$ and $L(k)$ respectively. For our choice of $P(k)$ we can write:

$$p(\Delta_n - \Delta_m) = \frac{\sin\kappa(\Delta_n - \Delta_m)}{\pi(\Delta_n - \Delta_m)} + \varepsilon\,\delta(\Delta_n - \Delta_m) \tag{2.17}$$

In case of equidistant sampling, $\Delta_j = j\,\Delta$, and a band-limitness that coincides with the Nyquist interval, $\kappa = 2\pi / \Delta$, equation (2.16) simplifies to:

$$a(\Delta_n) = \frac{\Delta}{2} N\, l(\Delta_n) \tag{2.18}$$

The highest resolution is obtained when we take for $L(k)$ a delta function, so $l(\Delta_n) = 1$ and weights are constant. This means that for equidistant location we can not expect an increase in resolution by using weights. In any other case we have to solve equation (2.16) to calculate weights $a(\Delta_j)$. For $L(k) = \delta(k)$ we will further investigate the influence of the weights $a(\Delta_j)$ on the shape of the array response. Of main interest are two parameters:

[1] The width of the main lobe of the array response (determines the resolution).

[2] The height of the aliasing lobes. Aliasing lobes dominate the 'noise level' in the k-domain

As can be seen from equation (2.17), the parameters that determine the weights are the band-width κ and damping parameter ε. In figure 2.1.1 we show results for the 14 station NARS configuration. In this figure the width of the mainlobe and height of the first side lobe is measured as a function of κ for 3 values of ε. Two regions can be observed:

[a] $\kappa > 1.2\ 10^{-2}$:

In this range the damping parameter has no influence on the shape of the array response function. A trade-off exists between the width of the main lobe and the height of the first side lobe.

[b] $\kappa < 1.2\ 10^{-2}$:

The width of the mainlobe decreases with decreasing κ. Increase of the damping factor slows down this phenomenon. The height of the first sidelobe oscillates for $\varepsilon = 0$ as a function of κ and behaves much smoother when damping is increased. When κ becomes smaller than the width of the main lobe (approximately given by k_2), the algorithm becomes unstable.

The region $k_2 \leq \kappa \leq 1.2\ 10^{-2}$ is favourable for increasing the resolution without blowing up the first side lobe. The question rises what happens to the other side lobes. To investigate this we choose a damping factor of 1% and calculate the height of the first 5 side lobes as a function of κ. Results are shown in figure 2.1.2.

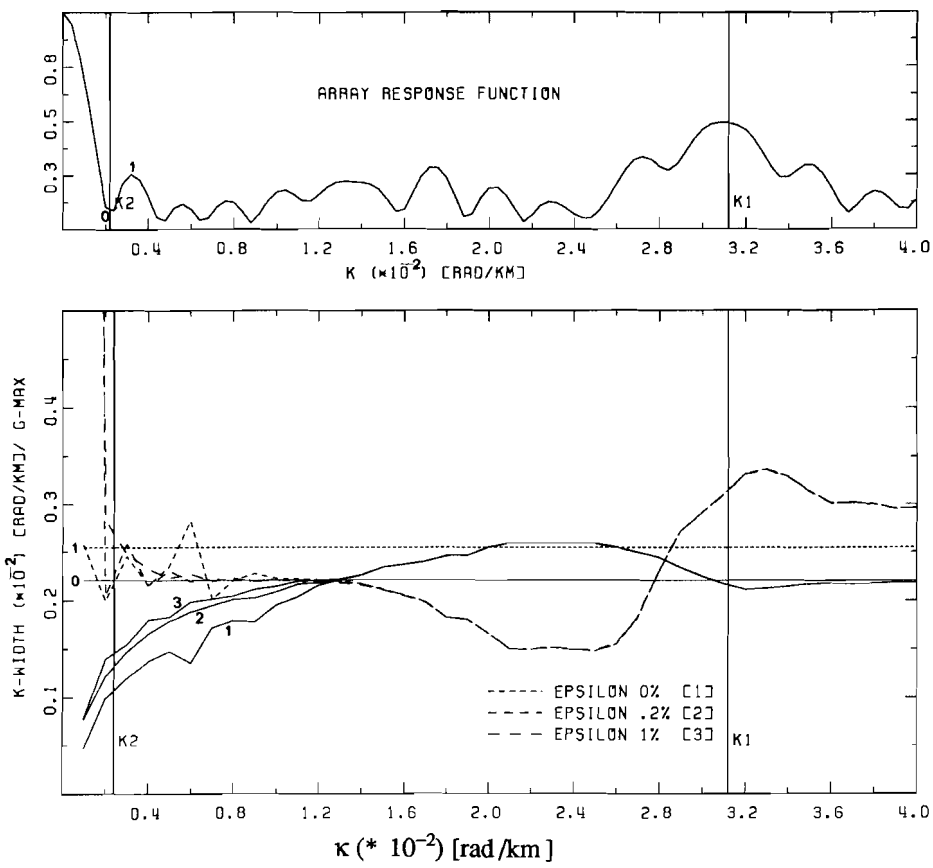

Figure 2.1.1. The top figure gives the unweighted array response function $|G'(k)|^2$. Indicated are the Nyquist wavenumber $k_1 = 2\pi/\Delta$ and the width of the mainlobe $k_2 = 2\pi/N\Delta$, where Δ is the average station distance. Marked with a 0 is the height of the first minimum aside the main lobe, and 1 the height of the first side lobe. In the lower figure the solid lines give the position of the first minimum (k-width) as a function of band width κ for: [1] $\varepsilon = 0\%$; [2] $\varepsilon = .2\%$ and [3] $\varepsilon = 1\%$. The percentages are relative to $p(0)$. Dashed lines give the height of the first side lobe (G-max) as a function of κ, at the same values of ε as the solid lines. Horizontal lines indicate the values for the unweighted situation and act as reference lines. Labels **0** and **1** in the upper figure correspond with the labels at the horizontal lines in the lower figure

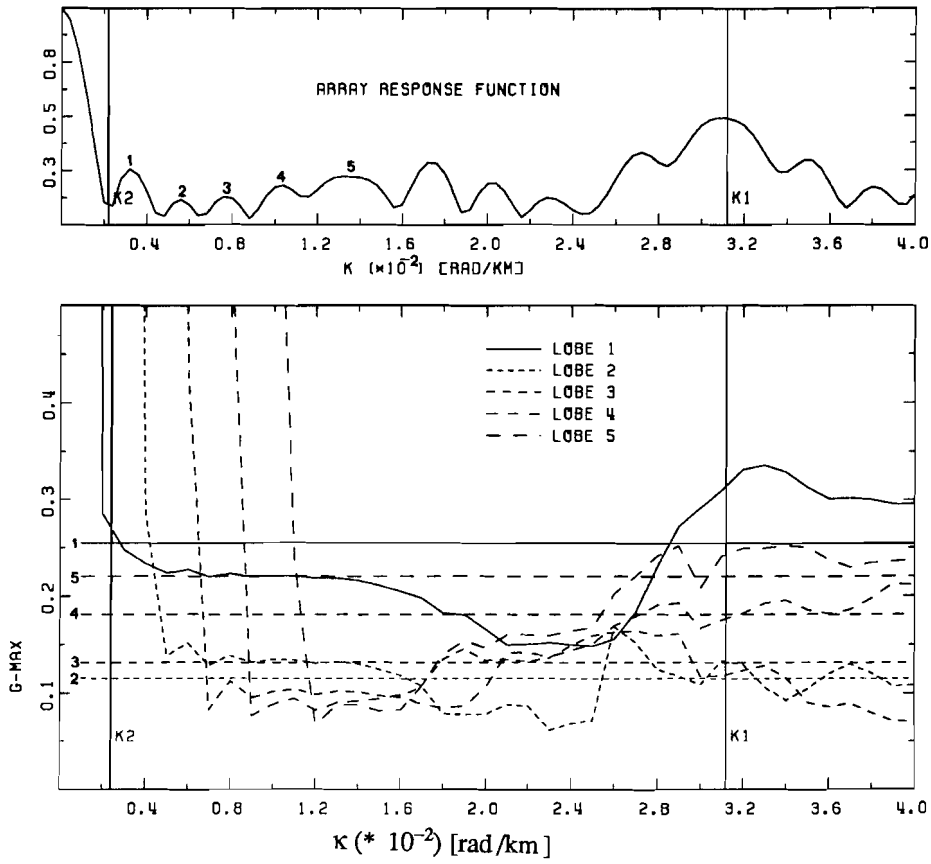

Figure 2.1.2. The description of this figure is the same as figure 2.1.1., except that the width of the mainlobe is omitted and that the dashed lines now give the height of the first 5 lobes. The damping parameter $\varepsilon = 1\%$.

The region $1.2\ 10^{-2} \leq \kappa \leq 2.4\ 10^{-2}$ is favourable to diminish the width of the first five lobes. Combination of the outcome of these numerical experiments leads to the following conclusions:

[1] The width of the mainlobe can be significantly diminished for small values of κ. However, the height of the subsequent sidelobes increases rapidly with decreasing κ.

[2] A region for κ can be given where the first five sidelobes are significantly diminished in height with respect to the unweighted array response, in the case of figure 2.1.2. this can be realized by taking $1.2\ 10^{-2} < \kappa < 2.4\ 10^{-2}$.

Constructions of figures like 1.2.1 and 1.2.2 for a specific station distribution can be helpful to design an array response function. The station distribution will be the limiting factor in the usefulness of applying weights.

2.1.2. Fourier estimators incorporating a priori knowledge

As we have seen in the previous chapter, the incorporation of a priori knowledge provides us with a powerful tool to enhance resolution. In this chapter we will show how we can use a priori knowledge about the spectrum in the Fourier estimator itself. This theory has recently been developed by Byrne and Fitzgerald (1982,1984) and Michette et al (1984). Since we know the approximate location of our modes from previous studies, these techniques are expected to improve the accuracy of the measurements. Suppose we put our a priori knowledge about the shape of the wavenumber spectrum $W(k)$ in a function $P(k)$:

$$P(k) = A_n + \varepsilon \qquad k_n - \kappa_n \le k \le k_n + \kappa_n \ , \ n=0,1,2,...$$

$$= \varepsilon \qquad \textit{elsewhere} \tag{2.19}$$

with k_n the a priori known location of mode n, κ_n the uncertainty in the a priori knowledge, A_n the amplitude of mode n and ε a damping parameter (see last chapter and figure 2.1.3). If we assume $W(k)$ to be a member of the weighted Hilbertspace $H = L^2(-\infty,\infty;\frac{1}{P(k)})$ with inner product (2.14) we can write:

$$w(\Delta_j) = \int_{-\infty}^{\infty} W(k) e^{\,ik\Delta_j} \frac{dk}{2\pi} = \langle W(k), g_j(k) \rangle_p$$

$$g_j(k) = e^{\,-ik\Delta_j} P(k) \tag{2.20}$$

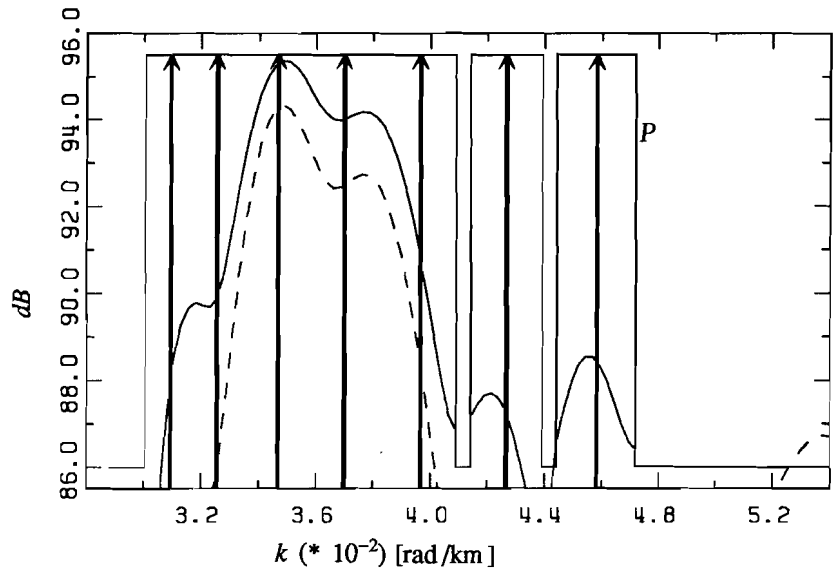

Figure 2.1.3. The absolute value of the complex wavenumber spectrum for one row of a mode separation diagram. The vertical scale is in dB. The maximum of the entire diagram has been set to 100. The dashed curve denotes the conventional DFT stack, the solid curve the PDFT stack. Superposed is the function $P(k)$ in arbitrary units. No information about relative excitation of the different modes is incorporated, i.e. boxes have equal height. Arrows mark the exact locations of the modes.

An estimator $\overline{W}(k)$ can now be constructed, as in Backus Gilbert theory, using the data kernels g_j as a set of basisfunctions:

$$\overline{W}(k) = \sum_{j=1}^{N} b_j g_j(k) \tag{2.21}$$

In contrast to the estimator (2.4), based on a Discrete Fourier Transform (DFT), our parameters b_j are not equivalent to the (un)weighted spectral values $w(\Delta_j)$. If we want to construct our estimator from the data $w(\Delta_j)$ we have to minimize the weighted norm:

$$\int_{-\infty}^{\infty} |W(k) - \sum_{j=1}^{N} b_j P(k) e^{-ik\Delta_j}|^2 \frac{1}{P(k)}\, dk \tag{2.22}$$

Differentiation with respect to b_n leads us to

$$\int_{-\infty}^{\infty} W(k) e^{ik\Delta_n} \frac{dk}{2\pi} = \sum_{j=1}^{N} b_j \int_{-\infty}^{\infty} P(k) e^{ik(\Delta_n - \Delta_j)} \frac{dk}{2\pi}$$

or

$$w(\Delta_n) = \sum_{j=1}^{N} b_j p(\Delta_n - \Delta_j) \tag{2.23}$$

Coefficients b_j can be determined. Our choice for $P(k)$ leads to equation (2.24) for the function $p(\Delta_n - \Delta_j)$ in (2.23)

$$p(\Delta_n - \Delta_j) = \sum_{m=1}^{M} A_m e^{ik_m(\Delta_j - \Delta_n)} \frac{\sin \kappa(\Delta_j - \Delta_n)}{\pi(\Delta_j - \Delta_n)} + \varepsilon\delta(\Delta_j - \Delta_n) \tag{2.24}$$

and the estimator becomes:

$$\overline{W}(k) = P(k) \sum_{j=1}^{N} b_j\, e^{-ik\Delta_j} \tag{2.25}$$

This estimator is called the PDFT estimator (Byrne and Fitzgerald, 1984) and is a generalization of the band-limited extrapolation procedures (Papoulis, 1975).
The stacking operation now consists of two steps: first one has to calculate the coefficients b_j from equations (2.23) and (2.24), then these coefficients are summed with their appropriate kernels $g_j(k)$ in equation (2.25). Figure 2.1.3 shows an example of the enhancement of energy in one row of a mode separation diagram when we use equation (2.25) in stead of equation (2.4).

2.1.3. Comparison of algorithm performance

A comparison of the different algorithms developed in the previous chapters with the conventional stacking technique can be made by measuring their performance on a set of higher mode Rayleigh wave synthetics. Since we know the exact values of the phase velocities for the different modes as a function of frequency, we can construct mode separation diagrams, measure phase velocities for the modes involved, and determine the error in the measurements. For these calculations we calculated synthetic seismograms using parameters identical to the March 24, 1984 Kurile event (see table 3.1) that was actually recorded in 10 NARS stations. The M7 model (Nolet, 1977) and centroid moment tensor solution published in the PDE monthly bulletins were used in the computation.

$$M = \begin{bmatrix} 2.52 & 1.56 & -1.43 \\ 1.56 & 4.82 & 1.96 \\ -1.43 & 1.96 & 3.39 \end{bmatrix} 10^{19}\,[Nm]$$

The synthetics consist of fundamental and first seven higher modes, calculated in the frequency band between 10 and 100 mHz and are shown in figure 2.3.1. Before we can produce mode separation diagrams for this comparison we have to investigate the possibility of using weights and the influence of a priori knowledge on the PDFT estimator.

Weights:

The usefulness of weighting can readily be explored by construction of weight diagrams like 2.1.1 and 2.1.2 for the station configuration of the test signal. Figure 2.3.2 shows that the first aliasing lobe can be significantly reduced in size for $k_2 \leq \kappa_m \leq 2.4\ 10^{-2}$, while the mainlobe width can only be reduced for κ_m close to k_2. The other sidelobes, however (see figure 2.3.3) blow up very quickly and there is no region for κ where we can significantly improve the average height of the first five lobes together. These results are based on a configuration for only one event, but we selected the event/station configuration with the best coverage and the lowest average sidelobe level among all other configurations studied in this thesis. Construction of weight diagrams for the other events in table 3.1 shows that the discussed results represent the best case of all presently available events recorded by the NARS array. In our frequency range of interest, roughly between 20 and 70 mHz, the difference in wavenumber and group velocity between succesive modes is such that the effect of blowing up sidelobes can easily influence the measurements. In general, group velocity curves of the various modes approach each other as the frequency increases up to approximately 0.1 Hz. Cara's (1978) measurements should also suffer from this effect at higher frequencies. The mode separation diagram he shows as an example for his choice of weights is calculated at a frequency of 14 mHz (70 s). The second higher mode that

becomes visible after weighting is clearly separated in group velocity from the much better excited first higher mode. For his example weighting is an excellent tool, but application of the method to higher frequencies is rather doubtful. We can conclude that assigning weights to the station does not provide a useful tool in our case where we want to calculate many mode separation diagrams on a routine basis. However, for special purposes, e.g. to look in the vicinity of a specific mode, weights can be optimally chosen.

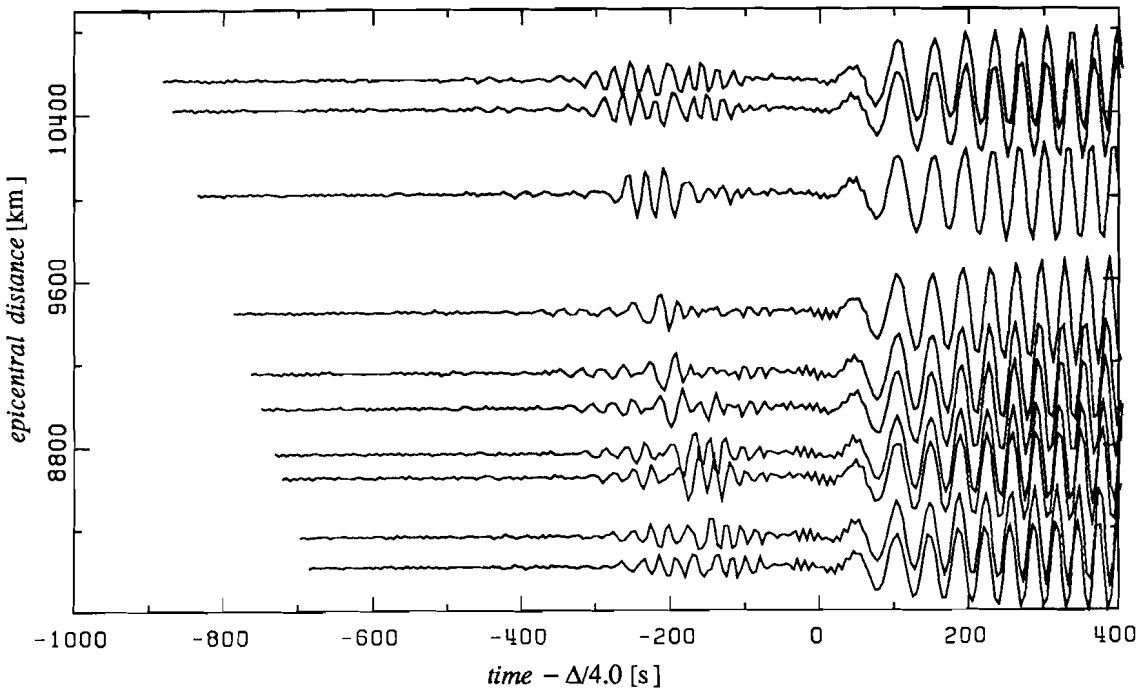

Figure 2.3.1. Synthetic Rayleigh wave data set. Parameters from March, 24 1984 Kuriles event (PDE).

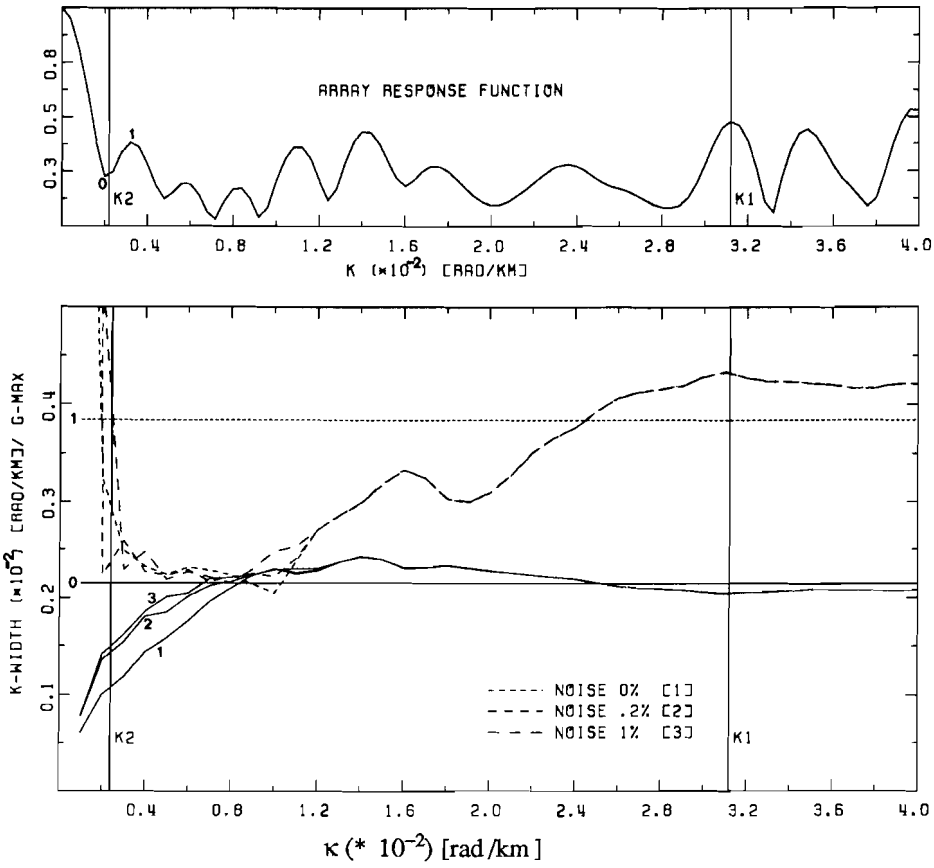

Figure 2.3.2. The description of this figure is the same as in figure 2.1.1.

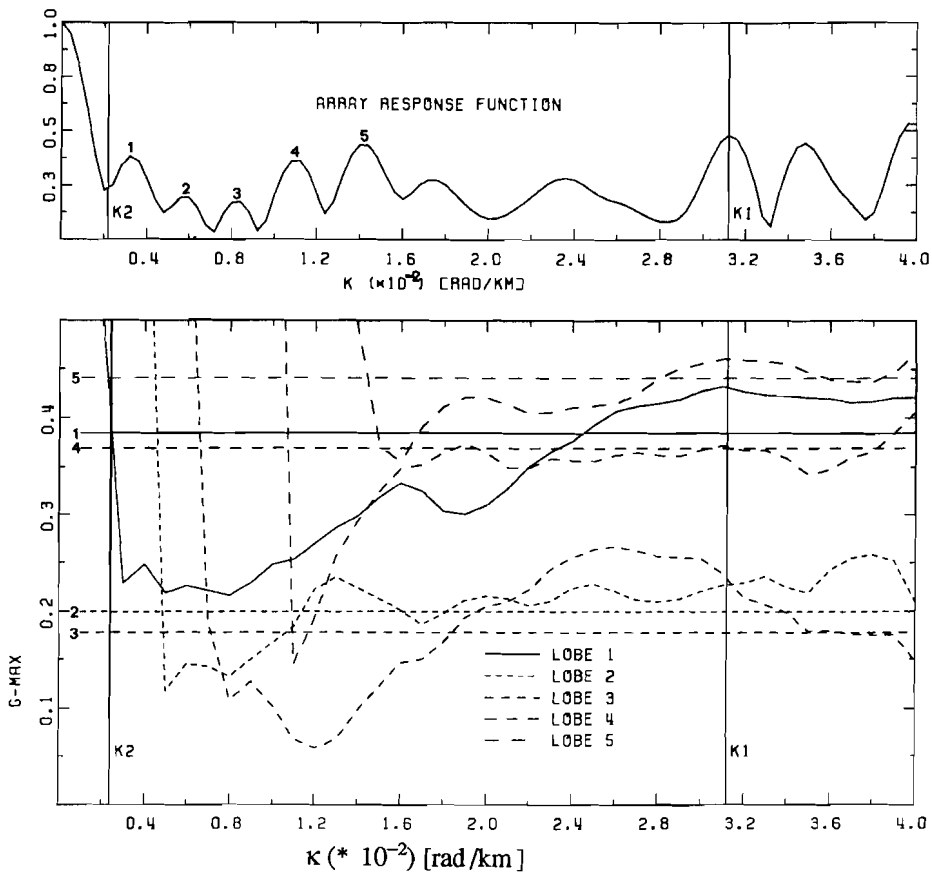

Figure 2.3.3. The description of this figure is the same as in figure 2.1.2.

Influence of a priori knowledge on the PDFT estimator:

When using a priori information in reconstruction of a spectrum by means of the PDFT estimator we have to be sure that this does not introduce a bias in the reconstruction itself. In order to check this, a test has been designed. The set up of the test is illustrated by figure 2.3.4.

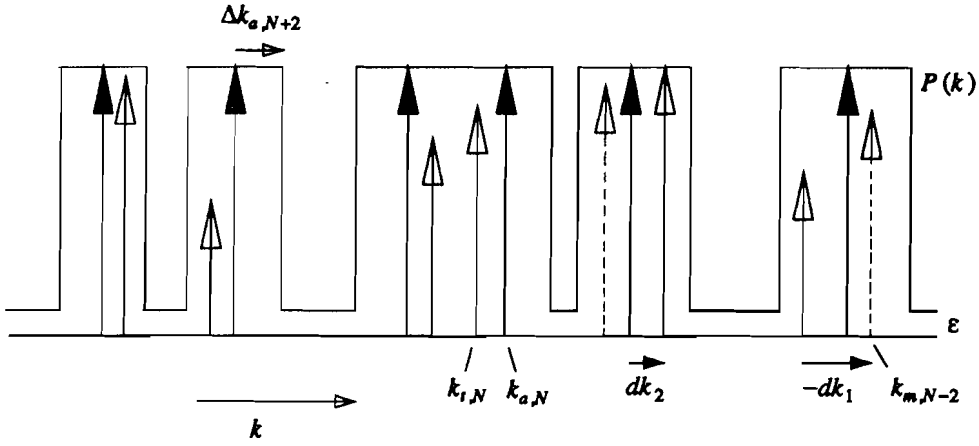

Figure 2.3.4. Test set up. Open arrows with solid shafts are true modes, at locations $k_{t,n}$, solid arrows with solid shafts are a priori assumed modes, at $k_{a,n}$, and open arrows with dashed shafts are measured modes at $k_{m,n}$. For sake of clarity only two measured modes are shown. Parameters of interest are dk_2, the difference between true and a priori location and dk_1 the difference between true and measured location. Uncertainty in the a priori knowledge (box width) is given by $\Delta k_{a,n}$. Modes are counted from right to left as phase velocity increases that way.

The a priori location $k_{a,n}$ of the modes is in this experiment assumed to be located at a distance $(-1)^n \Delta k_{t,n}$ from the true location of the modes. This gives a direct relationship between $k_{a,n}$ and $k_{t,n}$:

$$k_{a,n} = k_{t,n} + (-1)^n \Delta k_{t,n} \tag{2.26}$$

$P(k)$ is constructed as a superposition of boxcar functions around the assumed locations, while no amplitude information has been involved, i.e. all boxes have equal height or A_m= constant in equation (2.19). Parameters that determine the shape of $P(K)$ are the uncertainty in the a priori knowledge, $\Delta k_{a,n}$, and the average level ε. ε is specified relative to the height of the boxes. With these parameters we can compute mode separation diagrams and plot the difference between true and assumed mode location:

$$dk_2 = k_{t,n} - k_{a,n} = (-1)^{n+1} \Delta k_{t,n} \tag{2.27}$$

for each mode n versus the difference between true and measured mode location:

$$dk_1 = k_{t,n} - k_{m,n} \tag{2.28}$$

If $dk_1 = dk_2$, then the measurement is entirely determined by the a priori assumption ($k_{a,n} = k_{m,n}$). On the other hand $dk_1 = 0$ means that the a priori knowledge did not influence the result at all. In our application we want $|dk_1|$ to be close to zero, the measurement should be close to the true value, and $|dk_2|$ as large as possible to accomodate errors in the a priori knowledge. The design of our test is in the wavenumber domain, but the information we are interested in is how well phase velocities can be measured. Phase velocity v_f is related to wavenumber by $v_f = \frac{\omega}{k}$. Since ω is constant we can write for a perturbation in v_f:

$$\frac{\delta v_f}{v_f} = -\frac{\delta k}{k} \tag{2.29}$$

Relative changes in phase velocity and wavenumber are equal (apart from a sign). For this reason the parameters $\Delta k_{t,n}$ and $\Delta k_{a,n}$ are specified in percentage relative to $k_{t,n}$ and $k_{a,n}$ respectively.

Three examples of such diagrams for a perturbation $\Delta k_{t,n} = 1\%$, damping $\varepsilon = 1\%$ and different values of 'box width' $\Delta k_{a,n}$ are shown in figure 2.3.5. dk_1 and dk_2 are transformed to phase velocity values in [km/s]. This facilitates the interpretation of the diagrams in terms of phase velocity differences. Two clusters of points are visible, one for modes with a positive and one for modes with a negative offset. The mean and variance of these two clusters are calculated and plotted as a function of box width $\Delta k_{a,n}$ in figure 2.3.6a and as a function of damping (in a calculation with $\Delta k_{t,n} = 1\%$ and $\Delta k_{a,n} = 2\%$) in figure 2.3.6b. In the following we will discuss the influence of a priori knowledge on the measurements with the aid of figures 2.3.5 and 2.3.6.

If $\Delta k_{a,n} \leq \Delta k_{t,n}$ (the box width of $P(k)$ is less than the difference between true and assumed mode location) the a priori location determines the final solution, but this influence diminishes rapidly with increasing box width. For a box width of 2% is dk_1 on average close to zero. For $\Delta k_{t,n} = 2\%$ the results remain essentially the same. In realistic situations the error in higher mode phase velocities is assumed to be 1 to 2% (Nolet and Panza, 1976). We therefore adopt a conservative box width of 3% or more. This choice minimizes the influence of a priori knowledge.

The dependence of ε is illustrated by figure 2.3.6b. A minimum is detected near $\varepsilon = 0.1\%$, and from this value the error dk_1 increases rapidly with decreasing value of ε. The algorithm becomes unstable. If $\varepsilon > 0.1\%$ performance is somewhat worse, but remains within reasonable limits (.02 km/s).

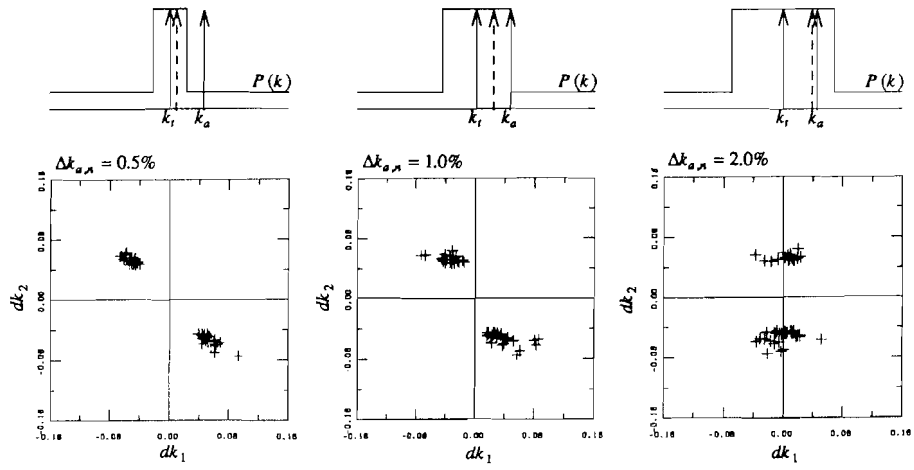

Figure 2.3.5. Test results for $\Delta k_{t,n}$=1%, damping ε=1% and box widths $\Delta k_{a,n}$=0.5%, 1% and 2%. The lower three figures show dk_2 as a function of dk_1, the upper three figures show the situation around one specific mode. The dashed arrow represents the measurement.

One can conclude that a priori information can be incorporated in the stacking procedure without biasing the result. The only constraint is that the uncertainty in the a priori knowledge, i.e. the width of the boxes in the a priori function, is larger than the expected error in the measurements and that the damping parameter ε is not too small.

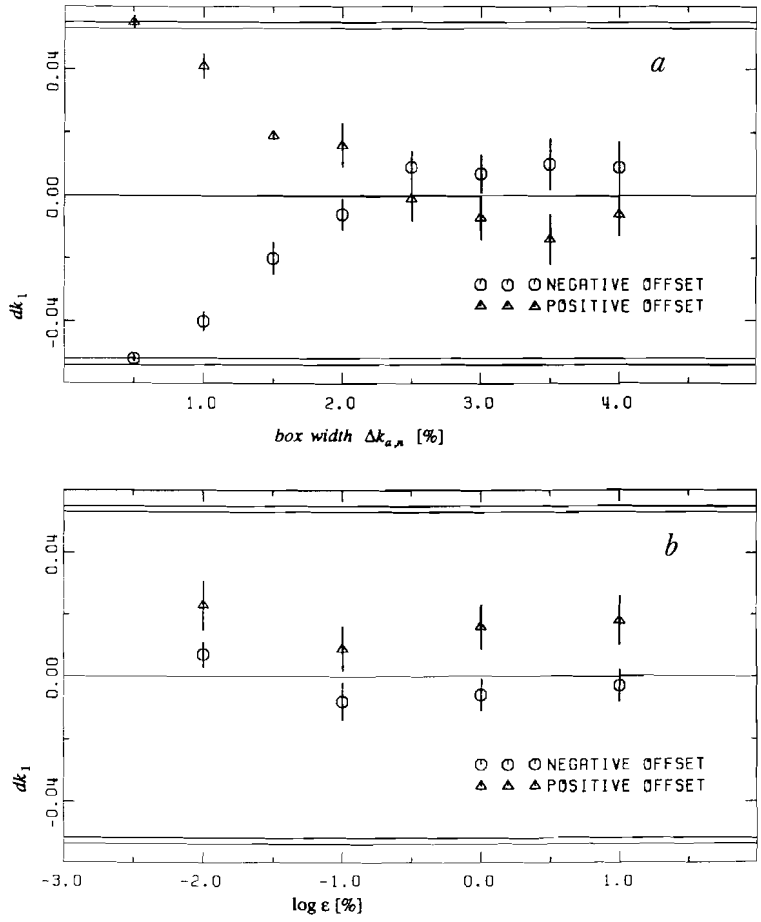

Figure 2.3.6. Difference between true and measured mode location (dk_1) averaged over measurements of 7 modes at 14 frequencies as a function of box width $dk_{a,n}$ (top figure) and as a function of damping parameter ε (bottom figure). Vertical bars indicate the standard deviation. Values for dk_2 are restricted to two regions at ±[.052,.054].

The choice of the damping parameter depends on the amount of noise present in the signal. The main source of noise comes from the aliasing lobes of the array response function and is dependent on station configuration, so no unique value can be assigned to ϵ, its optimum value should be experimentally determined in each analysis. In the next section we will compare different algorithms and the effect of the PDFT estimator on the mode separation diagram will be discussed.

Comparison of proposed algorithms:

Now we are in the situation where we can compare the performance of the different algorithms on the synthetic dataset. This comparison can be carried out in the same way as described in the last section, namely by measuring the difference between true and measured phase velocities: Δv_f. The algorithms we will use are:

[a] DFT stack

[b] DFT stack with CLEAN

[c] PDFT stack

One mode separation diagram, calculated for a constant frequency value, produces m phase velocity values for m modes. The mean and variance of these values are plotted in figure 2.3.7 as a function of frequency, or in this case: period. From this figure we can see that the PDFT and original DFT stack give comparable results, but that CLEAN produces outliers for periods lower than 30 seconds. This can be expected since the algorithm is based on the assumption that there are only a few modes present (Schwartz, 1978), while at increasing frequency more modes will appear in the mode separation diagram. A selection of the accompanying mode separation diagrams is shown in figure 2.3.8.

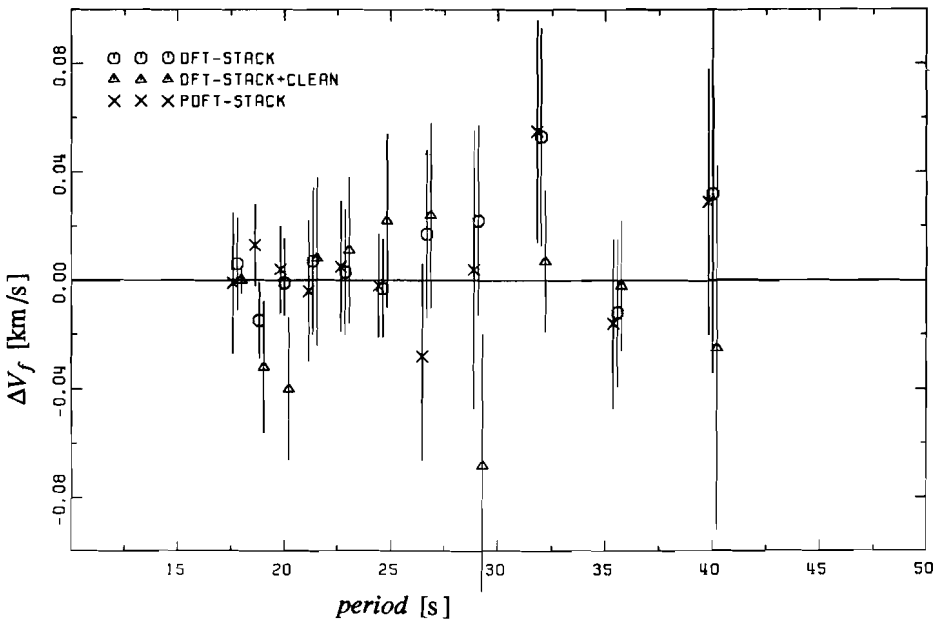

Figure 2.3.7. Mean and standard deviation of v_f for 7 higher modes as a function of period. For sake of clarity an offset is introduced along the period axis. Groups of three measurements belong to the period of the center of this group.

The effect of the clean algorithm on the mode separation diagram is that one extra mode (mode 4) is resolved. Unfortunately, this has as a consequence that the first and second mode give biased results. The PDFT estimator clearly enhances the energy around the modes, but if ε becomes too small (case d.), energy is smeared out. For this test we calculated 14 mode separation diagrams. Each diagram contains 7 higher modes and thus represent many different situations of possible mode-mode interference effects and relative excitations. This test is therefore thought to be representative for the general situation we encounter in practice and not only for the used synthetic data set. The accuracy in the measurements is not significantly improved when using the PDFT estimator, but the increase in the signal to noise ratio is very helpful in identification of the modes.

For the measurements, presented and discussed in the next chapter, we use a DFT stack first to get an impression of the quality of the data and then a PDFT stack with different values for ε.

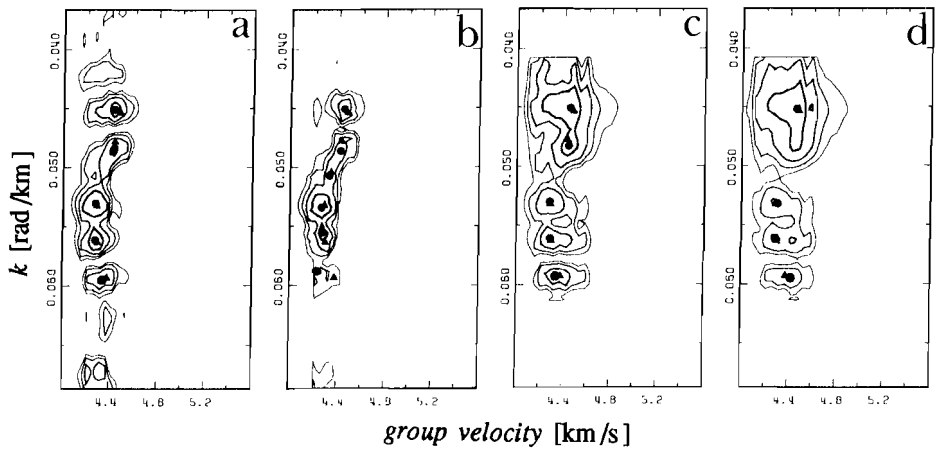

Figure 2.3.8. Mode separation diagrams at a period of 22.85 seconds for: a. DFT stack;b. DFT+clean; c. PDFT stack with ε=.1%, box width $\Delta k_{a,n}$=5% and perturbation $\Delta k_{t,n}$=1% and d: ε=.01%, box width $\Delta k_{a,n}$=5% and $\Delta k_{t,n}$=1%.

3. ANALYSIS OF NARS DATA

In this chapter we will present the NARS data that are used for higher mode surface wave analysis. Results are presented in the form of a phase velocity dataset for Rayleigh and Love fundamental and higher modes. In addition, a shear wave travel time dataset, compiled from ISC bulletins, is presented. It is used to constrain the shear velocity in the upper part of the mantle.

3.1 Data

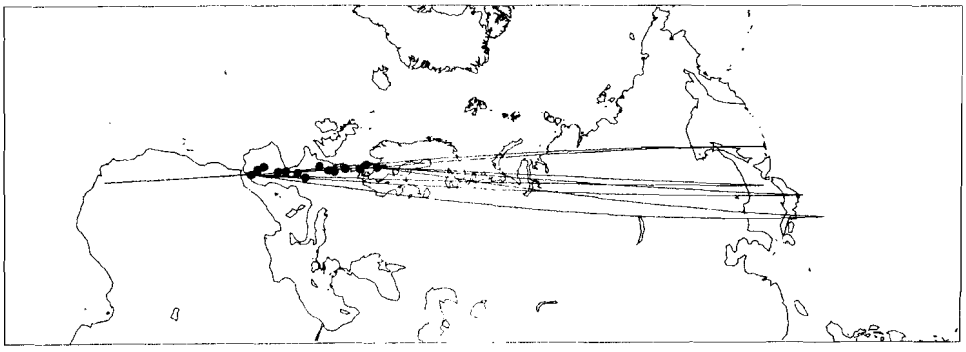

Figure 3.1.1. Location of earthquakes used in this analysis.

For optimal analysis of higher modes, earthquakes must be located near the great circle through the NARS stations. During 1983,1984 and 1985 three Japanese events and one Kurile event (see table 3.1) were recorded in a sufficient number of NARS stations (7 or more) to carry out a higher mode analysis. One additional Japanese event (26/5/83) has been used that was recorded with good quality records in only 6 stations. The reason to include this event is that its location coincides with the event of June 21, 1983 and their moment tensor solutions are very similar, so an attempt was made to process these two events together in one stack. Surprisingly one event in NW Africa occured on the great circle at the end of 1983 and this event was recorded in 7 stations.
Higher mode surface wave excitation is most effective for a source at intermediate depth.

Unfortunately none such event with sufficient magnitude occured in the first three years of NARS's existence.

Figure 3.1.1 shows the location of the events. The NW Africa (22/12/83) and Kurile (24/03/84) events are situated precisely on the great circle through the NARS array. The other Japanese events deviate in azimuth with a maximum of 12 degrees for the March 6, 1984 event. Since this is considerably less than the maximum deviation in azimuth in previous studies, which gave good results, we assume that we can neglect the variation of the initial phase. This simplifies the application of the stacking technique. The vertical component sections of the analysed events are displayed in figures 3.1.3 to 3.1.5. The horizontal components, although less stable, were used to collect a Love wave dataset.

The data were checked for possible timing errors and polarity reversals by comparison of P,S onsets and surface wave polarities along the array. Events recorded during 1983 do not contain minute marks on the EW component. In this case the onset times of P and S arrivals were calculated using the PEM-C model and compared with the data. Epicenter determinations have been taken from the ISC bulletin.

The radial and transverse components of the seismograms of the Honshu/Kurile events are displayed in figures 3.1.6 to 3.1.10. The horizontal components of the NW Africa event were too unstable to be included in the dataset.

Table 3.1: List of events used in this analysis.
The last column gives the number of stations that recorded the event.

date	origin time	lon	lat	depth	mb	Region	# stat.
26/05/83	2:59:58.8	139.09E	40.48N	16	6.6	Honshu	6
21/06/83	6:25:26.8	139.10E	41.35N	6	6.5	Honshu	8
22/12/83	4:11:29.3	13.51W	11.85N	11	6.3	NW Africa	7
06/03/84	2:17:21.0	138.92E	29.35N	454	6.1	E. Honshu	9
24/03/84	9:44:02.3	148.12E	44.04N	42	6.1	Kuriles	10
18/09/84	17:02:40.7	141.64E	34.01N	20	6.5	Honshu	9

The vertical and radial component of the shallow Japanese/Kurile events show a pulse like arrival with a group velocity of approximately 5.2 km/s and dominant period of 40 seconds between the predicted SS and SSS (see fig 3.1.2). Nolet (1976) showed that this arrival can be caused by a simultaneous constructive interference for both horizontal wavenumbers and radial orders, or when group velocities of adjacent modes are well separated but contain an independence of frequency in a wide frequency interval. The transverse component shows a similar phase at a group velocity of 4.5 km/s. Nakada and Hashizume (1983), in a study of the upper mantle beneath the Canadian shield, used similar pulse like signals as higher-

mode surface wave data and identified the signal at the transverse component as a S_a phase. A similar phase on the vertical and radial component with group velocity between 4.6 and 4.8, called the Rayleigh type S_a phase, can not be found in our dataset.

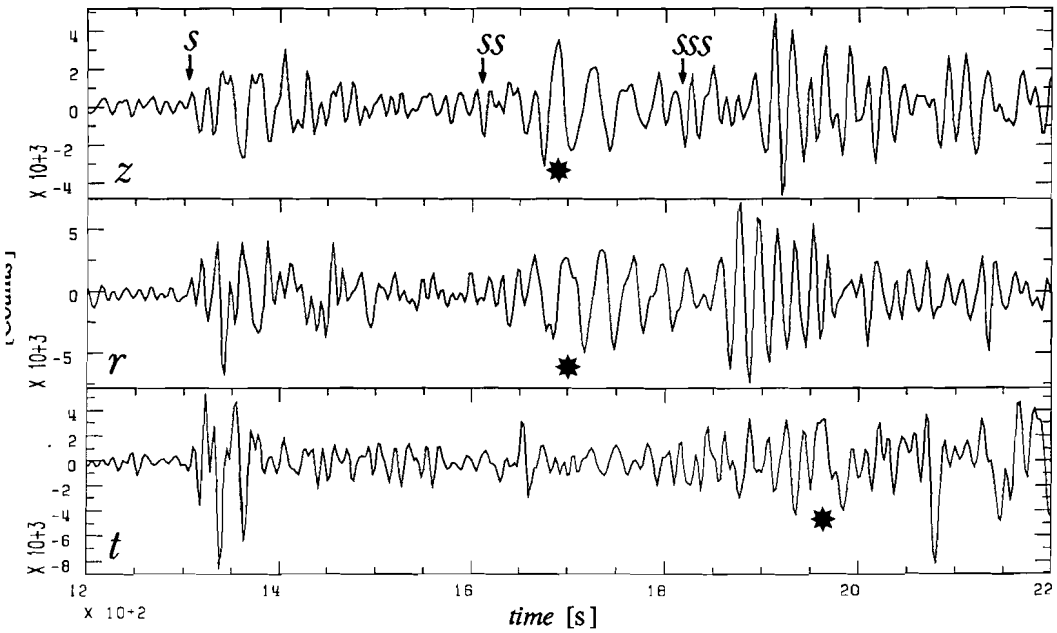

Figure 3.1.2. Vertical, radial and transverse component of event 24/3/84 recorded in station NE04. Marked with a star are the pulse like arrivals

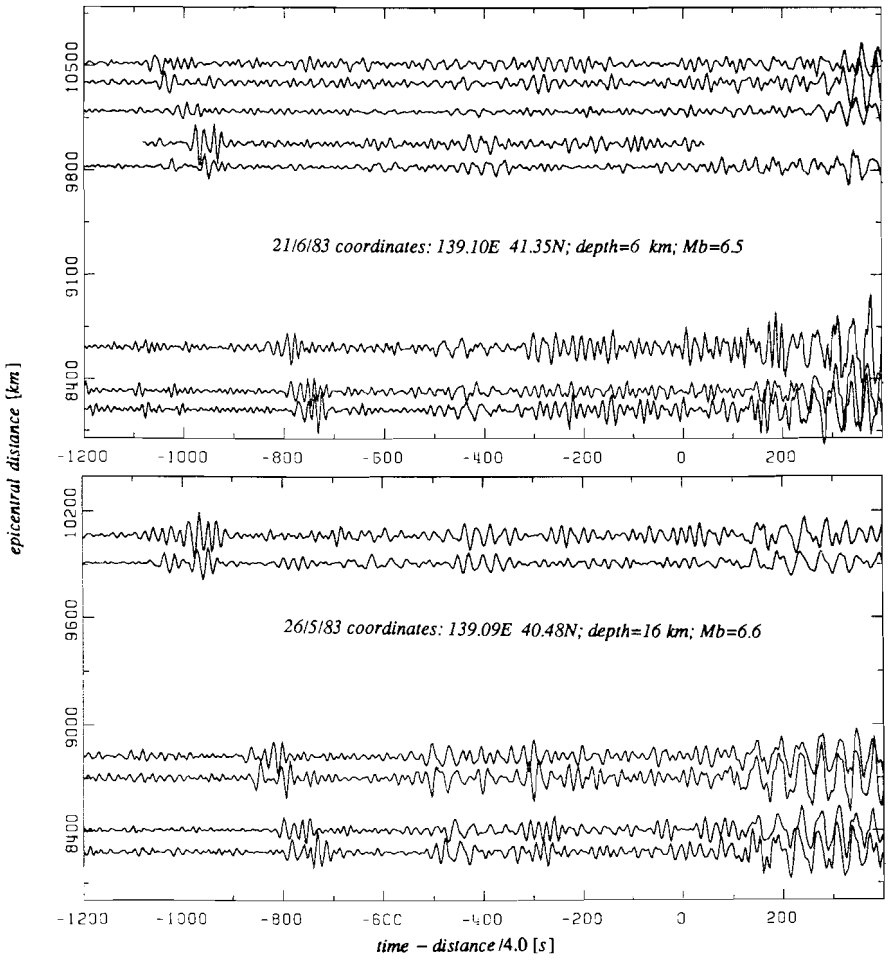

Figure 3.1.3. Vertical component NARS recordings of the events listed in table 3.1

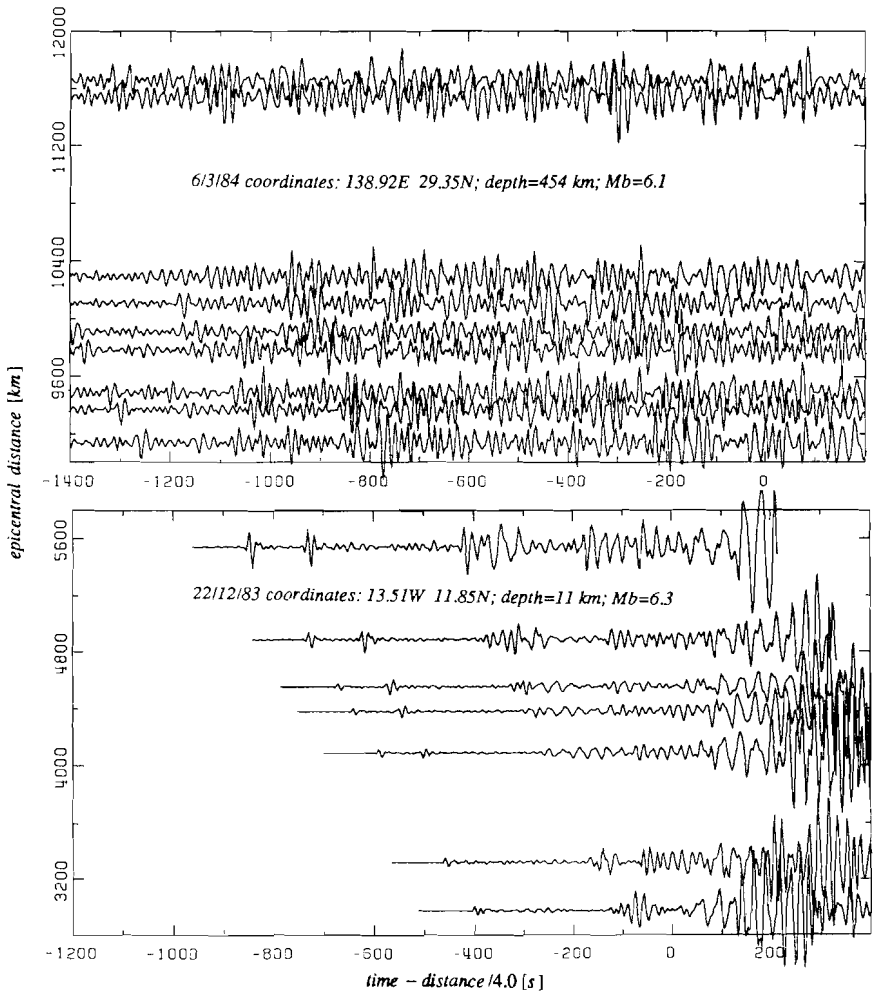

Figure 3.1.4. Vertical component NARS recordings of the events listed in table 3.1

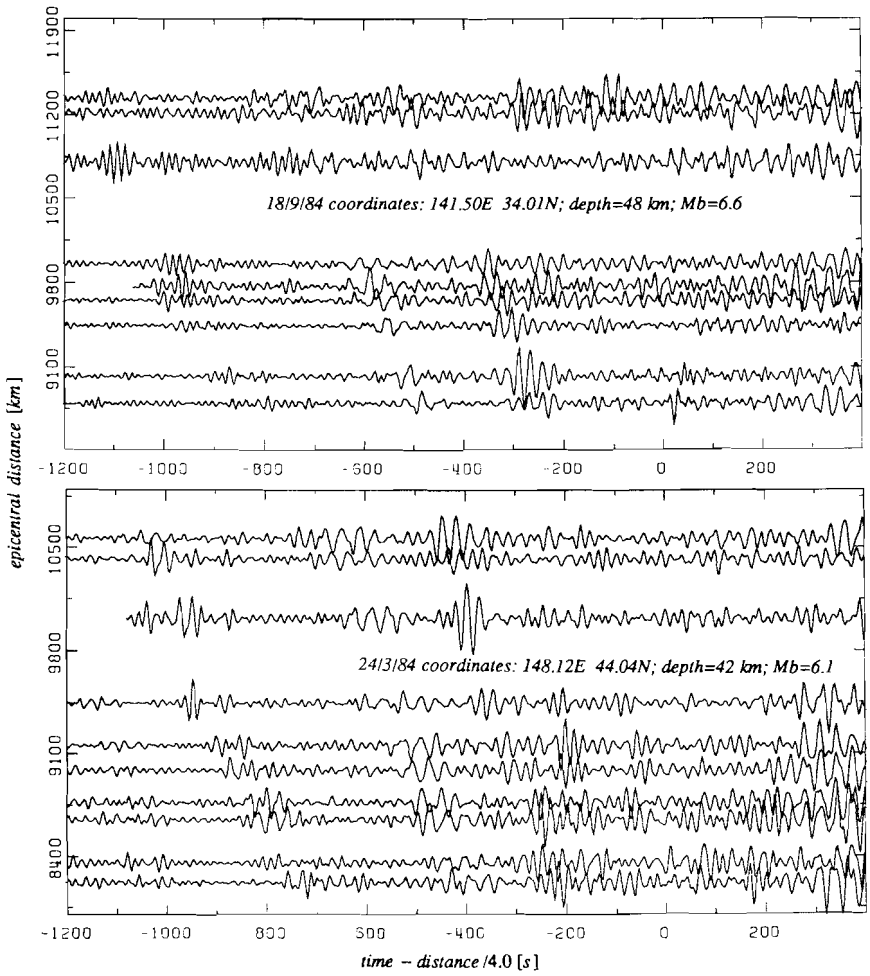

Figure 3.1.5. Vertical component NARS recordings of the events listed in table 3.1

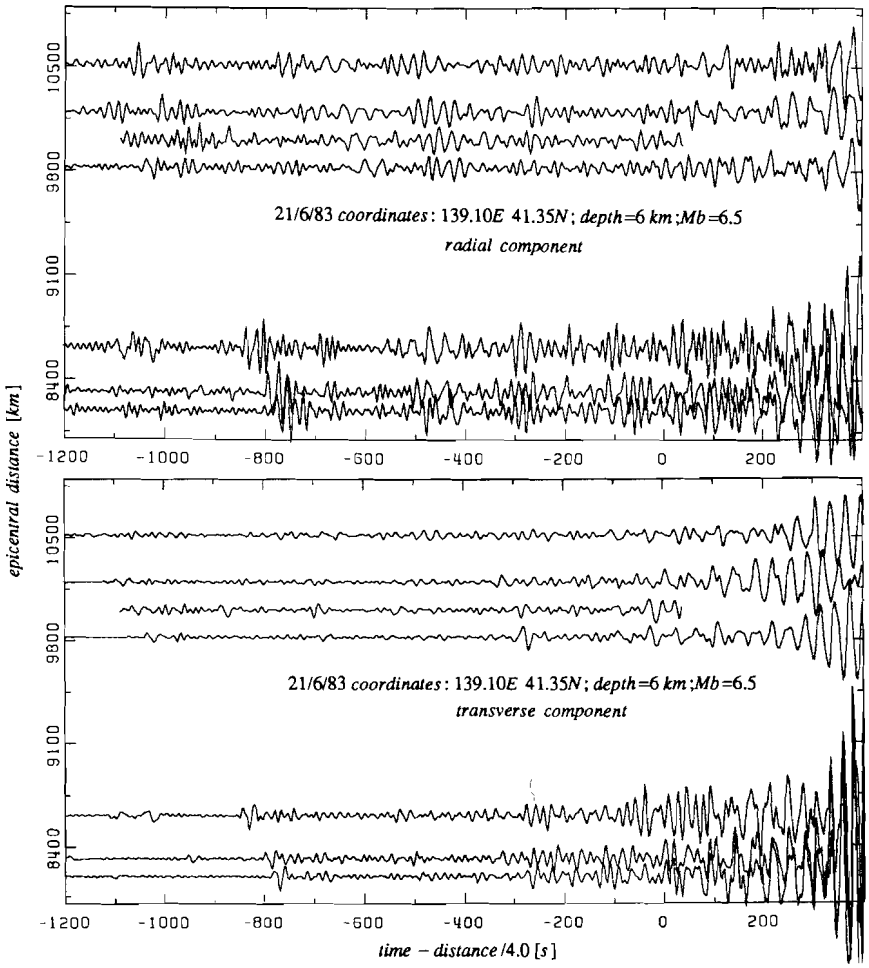

Figure 3.1.6. Radial and transverse component NARS recordings of the events listed in table 3.1

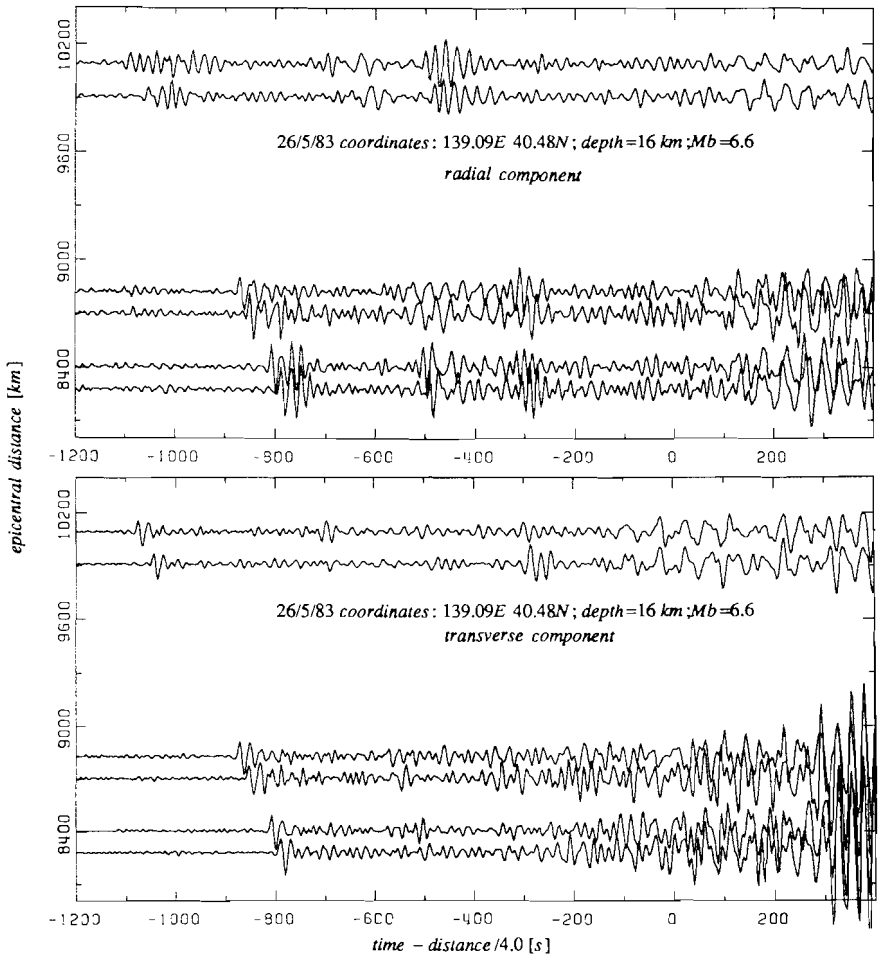

Figure 3.1.7. Radial and transverse component NARS recordings of the events listed in table 3.1

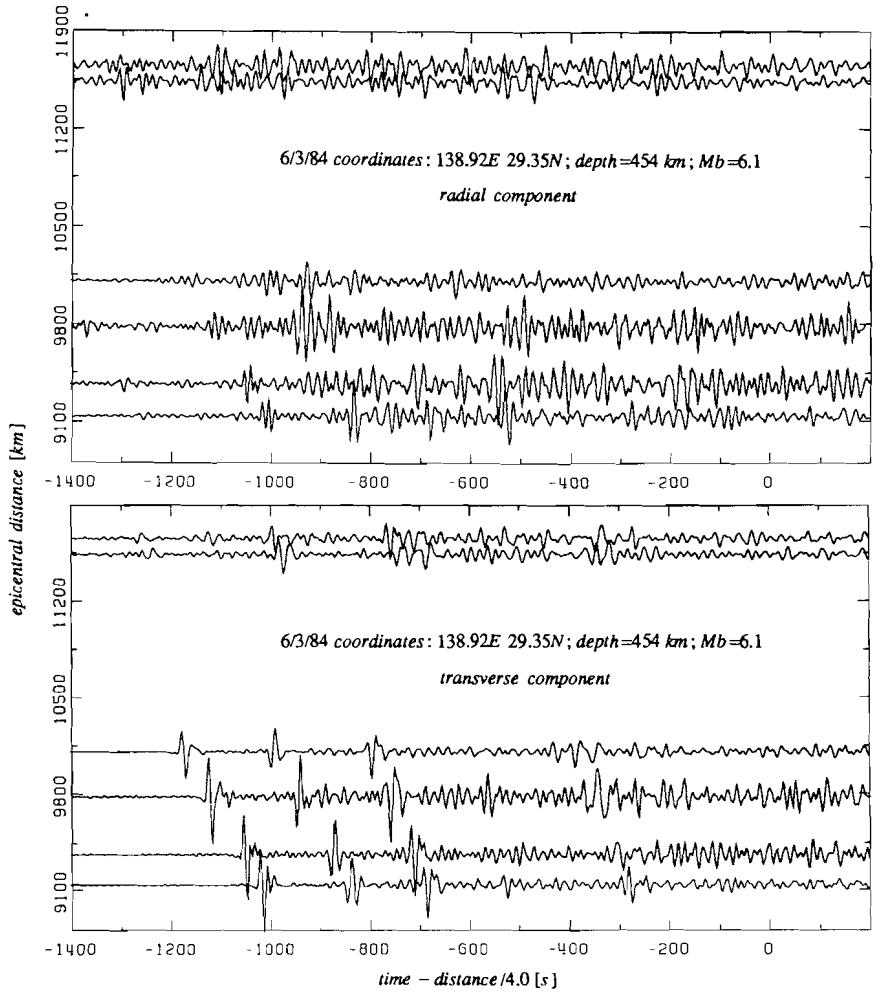

Figure 3.1.8. Radial and transverse component NARS recordings of the events listed in table 3.1

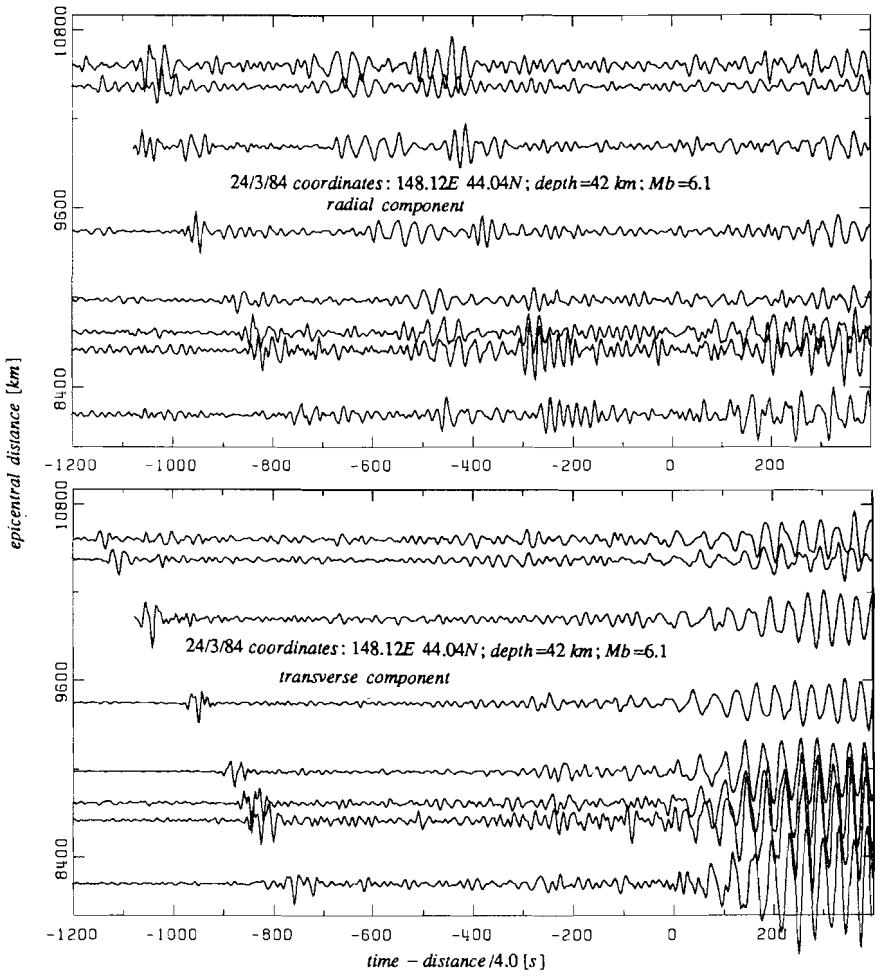

Figure 3.1.9. Radial and transverse component NARS recordings of the events listed in table 3.1

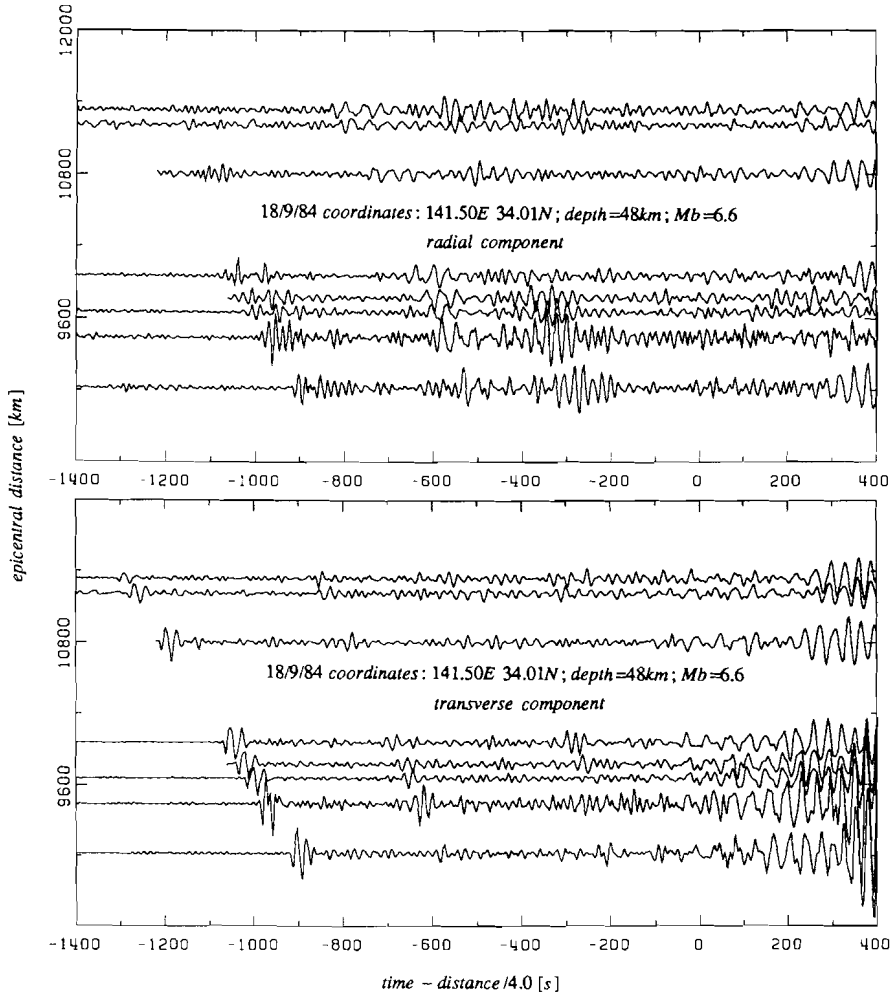

Figure 3.1.10. Radial and transverse component NARS recordings of the events listed in table 3.1

3.2 Measurements

3.2.1. Higher mode surface wave measurements

Vertical component recordings of the 6 events of table 3.1 have been analysed in order to obtain Rayleigh wave phase velocities. Transverse components could only be used for 2 Japanese events. For each event mode separation diagrams of phase- versus group velocity have been calculated for 23 frequencies between 20 and 70 mHz. These measurements are obtained in two runs of 14 frequencies, each run with a different group velocity window width, with 5 overlapping frequencies between 30 and 50 mHz. In this way the influence of the width of the group velocity window could be checked. Modes, showing up as energy maxima, are automatically picked from the diagrams in the neighbourhood of theoretical values predicted by the M7 model (Nolet, 1977). Care has been taken that the region searched for a maximum is sufficiently large to rule out any bias by the M7 model. All diagrams are visually inspected to check whether a real maximum is present and not biased by interference effects of neighbouring modes. A first analysis is done without any filtering or weighting to get an impression of the data quality. Then several runs with the PDFT estimator applying different values for the damping parameter are carried out to optimize these results. These data were removed whenever repeated measurements with varying damping parameter produced inconsistent results. Application of the stacking technique assumes a laterally homogeneous sub-surface structure. The path under study does contain some lateral variations (Spakman, 1986; Panza et al, 1980; Nolet et al, 1986d). We expect this phenomenon to express itself in a scatter of the measurements.

Rayleigh waves:

In order to get an impression of the reliability of the higher mode Rayleigh wave phase velocity measurements we calculated vertical component synthetic seismogram sections for all 6 events by means of mode summation, using mode 1 to 15 in the frequency range of 20 to 80 mHz. For the earth model we used the outcome of a preliminary analysis (WEPL1; Dost, 1986), modified by addition of traveltime information in the inversion procedure. At depths greater than 600 km the PREM model has been adopted. The synthetic sections show the observed pulse like signal at a group velocity of approximately 5.2 km/s. Figure 3.2.1 shows a flat part in the curves for mode 7 and 8 at periods between 30 and 40 seconds at the appropriate group velocity of 5.2 km/s. This confirms the secondly proposed nature of the signal in chapter 3.1.

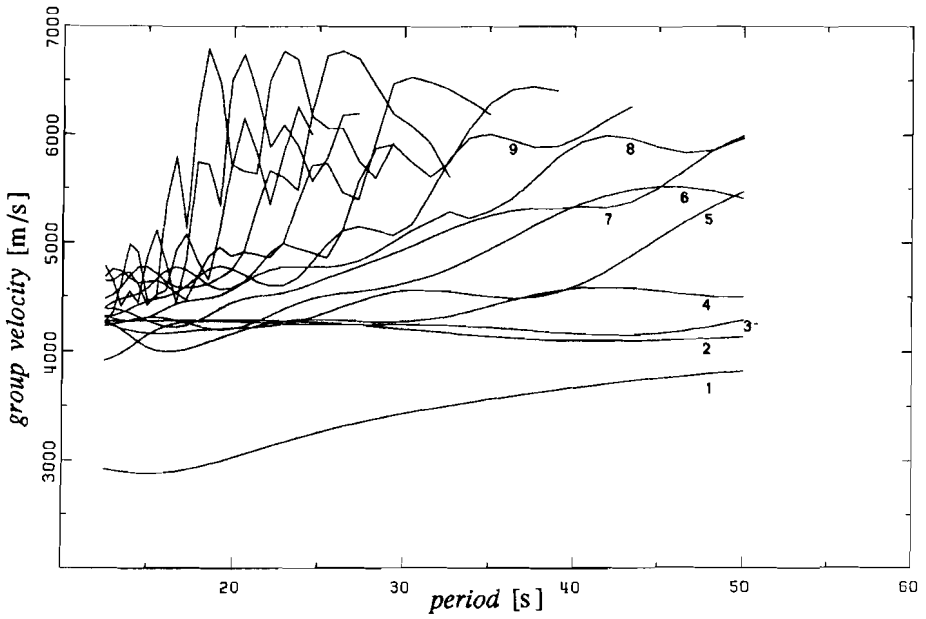

Figure 3.2.1. Group velocity as a function of period for the modified WEPL1 model used in calculation of synthetic seismogram sections.

The results of the analysis of the synthetic sections are displayed in figure 3.2.2. These measurements have been made without any weighting or deconvolution. From this experiment we can conclude that:

[a] The first higher mode is badly measured, except for the Kurile event (24/3/84). A plot of the relative excitations of the different modes, as shown in figure 3.2.3, indicates that this is due to a bad excitation. Side lobe effects from neighbouring modes can strongly influence the measurements. Side lobes coming from the interfering modes 5-8 can also generate features in the neighbourhood of mode 1, and can be recognized by their high group velocity values. Identification of the modes becomes more difficult at higher frequencies where group velocity curves of the various modes approach each other.

[b] The second and third mode can be accurately determined. It is however necessary to average phase velocities from all events in order to obtain an unbiased result.

[c] From mode 4 onward only the high frequency part of the measurements (<25s) gives unbiased results. Since we can model the previously described interference pattern that causes the bias in the phase velocities, we can try to discriminate between different earth models obtained after inversion by comparing the waveform of the pulse

like arrival with synthetics.

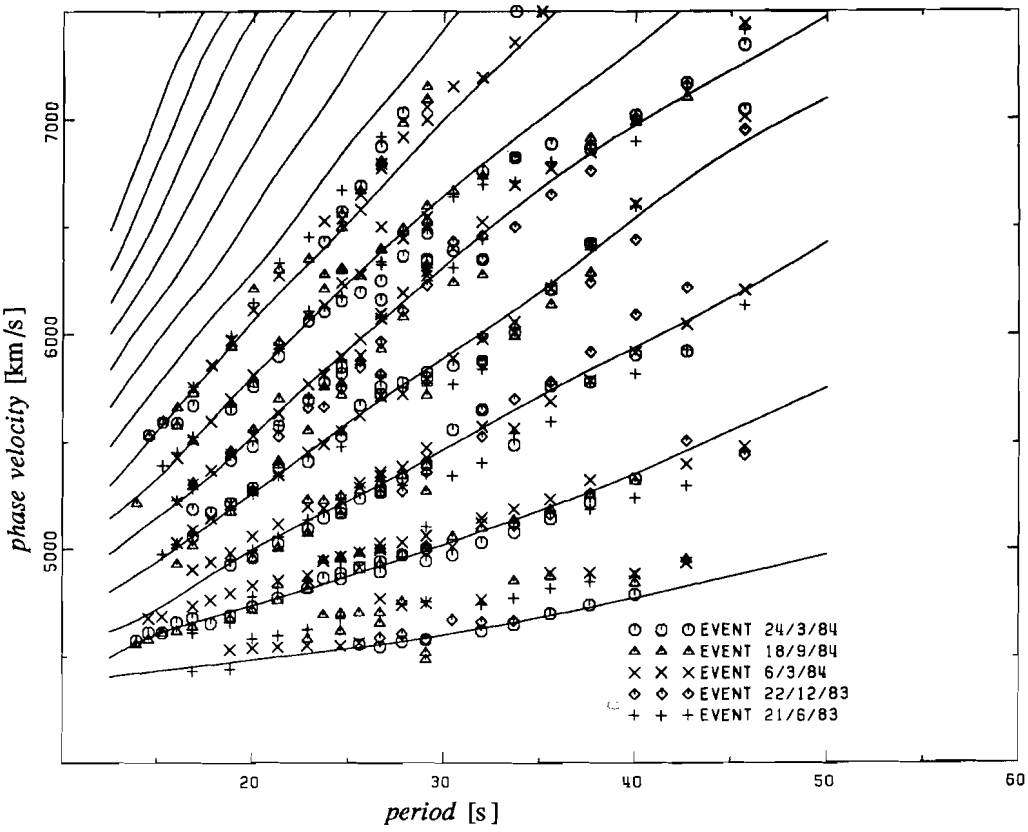

Figure 3.2.2. Phase velocity measurements on synthetic seismogram sections The different mode branches are labeled.

This analysis gives us some insight in the reliability of our measurements. We will present and discuss the measured phase velocity data set with the results from our synthetic experiment in mind. Rayleigh wave measurements that were judged to be reliable are presented in figure 3.2.4 and compiled in appendix D.

The fundamental mode Rayleigh wave is measured up to 50 mHz (20 seconds). The reason to exclude higher frequencies is that the penetration depth of surface waves decreases with increasing frequency, thus making the surface waves more susceptible to lateral heterogeneity. For the fundamental mode at frequencies higher than 50 mHz this gave rise to an

unacceptable scatter in the phase velocity measurements. The same phenomenon is observed for the first higher mode.

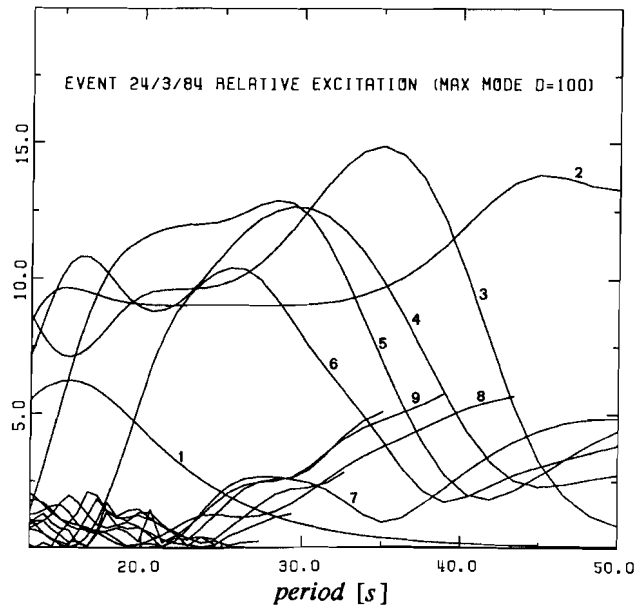

Figure 3.2.3. Relative excitation of mode 1-15 for the synthetics of event 24/3/84 as a function of period. Curves for mode 1-9 are marked.

The fact that the second and third higher mode do not show this large scatter gives us confidence that the deeper structure is much smoother. The first higher mode shows a large difference in phase velocity between the 21/6/1983 Honshu event and the other events for periods between 35 and 50 seconds. This is also the case for mode 2 and 3. As can be seen from the data (figure 3.1.3.) the two events in 1983 both suffer from a lack of data in the central part of the array. Since these two events have nearly the same location and their moment tensor solutions are very similar an attempt was made to process these events together in one stack. For the first two modes the phase velocities are reduced and match the values for the 1984 events between 30 and 40 seconds. Between 40 and 50 seconds this is not the case. This last period range is at the low frequency edge of the interval where we can accurately measure higher mode phase velocities with the NARS array. Therefore we did not include phase velocities between 40 and 50 second period from the first two higher modes into our data set. It should be noted that this is exactly the period range where there

are differences in measurements between Cara et al. (1980) and Nolet (1977). Moreover, even the values are comparable (see table 3.2).

Table 3.2 Comparison of phase velocity measurements.

T [s]	v_f [km/s] for the 2^{nd} higher mode				
	Cara et al. (1980)	Nolet (1977)	21/6/83	24/3/84	18/9/84
42.67	5.30	5.50	5.53	5.35	5.31

For mode 4 to 6 the measurements for periods $\leq 25s$ are thought to be reliable. Between 25 and 50 seconds strong interference effects play a major role as seen at the synthetics.
The difference between the preliminary data set (Dost, 1986) and our final dataset is:

[a] The preliminary data were obtained with a simple version of the PDFT estimator. In this version we assumed that all modes are confined to one finite wavenumber band. There was no specific information involved about the modes separately.

[b] Higher mode measurements were restricted to the frequency range of 30 to 70 mHz. The new dataset is extended to the lower frequency part (up to 20 mHz for the third higher mode). Higher mode phase velocity measurements for frequencies ≤ 20 mHz resulted in a large scatter because of the limited length of the array.

[c] Fundamental mode measurements from Seidl (1971) have been adopted in the preliminary dataset. At present they have been substituted by newly measured values. Measurements from 6 to 50 mHz (20-160 s) show a good agreement with Seidl's values. There is however considerable scatter between 14 and 20 mHz (50 and 70 s).

[d] In the final dataset S traveltimes are included. This is described in the chapter 3.2.2.

Love waves:

An attempt has been made to measure higher mode Love wave phase velocities. Reliable transverse components, measured in at least 7 stations, could be obtained for the 24/3/84 Kurile event and the 18/9/84 Honshu event (see figures 3.1.9 and 3.1.10). The transverse components of the 21/6/83 Honshu event were not used, because of their bad coverage (see figure 3.1.7). Results for the fundamental and first four higher mode phase velocity measurements are shown in figure 3.2.7 and compiled in appendix D. For the fundamental mode the group velocity is also shown. The measurements are compared with a Love wave phase velocity data set by Cara et al. (1980). This data set is based on measurements of one Japanese event recorded in western Europe including scandinavia. In addition we compare our results with Love wave measurements for North America, based on recordings of two Tonga events (Leveque and Cara, 1983).

The fundamental mode shows a continuous dispersion curve for the 24/3/84 Kurile event, but a jump in phase and group velocity at 25 mHz for the 18/9/84 Honshu event. The cause of this jump can be recognized from the data (see figure 3.2.5), bandpass filtered between 20 and 30 mHz. The Kurile event shows a undisturbed dispersed wavetrain, while the Honshu event clearly shows a beating effect at a group velocity of approximately 3.6 km/s, which is the measured group velocity coinciding with the jump in phase velocity. This effect can be caused by multipathing due to lateral heterogeneity. Comparison with fundamental mode phase velocities from Cara et al. (1980) shows that their measurements coincide with the results from the Honshu event up to 25 mHz. Unfortunately, their measurements are not extended to higher frequencies and we do not know whether they may be influenced by such a beating phenomenon. North American phase velocities are consistently lower, except in the vicinity of the jump. Again no comparison can be made for frequencies higher than 25 mHz, since no observations has been made in that frequency region so far.
The first higher mode shows a large scatter in phase velocity between 25 and 30 mHz. As can be seen from the bandpass filtered data (see figure 3.2.6) the beginning of a Sa phase can be recognized at a group velocity of 4.45 km/s for the Kurile event, but not for the Honshu event. This can be caused by the greater depth of the Kurile event, which is favourable for the excitation of this phase. However, an additional long period feature in the station with the smallest epicentral distance to the Kurile event, just preceding the Sa phase is presumably due to an instability of the horizontal seismometers. This will effect our measurements, but phase velocity measurements without this registration do not produce accurate results in this frequency range either. The second and third mode show a continuous dispersion curve. Comparison with Cara et al. (1980) show that their second higher mode phase velocities are influenced by interference effects of the second and third mode. The phase velocities for Northern America are very close to our measurements.
Because of the very limited dataset and the anomalous features in the determination of the phase velocities just described, we decided not to invert simultaneously for Love and Rayleigh wave phase velocities, but await more accurate measurements.

Our dataset for the inversion thus consists of:

[1] Fundamental mode Rayleigh wave phase velocities from 6 to 50 mHz.

[2] First higher mode Rayleigh wave phase velocities from 25 to 45 mHz,

[3] Second higher mode Rayleigh wave phase velocities from 25 to 70 mHz

[4] Third higher mode Rayleigh wave phase velocities from 22 to 70 mHz

[5] Fourth to sixth higher mode Rayleigh wave phase velocities from 45 to 70 mHz.

Additionally a shear velocity (Sn) data set is used in the inversion. The motivation for and compilation of this data set is the subject of the next section.

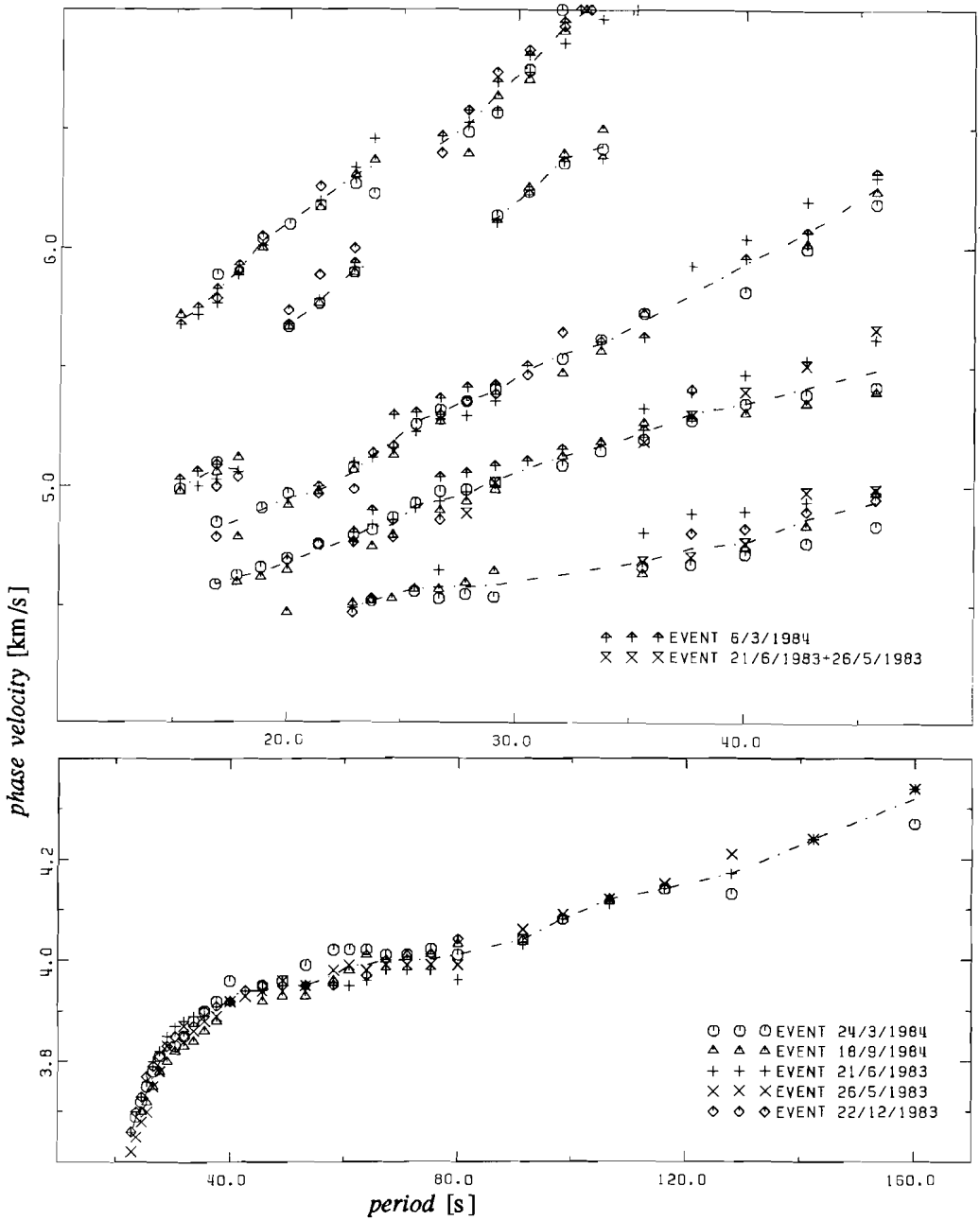

Figure 3.2.4. Fundamental and higher mode Rayleigh wave phase velocity measurements. The dashed line indicates average values used in the inversion.

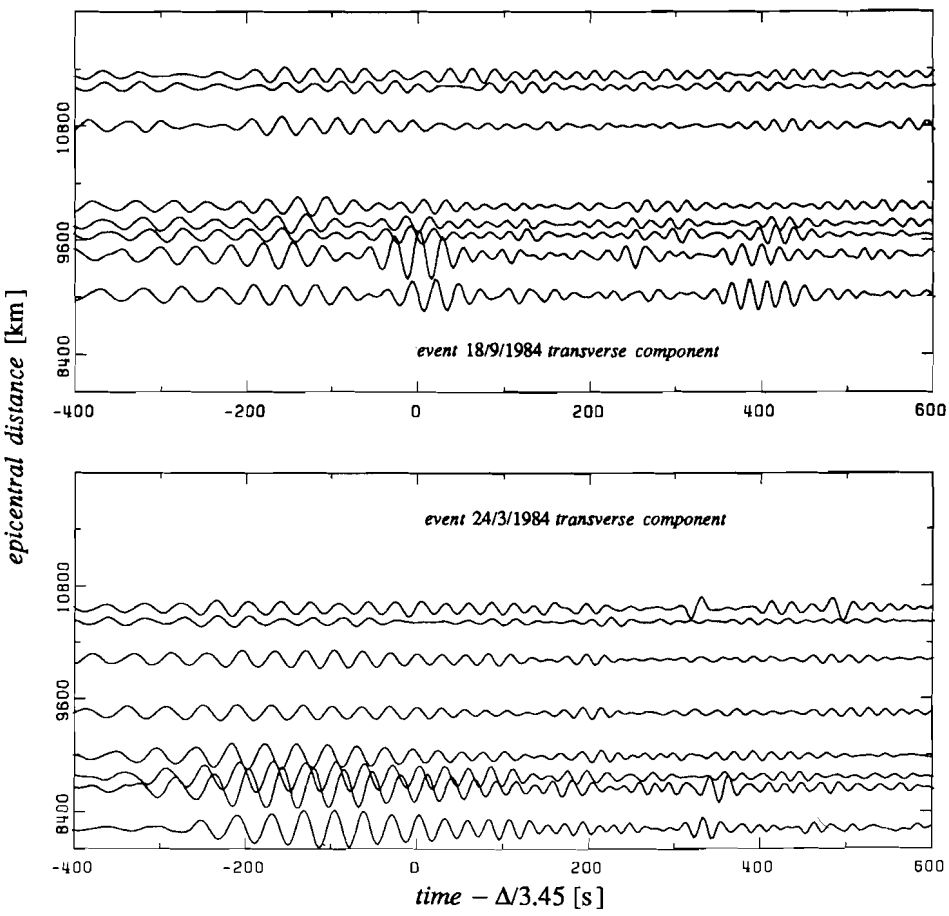

Figure 3.2.5. Comparison of transverse components of NARS registrations of event 24/3/84 and 18/9/84 near the fundamental mode Love wave. The time axis is reduced by a factor Δ/3.45.

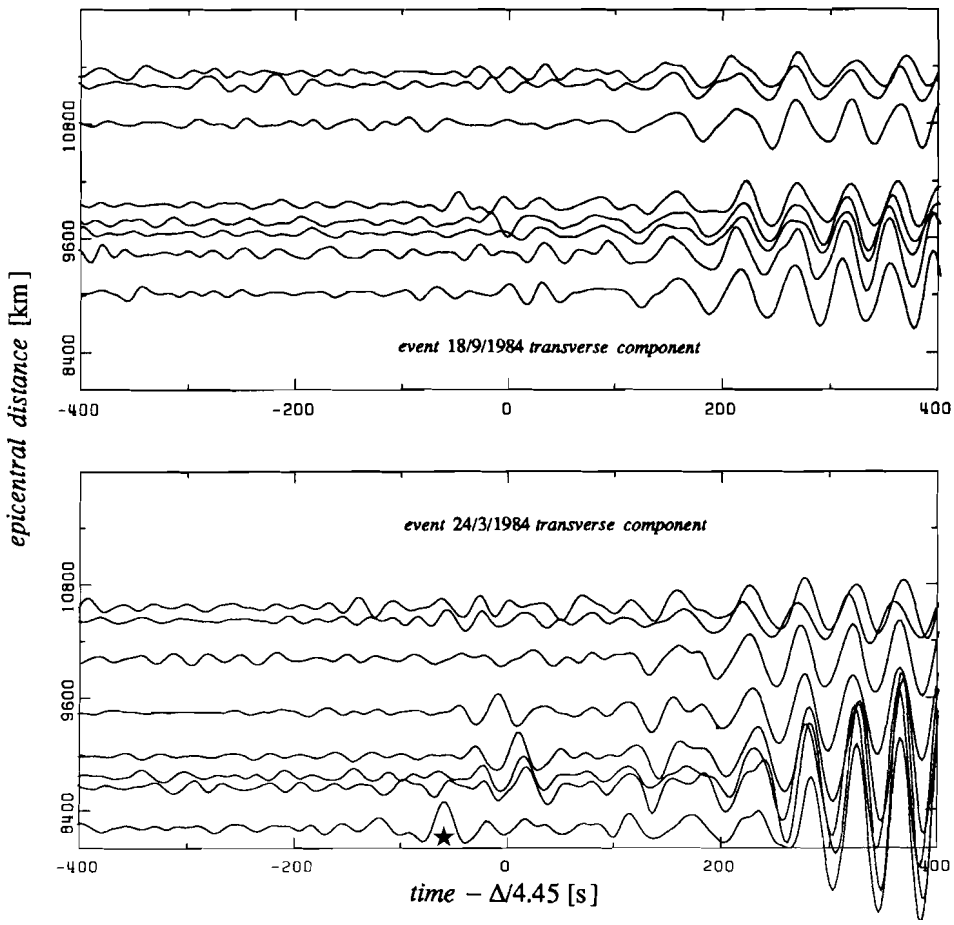

Figure 3.2.6. Comparison of transverse components of NARS registrations of event 24/3/84 and 18/9/84 near the first higher mode Love wave. The time axis is reduced by a factor $\Delta/4.45$. Marked by an asterix is an instability in the transverse component recording.

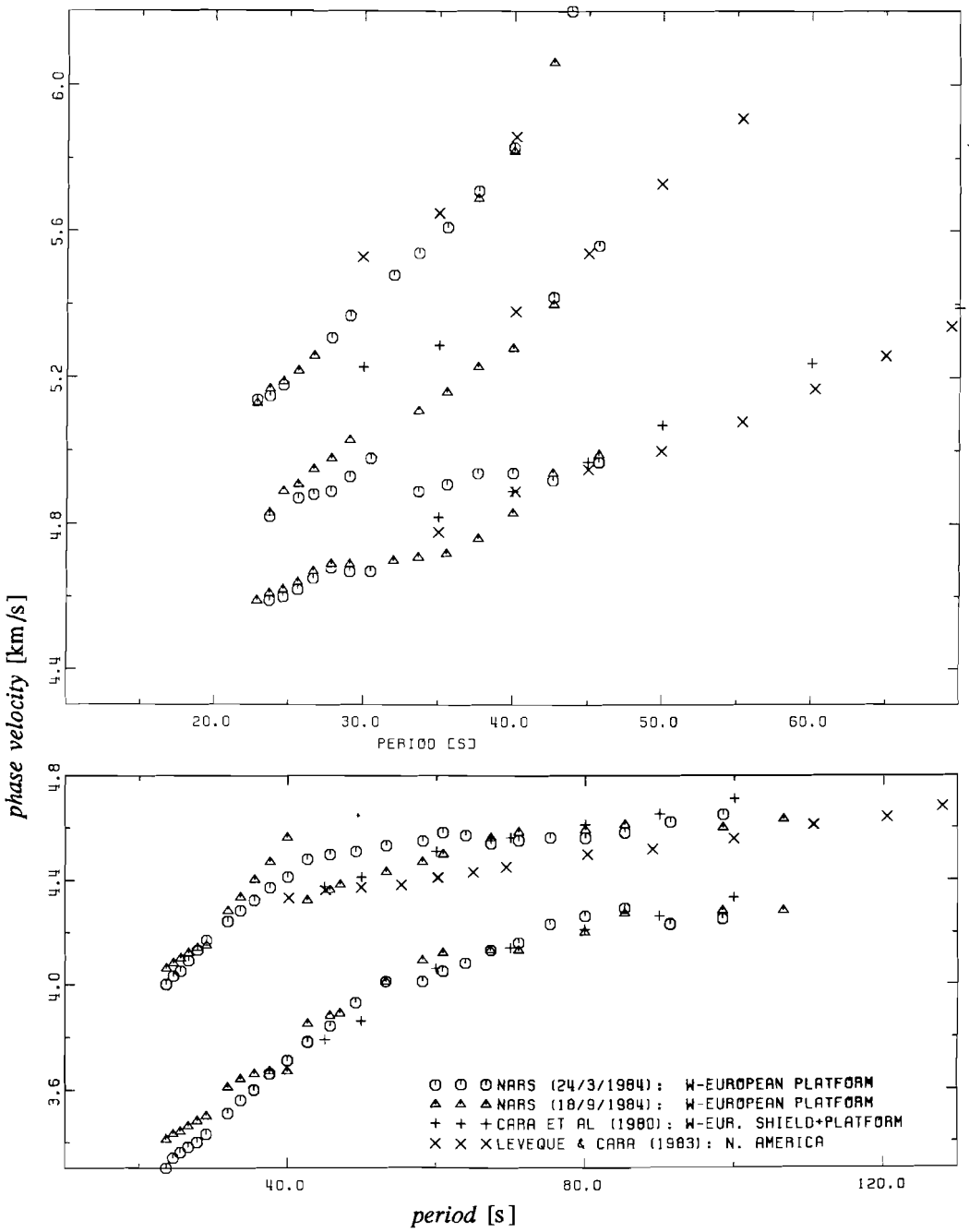

Figure 3.2.7. Fundamental and higher mode Love wave phase velocity measurements.

3.2.2. Traveltimes

An additional independent source of information about the upper mantle shear velocity structure that can be included in our inversion procedure are Sn traveltimes from selected European events. Several interpretations have been given to this Sn wave, e.g. a head wave refracted at the base of the Moho, but Mantovani et al. (1977) show that an interpretation as a wave that is guided by the lithosphere and travels with a constant surface velocity is more consistent with the character of the phase. For shallow depths of foci and a model containing a low velocity zone, it was shown that the Sn phase can be interpreted as a lid-wave. This means that its energy is confined to the uppermost few tens of kilometers of the mantle.

Concerning the European continent there have been previous studies that incorporated shear wave traveltimes.

Lehmann (1961) compiled S readings and was able to demonstrate the existence of a low velocity layer in Europe, followed by a rise at 220 km depth. Her dataset consisted of ISS traveltimes and personal readings from four shallow events (two Italian, one Azores and one Greek) and 6 deep Rumanian earthquakes (130 km depth).

A difference in structure between western and eastern Europe was assumed in the study by Mayer-Rosa and Mueller (1973) who examined P and S times together with fundamental mode Rayleigh waves. Their conclusion was that in the upper 200 km a clear distinction could be made between the two regions.

Regional S arrivals are difficult to read and may show considerable scatter. Especially too large arrival times are to be expected due to a larger amplitude SSn phase that arrives after the Sn phase (Kennett, 1985). For selected events and stations that sample the structure under NARS we will try to infer a traveltime curve using ISC bulletins as a database. In the present compilation we will take care to minimize the influence of lateral heterogeneity and therefore neglect events in eastern Europe as well as events in Algeria and southern Spain (Spakman, 1986; see also Panza et al (1980) for anomalous Sn velocities in this last region). The remaining events and reduced traveltime curve are shown in figure 3.2.8.

No	date	epicentre	h	origin time
1	24/10/76	50.39N/3.92E	28	20:33:29.2
2	6/4/77	61.73N/2.30E	10	19:31:45.1
3	26/12/79	54.93N/2.78W	10	03:57:05.6
4	5/6/80	51.23N/5.74E	24	02:11:39.0
5	22/5/82	51.12N/5.85E	26	06:00:02.4
6	22/5/82	42.86N/1.87W	3	04:03:00.0
7	22/6/82	42.89N/1.94W	10	19:50:21.5
8	29/7/82	60.31N/1.93E	10	00:17:00.2
9	8/3/83	59.67N/5.20E	33	18:43:54.0
10	4/8/83	50.38N/4.33E	10	07:08:24.4
11	9/8/83	50.40N/4.29E	10	01:32:34.8
12	8/11/83	50.73N/5.31E	5	00:49:31.5
13	8/11/83	50.60N/5.38E	8	02:13:21.2
14	3/4/84	50.58N/2.49W	12	14:27:11.2
15	15/4/84	52.22N/3.31W	25	21:05:34.4
16	19/7/84	52.86N/4.17W	20	06:56:12.3

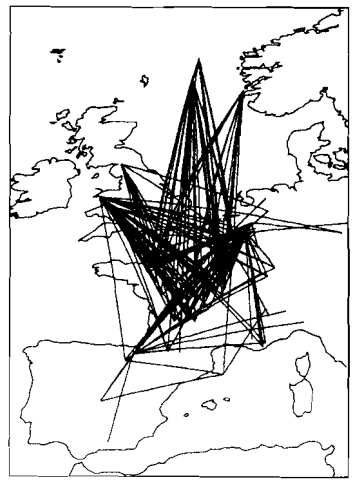

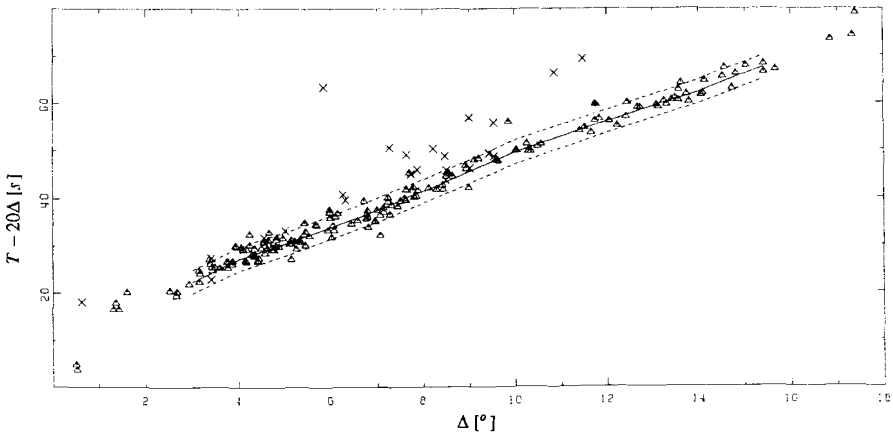

Figure 3.2.8. Top:list of used events and great circle paths. Bottom: Reduced Sn traveltime as a function of epicentral distance Δ. Solid line represents the inferred traveltime curve, dashed lines the assumed standard deviation. Data from two french events, event 6 and 7, are marked with a cross in stead of a triangle and are not used in construction of the traveltime curve.

The dataset contains mainly events in the North sea, United Kingdom, Belgium, the Netherlands and stations in France. The inferred traveltime curve is compatible with the majority of the data. A scatter in the measurements between 5 and 12 degrees is mainly due to 2 French events, number 6 and 7. In general regional French events give a large scatter in Sn traveltimes and are thus omitted. An average standard deviation in the traveltime curve of $\pm 2.5\ s$, as indicated in figure 3.2.8, is thought to be representative for our dataset.
One of the events, number 16, was also recorded by the NARS array in stations NE02 to NE07. This enabled us to check wether the Sn onset is clearly visible on a broad-band instrument or not. Vertical component registrations are shown in figure 3.2.9

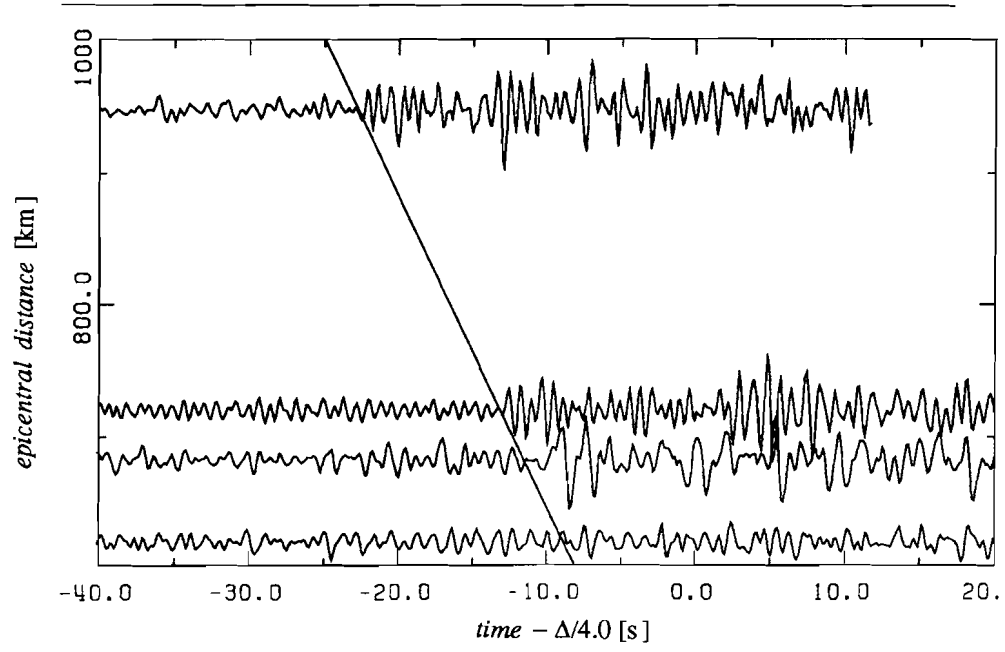

Figure 3.2.9. NARS registration of the 19-7-1984 United Kingdom event.

S phases are clearly observable at epicentral distances greater than 700 km. For shorter distance the onset is difficult to pick. These measurements have been incorporated in our compilation of regional traveltimes and are consistent with ISC determinations.

4. INVERSION

The dataset is inverted using the generalised inversion technique (Wiggins, 1972) with a sharp eigenvector cut off. In the inversion a trade-off exists between depth resolution and variance in the model parameters. The number of eigenvectors used in the inversion determines this trade-off. S velocity, v_s, and density, ρ, were inverted simultaneously after weighting them with a priori uncertainty. P velocity, v_p, is coupled to v_s with a fixed Poissons ratio. This is convenient since only the fundamental mode is weakly sensitive to v_p. One should keep in mind that surface waves are only sensitive to changes in the gradient of the density, not to absolute changes (Nolet, 1977). As an extra constraint, no change in surface gravity is allowed to result from the inversion. As a measure of the fit of a model to the data, relative residuals are calculated. This is the average root mean square of the difference between observed and calculated values (ξ) for the data divided by the standard error. Thus, for N data ξ corresponds to $(\chi^2/N)^{1/2}$ with χ^2 the more familiar statistical quantity Since $N \gg K$, the number of eigenvectors used in the construction of the model, the number of degrees of freedom is approximately N. Thus, when $\xi<1$ a model has been chosen that fits the errors in the data rather than the trend in the data. On the other hand, if $\xi>1$ a poor fit between the data and the model is obtained. Therefore we should aim at a relative residual $\xi=1$. Of course we might introduce at this stage sophisticated statistical techniques to decide whether the addition of an extra eigenvector is warranted by the data. We have, however, found it much more convenient to apply subjective judgement to decide whether we are near enough to $\xi=1$ and to avoid model features of doubtful reality. We shall make up for this by applying resolution analysis a posteriori. Resolution is calculated by introducing constant velocity changes over thick layers, thereby forcing the system to be overdetermined. The inversion then gives the variance in the model averaged over the specified layer thickness.

In the inversion procedure a starting model is required. One should be cautious not to influence results with a priori assumptions about e.g. a low density- or velocity channel in this starting model. The M7 model is an isotropic model. Cara et al. (1980) observed a possible anisotropy under western Europe. They based their observation on the incompatability of Love and Rayleigh wave phase velocities in this region. Mitchell (1984) mentions as possible alternative explanations for a Love/Rayleigh incompatability a laterally varying structure or a failure to include a sufficient number of layers in the inversion process. Since there is at the moment no proper Love wave dataset at hand for the west-European platform, we will interprete our data assuming an isotropic model.

Nolet's data sample the Scandinavian shield and the west-European platform, while our new data sample only the platform structure. Inversion of the two datasets, using the same starting model enables us to construct a shield model. Differences in shear velocity and density can thus be investigated.

4.1 Inversion for the west-European platform

In a preliminary inversion (Dost, 1986), using data obtained by an estimator that only takes into account the fact that all surface wave modes occur in one limited wavenumber band, we took a modified M7 model as the starting model. The M7 model does not exhibit sharp discontinuities near 400 and 670 km depth, since the higher mode dataset used in constructing this model could not distinguish between a sharp or smooth feature at those depths. The shear velocity under the Moho down to 220 km depth was set to a constant 4.45 km/sec and density to 3.40 gr/ccm. We restricted density variations in this depth interval to 0.2 gr/ccm in order to obtain realistic results. In the preferred model (WEPL1) the most remarkable features are a broadening of the low velocity zone and the disappearance of a Lehmann discontinuity. In addition a high shear velocity lid between 80 and 120 km was found to correlate with a density high. In the present inversion with a more refined dataset we will investigate the influence of the starting model on the inversion results. First the new dataset is inverted with the same smooth starting model as WEPL1, then we will investigate the influence of sharp discontinuities at varying depths on the inversion result. An overview of models used in this chapter is given in table 4.8.

Inversion with a smooth starting model

The result of our inversion using the modified M7 model as starting model (WEPL1a) is shown in figure 4.1.1. In the same figure WEPL1 is reproduced. Incorporation of travel times results in a more pronounced high shear velocity lid and low shear velocity layer. The Lehmann discontinuity at 220 km depth is absent in both models and average shear velocity between 350 and 650 km is in WEPL1a 0.1 km/s higher than WEPL1. Even if we assume the Lehmann discontinuity to be present in the starting model it is removed in the inversion procedure. Regarding the density it is remarkable that the density high at 100 km depth disappears completely and the density high around 200 km depth remains. The question rises whether this density feature is resolved or not. To answer this, resolution is calculated at specific depths and given in table 4.1 and 4.2. The standard deviation of the shear velocity v_s is comparable for both models. The standard deviation of the density shows a totally different behaviour. The WEPL1a model has a resolution far worse than WEPL1.

Table 4.1: v_s resolution

WEPL1a				WEPL1			
depth [km]	v_s [km/s]	st dev [km/s]	layer thickness [km]	depth [km]	v_s [km/s]	st dev [km/s]	layer thickness [km]
100	4.604	.110	80	100	4.393	.130	80
180	4.201	.072	80	180	4.188	.090	80
260	4.385	.110	80	270	4.411	.083	80
440	5.114	.090	120	440	4.954	.072	120

Table 4.2: ρ resolution

WEPL1a				WEPL1			
depth [km]	ρ [gr/ccm]	st dev [gr/ccm]	layer thickness [km]	depth [km]	ρ [gr/ccm]	st dev [gr/ccm]	layer thickness [km]
100	3.358	.160	80	100	3.424	.091	80
180	3.520	.220	80	180	3.180	.089	80
260	3.455	.190	80	270	3.148	.130	80
440	3.796	.260	120	440	3.684	.120	120

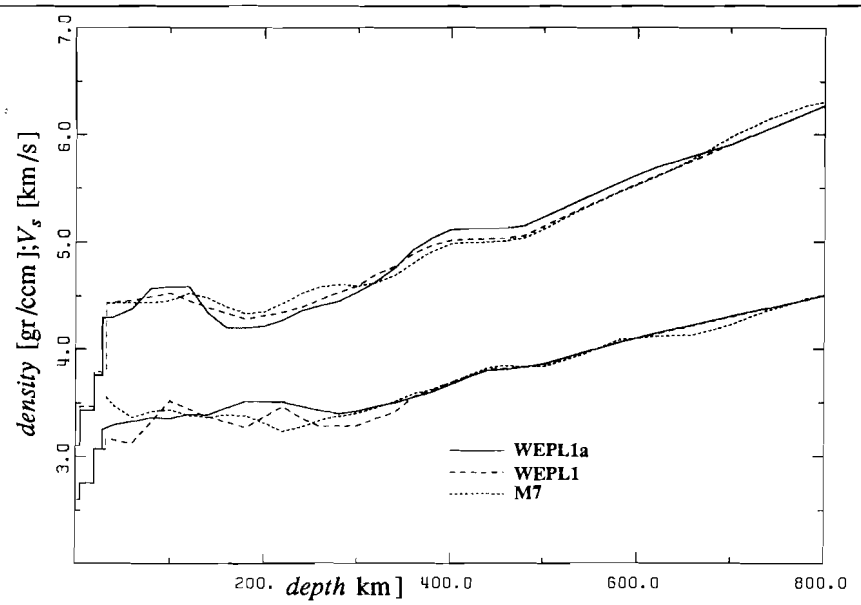

Figure 4.1.1. Density (lower curve) and shear velocity as a function of depth.

This means that a density high at approximately 200 km depth is not resolved and as a consequence ξ will not change when we smooth the density curve. Calculation of the model fit to the data for a model with a smooth density curve between 100 and 300 km depth and

WEPL1a, however, points towards the existence of the density high: ξ is reduced from a value of 1.69 to 1.38, which is significant. This disagreement between resolution calculations and the model fit to the data can be caused by the fact that the linearity assumption in the inversion is violated. Experiments show that the thickness of the high velocity lid determines the resolution in the density: a smaller lid thickness results in an improvement in resolution. It is interesting to note that Lerner-Lam (1985) reports that lid thickness can be substantially reduced by allowing a transverse isotropic parameterization of velocity in the inversion. In our present inversion this is not accounted for.
Finally, an experiment has been carried out to test the correlation between v_s and ρ at 100 km depth, as suggested by WEPL1. Therefore we coupled v_p, v_s and ρ by Poisson's ratio and Birch's law in the inversion. As a result the shear velocity exhibits again the high velocity lid, but density does not show a corresponding high as in WEPL1.
The model fit to the data shows in all cases a trade-off between the fundamental mode data from 90 to 160 s and higher mode data. Mode 5 can not be adequately fitted, the measured phase velocities are always too low. This bias can be due to interference effects with the 4^{th} and 6^{th} higher mode.

Inversion with a starting model containing sharp discontinuities

For a first inversion with a model containing sharp discontinuities we took the modified M7 model down to 360 km depth and added for depths ≥360 km the PREM model (Dziewonski and Anderson, 1981). In a first experiment the influence of a possible Lehmann discontinuity is investigated. Three starting models are used in the inversion: one with a smooth gradient between 200 and 300 km depth, one with a strong gradient between 220 and 240 km depth and one with a first order discontinuity at 220 km. Results are displayed in figure 4.1.2. All models, build with 9 eigenvectors, fit the data equally well (ξ =1.44, 1.44 and 1.42). These values are comparable with results from inversions with a smooth starting model. We can conclude that the existence of a Lehmann discontinuity is not resolved with our current data set. In general, the pronounced density high at 200 km depth, as present in inversions with a smooth starting model, disappears. An increase in density from 40 to 100 km depth is resolved for all models. For a starting model with a constant density from 40 to 300 km depth, the density gradient is always introduced and results in a significant improvement of the fit to the data. This agrees with our WEPL1 model, although the density gradient is smoother now. Variations in thickness of the high velocity lid do not affect resolution in density as was the case in the inversion with a smooth model. Models with a Lehmann discontinuity exhibit a thicker high velocity lid and a more pronounced low velocity layer. These models have a better fit to the traveltimes than less pronounced models and are thus preferred. The '400' km discontinuity starts for all models at higher shear velocity values than PREM. The model without a Lehmann discontinuity exhibits a jump in shear

velocity that is about 1.8 times larger (Δv_s= 0.3 km/s) than PREM (Δv_s= 0.17 km/s) and approximately 1.3 times larger than the two models containing a Lehmann discontinuity (Δv_s = 0.23 km/s). To our knowledge, the only published global or regional model with a comparable velocity contrast at the '400' km discontinuity is the EPR-B model for the mantle under the East-Pacific Rise (Wielandt and Knopoff, 1982). However, the depth of the discontinuity in this model is much larger (465 km). The average shear velocity of all three models between 400 and 600 km is significantly higher than PREM. Resolution of v_s and ρ is approximately the same as in WEPL1a , see table 4.3 and 4.4.

Table 4.3: v_s resolution
The second column (WEPL1.leh) gives values for a model with a strong gradient as Lehmann discontinuity.

WEPL1a				WEPL1.leh			
depth [km]	v_s [km/s]	st dev [km/s]	layer thickness [km]	depth [km]	v_s [km/s]	st dev [km/s]	layer thickness [km]
100	4.604	.110	80	100	4.605	.090	80
180	4.201	.072	80	180	4.128	.068	80
260	4.385	.110	80	260	4.494	.110	80
340	4.762	.083	80	340	4.717	.078	80
440	4.954	.072	120	440	5.158	.089	120

Table 4.4: ρ resolution
The second column (WEPL1.leh) gives values for a model with a strong gradient as Lehmann discontinuity.

WEPL1a				WEPL1.leh			
depth [km]	ρ [gr/ccm]	st dev [gr/ccm]	layer thickness [km]	depth [km]	ρ [gr/ccm]	st dev [gr/ccm]	layer thickness [km]
100	3.358	.160	80	100	3.415	.170	80
180	3.520	.220	80	180	3.475	.200	80
260	3.455	.190	80	270	3.454	.210	80
340	3.555	.210	80	340	3.509	.200	80
440	3.796	.260	120	440	3.762	.220	120

The disappearance of the density anomaly at 200 km depth and the disappearance of the dependence of density resolution on lid thickness stress the importance of the existence of discontinuities in the starting model. No explicit assumptions about anisotropy or a density high at 200 km depth are needed to obtain an acceptable model. The departure from smooth models in the linearized inversion may introduce non-linear effects. The presented resolution calculations should therefore be interpretated as a rough order of magnitude calculation. In conclusion we can say that, although the Lehmann discontinuity is not resolved, a smooth gradient between 200 and 400 km depth leads to a large jump in shear velocity at the '400'

km discontinuity compared to a reference earth model like PREM and more regional models.

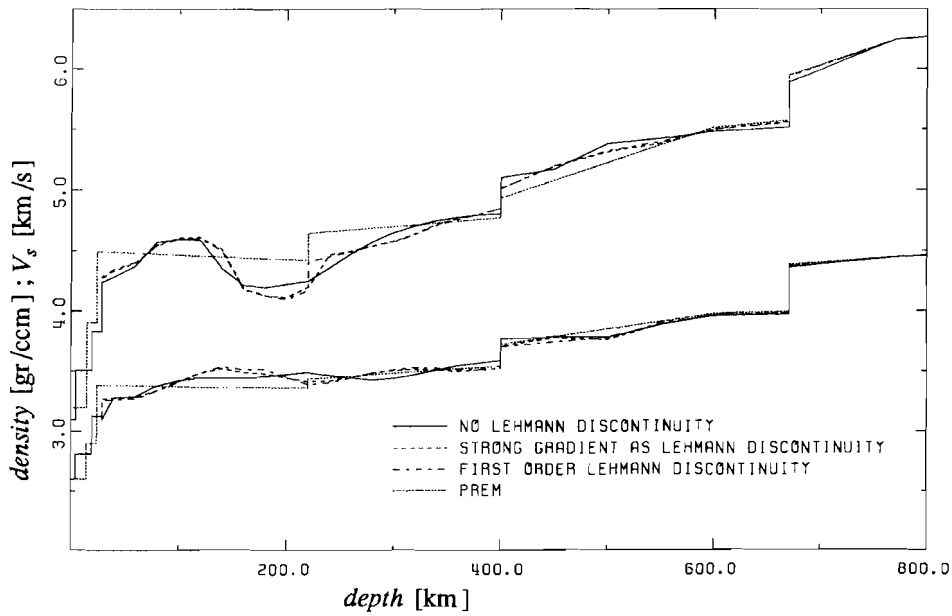

Figure 4.1.2. Density (lower curve) and shear velocity as a function of depth for a starting model with discontinuities at 400 and 650 km depth. Inversion results for three different starting models are compared with PREM.

Now we can investigate the influence of the depth of the two major discontinuities in the inversion. The depth of the 400 km discontinuity is best determined by body-wave studies and ranges from 380 to 420 km depth. In general the sharpness of this discontinuity is not well determined, except in the case of northern Australia where a first order discontinuity at 406 km has been found (Leven, 1985). We investigate three models with a first order discontinuity at 380, 400 and 420 km depth respectively as well as a model with a strong gradient between 380 and 420 km depth. Results for the first three models are displayed in figure 4.1.3. The discontinuity located at 380 km depth has the effect that the Lehmann discontinuity disappears and that the jump in v_s at the discontinuity becomes much larger (.28 km/s) than in PREM. The other two models are very similar to each other, except in the immediate vicinity of the discontinuity itself. The jump in shear velocity at the discontinuity is in both models approximately .22 km/s. This value is comparable with existing regional models like SNA and TNA (Grand and Helmberger, 1984). The gradients in shear velocity between the '400' km discontinuity and 600 km depth are approximately equal for

the three models. There is no resolved difference in density gradient for the three models. Experiments in the form of an inversion with a strong gradient in shear velocity and density between 380 and 420 km depth gave similar results as the models with a discontinuity at 400 and 420 km depth. This observation shows again the inability of the surface wave data to discriminate between a strong gradient and a first order discontinuity. The influence of the location of the 650 km discontinuity on more superficial gradients in shear velocity or density of the model is negligible.

There is a difference in width of the high velocity lid and absolute depth of the low velocity layer between inversion results in figure 4.1.2 and 4.1.3. As stated before it was found that models with a greater thickness of the high velocity lid and more pronounced low velocity layer give the best fit to the traveltime data and are thus to be preferred. The use of models with a more pronounced velocity contrast and thicker high velocity lid in stead of the models shown in figure 4.1.3. has no influence on our present conclusions.

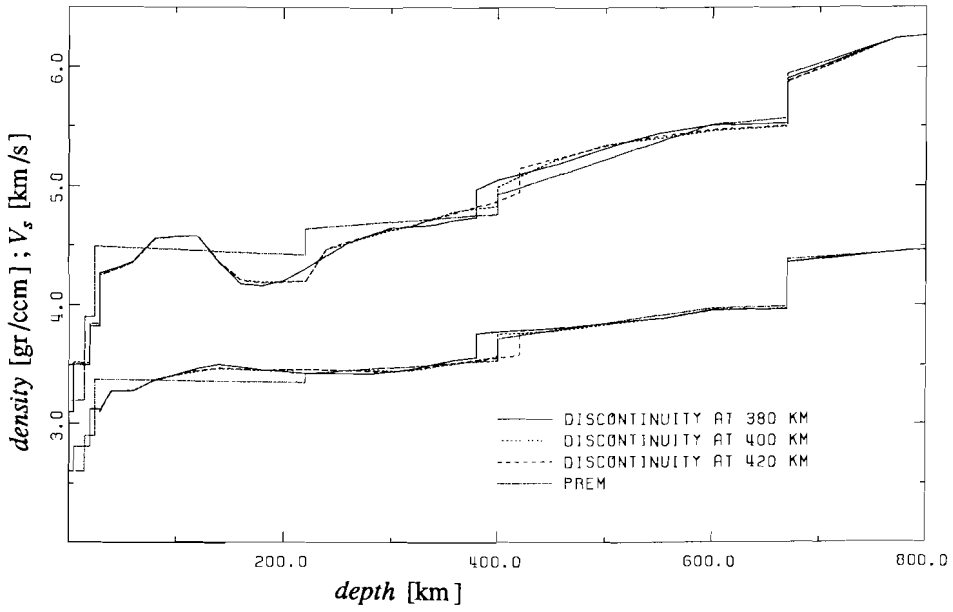

Figure 4.1.3. Density (lower curve) and shear velocity as a function of depth for a starting model with the '400 km' discontinuity at 380, 400 and 420 km depth. Inversion results for three different starting models are compared with PREM.

For a definite choice of an average platform model we include constraints from body wave studies. Paulssen (1987 and pers. comm.) studied P and S waveforms from European events using NARS recordings and WKBJ modelling. She found that waveforms from different

source-receiver paths could not be fitted with one homogeneous model down to a depth of at least 450 km and only bounds on the depth of the '400' km discontinuity can be roughly specified. A minimum depth of the '400' km discontinuity of 400-420 km is constrained from this modelling.

Our final model for the west-European platform (WEPL2) thus consists of a high shear velocity lid from 80 to 140 km depth, a pronounced low velocity channel from 140 to 240 km depth and a smooth gradient in velocity between 240 and 400 km depth. The two major discontinuities are placed at 400 and 650 km depth. Density shows a steep gradient between 60 and 140 km depth, followed by an approximately constant value down to 300 km depth. At greater depth density follows PREM closely. This model is shown in figure 4.1.4 and listed in table 4.5. Resolution is indicated in table 4.6. In all inversions presented in this chapter there is a trade-off between the misfit of fundamental mode data at 90 to 160 s and higher mode data as noted already in the inversion with a smooth starting model. A period of 90 s for the fundamental mode means a penetration depth of approximately 180 km, the deepest part of the low velocity zone. The region that is of major importance in this incompatibility between fundamental and higher modes is thus the region around the possible Lehmann discontinuity which is badly resolved in the inversion. The bias of the 5^{th} mode remains also present.

Table 4.5: WEPL2

depth [km]	v_s [km/s]	ρ [gr/ccm]	depth [km]	v_s [km/s]	ρ [gr/ccm]
0-5	3.100	2.600	320	4.647	3.453
5-20	3.509	2.815	340	4.736	3.473
20-29	3.829	3.128	360	4.783	3.487
29	4.263	3.271	380	4.830	3.527
40	4.323	3.281	400	4.876	3.564
60	4.382	3.283	400	5.096	3.745
80	4.543	3.351	450	5.202	3.773
100	4.622	3.428	500	5.282	3.774
120	4.622	3.487	550	5.384	3.886
140	4.520	3.516	600	5.502	3.964
160	4.178	3.466	635	5.529	3.965
180	4.117	3.435	670	5.556	3.966
200	4.130	3.444	670	5.940	4.345
220	4.244	3.453	721	6.087	4.399
240	4.414	3.455	771	6.241	4.443
260	4.453	3.477	871	6.311	4.504
280	4.505	3.499	971	6.378	4.563
300	4.557	3.484			

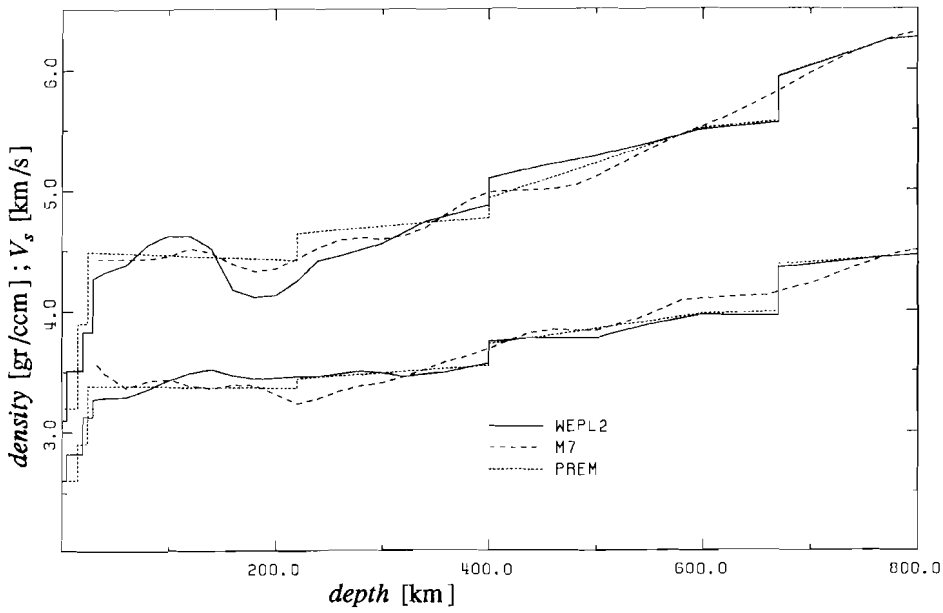

Figure 4.1.4. Density (lower curve) and shear velocity as a function of depth for WEPL2. For comparison M7 and PREM are shown.

Table 4.6: resolution WEPL2

depth [km]	v_s [km/s]	st dev [km/s]	layer thickness [km]	depth [km]	ρ [gr/ccm]	st dev [gr/ccm]	layer thickness [km]
40	4.323	.076	40	40	3.281	.170	40
100	4.625	.091	80	100	3.428	.170	80
180	4.117	.056	80	180	3.435	.210	80
260	4.453	.110	80	260	3.477	.210	80
340	4.736	.078	80	340	3.473	.220	80
440	5.181	.092	120	440	3.767	.240	120

4.2 Inversion for the Scandinavian shield

We can compare our new dataset sampling the west-European platform with Nolet's dataset for western Europe including Scandinavia in order to detect differences in structure between the two regions. Although our measurements have been obtained for much higher frequencies, this comparison can give information on gross differences. Therefore we compared smooth models inverted with only a limited amount of eigenvectors. Nolet's phase

velocity data were re-inverted using the same starting model as in the WEPL2 inversion. A smooth model could be obtained with 7 eigenvectors and shows basically the same features as M7. A minimum in density around 220 km depth is retained. The new data were re-inverted to obtain a smooth 7 eigenvector model for comparison. Traveltimes have been excluded. The shield model has been calculated by means of the expression:

$$\vec{m}_s \Delta_s = (\Delta_p + \Delta_s)\vec{m}_{s+p} - \Delta_p \vec{m}_p \tag{4.1}$$

where Δ_s and Δ_p stand for the path length over the shield and the platform structure respectively and $\vec{m}_s$, $\vec{m}_p$ and $\vec{m}_{s+p}$ denote shield, platform and averaged model values. The resulting model is called SCSH2 and is tabulated in table 4.7. The same procedure has been applied to the preliminary dataset by Dost (1986), and resulted in a difference model SCSH1. A comparison between SCSH1, SCSH2 and WEPL2 is shown in figure 4.1.5. A constant shear velocity value down to 300 km depth that was found in SCSH1, is still present in SCSH2. The latter model shows more fluctuations between 220 and 300 km depth, but this can be attributed to the region where resolution becomes bad in WEPL2 and the possible existence of a Lehmann discontinuity is not resolved. This observation that the low velocity channel is absent under the Scandinavian shield is also supported by findings of Calcagnile (1982) from regionalisation of fundamental mode Rayleigh wave phase velocities. Between 400 and 500 km depth a difference in shear velocity between WEPL2 and both SCSH1 and SCSH2 is observed. Concerning the density, a difference between 200 and 320 km depth is observed. This density difference is on average 0.20 gr/ccm. As we noted before resolution calculations can only be used as a rough estimate. In these model difference calculations this becomes even more troublesome. However, since the density difference is spread out over at least 120 km depth and the estimated resolution for WEPL2 at 260 km is 0.21 gr/ccm over 80 km depth, it is acceptable to conclude that there is a strong indication for a difference in density between the Scandinavian shield and the west-European platform between 200 and 350 km depth. The interpretation of the models presented in this chapter in terms of mineralogy is the topic of the next chapter.

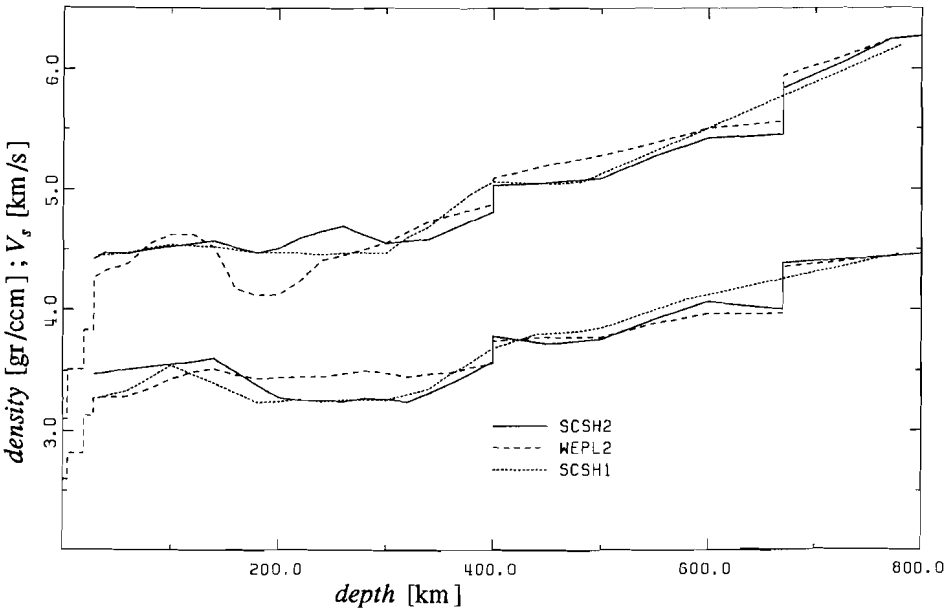

Figure 4.1.5. Density (lower curve) and shear velocity as a function of depth for SCSH2. For comparison SCSH1 and WEPL2 are shown.

Table 4.7: SCSH2

depth [km]	v_s [km/s]	ρ [gr/ccm]	depth [km]	v_s [km/s]	ρ [gr/ccm]
29	4.423	3.469	340	4.589	3.317
40	4.473	3.483	360	4.664	3.392
60	4.466	3.509	380	4.739	3.483
80	4.496	3.529	400	4.814	3.575
100	4.525	3.549	400	5.034	3.787
120	4.546	3.574	450	5.057	3.718
140	4.567	3.601	500	5.093	3.755
160	4.520	3.492	550	5.277	3.921
180	4.475	3.382	600	5.421	4.065
200	4.511	3.281	635	5.437	4.031
220	4.597	3.259	670	5.451	3.998
240	4.650	3.253	670	5.836	4.387
260	4.692	3.246	721	6.035	4.415
280	4.623	3.272	771	6.241	4.443
300	4.553	3.266	871	6.311	4.504
320	4.571	3.246			

Table 4.8 Overview of models mentioned in the text.

model	data used	# eigenvectors	remarks
M7	Fundamental (6-35 mHz) and higher mode (mode 1-6;10-35 mHz) Rayleigh wave phase velocities for western Europe and Scandinavia (Nolet, 1977).	?	Separate inversion for shear velocity and density.
WEPL1	Fundamental (6-50 mHz) and higher mode (mode 1-6;30-70mHz) Rayleigh wave phase velocities for the west-European platform (Dost, 1986).	10	Simultaneous inversion for shear velocity and density
WEPL2	Fundamental (6-50 mHz) and higher mode (mode 1-6;22-70mHz) Rayleigh wave phase velocities for the west-European platform. In addition a shear wave traveltime dataset is compiled. Discontinuities are introduced in the starting model (This study).	9	Simultaneous inversion for shear velocity, density and shear wave traveltime data.
SCSH1	Constructed as a difference model from an inversion of the dataset used in WEPL1 and the M7 dataset using identical starting models (Dost, 1986).	8	see WEPL1
SCSH2	Same as in SCSH1, only WEPL1 is replaced by WEPL2 and traveltimes are excluded (This study).	7	see WEPL2
WEPL1a	Inversion of the dataset of WEPL2 with a smooth starting model (This study).	10	none

5. INTERPRETATION AND CONCLUSIONS

For an interpretation of the models derived in the last chapter in terms of mantle mineralogy we need information about elasticity parameters and their pressure and temperature derivatives. Recent progress in the measurement of these parameters in high pressure laboratories now make it possible to test hypotheses about the upper mantle structure. These hypotheses are mainly based on arguments related to the average mineralogy (pyrolite and piclogite models), but may include arguments concerning mechanical properties (tectosphere model or lithospheric doubling concept). We will give a brief review of the major hypotheses, compare our shear velocity and density models with models constructed from recently published laboratory data and discuss the implications for the west-European platform and Scandinavian shield structure. An interpretation of preliminary results (WEPL1 and SCSH1; Dost, 1986) in terms of mineralogy was published in Nolet et al. (1986b).

5.1 Mineralogical models

Table 5.1 gives an overview of the principal minerals in the upper mantle. Indicated are abbreviations that will be used in the text.

Pyrolite

Ringwood (1975, 1979, 1982) proposes a model for the upper mantle that is based on a homogeneous undepleted mantle mineral assembly: pyrolite. Its composition, as used in different tests mentioned in this chapter, is shown in table 3.2. Pyrolite acts as the primitive source material of modern basalts, that are formed upon partial melting. Different basalt types are the result of a difference in the percentage of partial melting (this percentage is for nephelinites 1-5%, alkali basalts 5-10%, tholeiites 15-25% and komatiites 30-60%). The remaining fractions after partial melting are garnet and spinel lherzolite, complementary to nephelinites and alkali basalts, harzburgite, complementary to tholeiites and dunite, complementary to komatiites. The discontinuities at 400 and 650 km depth are interpreted as phase changes. The '400' km discontinuity is interpreted as the transition from olivine to modified spinel (β-phase) accompanied by a increasing solid solution of pyroxene in garnet. The transition zone, the region between 400 and 650 km depth, is mainly consistent with a modified spinel plus garnet composition with minor clinopyroxene. The latter phase exists down to 500 km depth. At 550 km depth the modified spinel transforms to spinel (γ-phase) and this breaks down to perovskite and periclase between 650 and 700 km depth. Garnet breaks down to the ilmenite structure starting at 600 km depth. A subducting slab, mainly consisting of a basaltic upper layer underlain by a harzburgite layer, sinks to approximately 600 km depth and remains denser than the surrounding mantle. Below 650

km depth the former basaltic layer remains denser, but the harzburgite layer becomes relatively buoyant and material gathers at the 650 km discontinuity. This material is heated by thermal conduction and the former basaltic crust is subjected to partial melting. As a result the former harzburgite is fertilized, becomes buoyant and starts forming diapirs into the upper mantle. The residual former basaltic layer sinks as large blocks into the lower mantle in a dense perovskite structure.

Piclogite

Anderson (1979a), Bass and Anderson (1984) and Anderson and Bass (1984, 1986) discuss the piclogite model in detail. A general discussion is also presented by Oxburgh (1980). The piclogite model is based on a chemically inhomogeneous mantle composition. It is assumed that an original melt layer or magma ocean was present. Then the scenario is envisaged where low density olivine crystallizes and becomes concentrated in the shallow mantle in peridotite. Garnet crystallizes later and sinks, while the residual fluid freezes to a clinopyroxene-garnet rich mixture with some olivine. This residu is called piclogite (or an olivine eclogite) and is in composition close to komatiite. Pyroxene dissolves with increasing depth in the garnet and at the end of the transition zone (550-650 km) garnetite is formed. Eclogite will accumulate at the 650 km discontinuity, as it cannot penetrate it because of the high density of Al_2O_3- poor assemblages beneath the discontinuity. In this way a stratification of the upper mantle is achieved. From top to bottom the upper mantle thus consists of: basalt, peridotite and eclogite. Basalt injected into the mantle during subduction inverts at shallow depths to eclogite and sinks rapidly through the mantle. Anderson (1979a,b) interpretes the 220 km discontinuity as the boundary between the peridotite and eclogite layer and the 400 km discontinuity as the boundary between eclogite and garnetite. More recently Liu (1980) and Bina and Wood (1984) have argued that the eclogite to garnetite transition would not produce the observed 400 km discontinuity. As a result Anderson and Bass (1984, 1986) and Bass and Anderson (1984) moved the boundary between peridotite and eclogite down from 220 km to 400 km depth. Most remarkable is the difference in piclogite composition between the Bass and Anderson (1984) and Anderson and Bass (1984) paper (see table 5.1). A comparison between compositions used by different authors is complicated by the use of both weight and volume percentages by these authors.

Table 5.1 Principal minerals in the upper mantle.		
Olivine (Ol) (β= modified spinel, γ=spinel)		$[Mg,Fe]_2SiO_4$
Orthopyroxene (Opx)		$(Mg,Fe)SiO_3$
Clinopyroxene (Cpx)		$(Mg,Fe)CaSi_2O_6$
Pyrope-garnet (Pgt)		$(Mg,Fe)_3Al_2Si_3O_{12}$
Garnet-majorite (Mgt)		$[(Mg,Fe)_3Al_2Si_3O_{12}]_{1-y}.[(Mg,Fe)_4Si_4O_{12}]_y$
Perovskite (Pv)		$(Mg,Fe)SiO_3$
Ilmenite (Il)		$(Mg,Fe)SiO_3$
Periclase (Pc)		$(Mg,Fe)O$
Jadeite (Jd), commonly in solid solution with Cpx		$NaAlSi_2O_6$
Grossularite (Grs), commonly in solid solution with Pgt		$Ca_3Al_2Si_3O_{12}$
Garnet lherzolite		Pgt+Opx+Cpx+Ol
Spinel lherzolite	**Peridotite**	Sp+Opx+Cpx+Ol
Harzburgite		Ol+Opx
Dunite		Ol
Eclogite		Gt+Cpx

Table 5.2 Comparison of models used in hypothesis testing.

	Pyrolite			Piclogite		
Comp.	Bass & And. [wt %]	And. & Bass [wt %]	Weidner [vol %]	Bass & And. [wt %]	And. & Bass [wt %]	Weidner [vol %]
Ol	57	57	61	16	16	16
Opx	17	17	15	3	6	3
Cpx	12	12	10	44	33	45
Gt	14	14	14	37	45	36

Hypothesis testing

In a recent series of articles, partly reviewed by Anderson and Bass (1986), the pyrolite and piclogite models are tested against global seismological results (the PREM model of Dziewonski and Anderson, 1981). As a data base an internally consistent dataset of laboratory measurements on a pyrolite composition by Akaogi and Akimoto (1977, 1979) is widely used. A review by Jeanloz and Thompson (1983) gives valuable information on existing data and uncertainties. The only laboratory measurements on a piclogitic composition is made by Irifune et al. (1986). They studied an alkaline-poor olivine tholeiite.

Acoustic velocities are calculated at depth by projection along adiabats. This assumption of adiabaticity is thought to be reasonable for the deeper part of the upper mantle. In terms of thermodynamics the mineral assemblage is heated isobarically up to the so called 'foot' to

the adiabat temperature. From there it is adiabatically compressed to the desired pressure (Weidner, 1986).
Bass and Anderson (1984) and Anderson and Bass (1984) compared in this way a pyrolite and piclogite composition. As reference model the PREM model has been used. They concluded that both the pyrolite and piclogite models are acceptable down to the 400 km discontinuity, but that for the transition region between 400 and 650 km depth the pyrolite model generates too high shear velocity values, while piclogite is appropriate. Anderson and Bass (1984) show that for shields the velocities fall near the $1400^{o}C$ adiabat for depths greater than 200 km. Other models, e.g. tectonic rise, approach this adiabat at much larger depths (near 400 km). In answer to their study Weidner (1985; 1986) comes to the opposite conclusion, namely that the pyrolite model is acceptable, and points out that this inconsistency is due to different assumptions concerning phase equilibria for the pyroxene-garnet transformation, elastic properties of the majorite phase and pressure and temperature derivatives of the elastic properties of the high pressure phases. In his study a $1400^{o}C$ foot to the adiabat has been used as well. Irifune et al. (1986) conclude that, based on measured properties of a piclogite like composition, the piclogite model can not explain the velocity jump at 400 km depth and the high gradient in the transition zone.
The most important parameters that lead to the present controversy are the jump in shear velocity at the 400 km discontinuity, the velocity gradient in the transition region (400-650 km depth) and the absolute level of velocity between 300 and 400 km depth. In the following we will describe these in detail.

Absolute velocity 300-400 km depth

In this region all calculated models give more or less the same results. Here the assumption of the $1400^{o}C$ foot to the adiabat is only valid for shields.

400 km discontinuity

Bass and Anderson (1984) assume in their model that at 400 km depth all olivine is transformed to modified spinel (β phase) and that all orthopyroxene is already dissolved in garnet as majorite. Their pyrolite model therefore creates a jump in velocity that is twice the observed value and only piclogite, containing less olivine, is able to produce the correct velocity jump due to the additional pyroxene to garnet transition. Bina and Wood (1984) demonstrate, both on experimental and thermodynamical grounds, that the eclogite-garnetite transition does not exhibit any discontinuity in bulk sound velocity from 11 to 23 GPa.

Weidner (1985) argues that the magnitude of the 400 km discontinuity is not only sensitive to the amount of olivine present in the mantle, but also to the pressure derivative of the shear modulus of the high pressure phase that is not yet measured. The observed velocity and density jump is found to be consistent with an olivine content of 40-65 volume %. For models with a smaller olivine content an accompanying chemical discontinuity should be present. The contradiction with findings by Lees et al. (1983) are attributed to incorrect elastic parameters for spinel and modified spinel and differences with Bass and Anderson (1984) to phase relations and properties of the garnet phase. In a more elaborate paper on the subject Weidner (1986) argues that there are observations that are incompatible with Bass and Anderson's conclusions. One critical assumption that comes under attack is the assumption that Ca-poor pyroxene dissolves completely into the garnet phase around 400 km depth. The only possibility for a complete dissolution of Ca-poor pyroxene is in case Akaogi and Akimoto (1977; 1979) overestimated their pressure. Irifune et al. (1986) report that this is the case. A direct cause of the overestimation of pressure is that there should be a considerable solution of pyroxenes into garnets at depths as shallow as 200 km. The recent discovery by Moore and Gurney (1985) of pyroxenes in solid solution with garnets as inclusions in diamonds from kimberlites supports these conclusions.
Observations that can not be explained are coexisting garnet, modified spinel and Ca-poor pyroxenes at a pressure of 145 kb and spinel with Ca-poor pyroxene at 205 kb (Akaogi and Akimoto, 1979).
The experiments carried out by Irifune et al. (1986) on a piclogitic composition lead to the conclusion that not only the Ca-poor-pyroxene dissolves completely into the garnet phase at 400 km depth, but also the clinopyroxene. This gives us a pyroxene free garnetite composition at the 400 km discontinuity, which results in a too large jump in velocity and density for Anderson and Bass's eclogitic and piclogitic compositions.

Transition region 400-650 km

Anderson and Bass (1986) assume that this region is dominated by a clinopyroxene-garnet composition. At 550 km depth, 60% of the clinopyroxene is dissolved in the garnet phase as majorite and coexists with spinel and orthopyroxeen-majorite. At the bottom of the transition layer all pyroxene is present as majorite. They claim that only this composition, with clinopyroxene gradually changing to majorite can explain the low velocities and high gradients in the transition region. Weidner (1985, 1986) demonstrates that his pyrolite model does account for the observed high gradient and concludes that the pyroxene to garnet and excess Ca-poor-pyroxene to spinel plus stishovite transformations give the main

boundaries between modified spinel and spinel remain linear, but that the above mentioned interpretation of the 550 km discontinuity has to be rejected. The same author proposes a phase transition of pyroxene to a garnet-like structure.

5.2 Models involving mechanical properties

The models described in the last section are based on an average Earth structure without lateral variations. In this chapter we will discuss two models that do account for differences between geological provinces.

Tectosphere model

Jordan (1975, 1978, 1981) tackled the problem of the contrast in upper mantle properties between old continents and old oceans. Application of the thermal-boundary layer model (as developed in plate tectonic theory) to continents preclude the existence of differences in chemical, mechanical or thermal properties beneath 100-150 km depth. However, from seismological observations of ScS and multiple ScS travel times (Sipkin and Jordan, 1975, 1976, 1980) this was questioned and the tectosphere model presented as an alternative. In the tectosphere model a thick 'root' or chemical boundary layer is present that stabilizes a more than 200 km thick thermal boundary layer against convective disruptions. The root consists mainly of peridotite, depleted in basaltic components. Depletion can be caused by 10-20% partial melting. The melt phase migrates upward and as a result the root becomes less dense. This effect will not only compensate for the temperature, but also stabilize against convection. This hypothesis has been rejected by e.g. Anderson (1979b), because of a lack of convincing seismological evidence that continents and oceans differ in structure beneath 200 km depth.

Lithospheric doubling

Lithospheric doubling is defined by Vlaar (1982, 1983) as horizontal subduction of young (<30 Ma) oceanic lithosphere, obducted by a continental or oceanic lithosphere. It is proposed to be a general phenomenon in recent plate tectonics and was shown to provide a succesful scenario for the Alpine orogeny (Vlaar and Cloetingh, 1984). Lithospheric doubling would imply a strongly stratified upper mantle up to a few hundreds of kilometers depth. Density should increase in the top of the lithosphere, but may be followed by a density drop where the second harzburgite layer is present. This is an unstable situation, but may 'freeze' in (Nolet et al, 1986b).

Hypothesis testing

Both the tectosphere and lithospheric doubling concept can be used for interpretation of the upper part of our models (z < 400 km). The tectosphere concept needs information about the depth at which there are no differences in mantle structure between different geological provinces, in our case the Scandinavian shield (SCSH1,2) and west-European platform (WEPL1,2). Lithospheric doubling looks for a strongly layered upper mantle and specifically an eclogitic layer that might mark the top of an obducted young ocean. Both models are not in conflict with each other like the pyrolite and piclogite models.

5.3 Petrological Interpretation

The assumptions in the hypothesis testing of the pyrolite and piclogite model, that acoustic velocities can be projected to greater depths along adiabats is not valid for the upper 200-400 km. Therefore Nolet et al. (1986b) parameterized a geotherm for this region and relied on laboratory measurements of seismic velocities at room temperature and pressure and their isothermal and isobaric derivatives with respect to pressure and temperature. By projection along the adopted geotherm they were able to construct velocity curves for the most important mantle minerals. Although the laboratory measurements of the derivatives with respect to pressure and density are not very accurate, especially concerning the derivatives with respect to pressure and density, an important conclusion was reached: temperature and pressure effects cannot by itself cause high gradients in v_s and ρ. As a consequence we must interprete large velocity or density gradients in terms of a change in mineralogy, chemical composition or partial melting. In figure 5.1.1. the upper 450 km of the WEPL1 and WEPL2 models are compared.
The shear velocity contrast between the high velocity lid and the low velocity zone is enlarged in WEPL2 with respect to WEPL1. The high velocity lid in WEPL2 is confined to the depth range from 80-140 km. The corresponding density gradient indicates an increase in density. The average density in the 80-140 km depth interval amounts to 3.45 gr/ccm and can only be explained with the existence of garnet, since olivine, orthopyroxene and clinopyroxene give density values of approximately 3.3 gr/ccm in this depth region (Nolet et al., 1986b). This means that the interpretation of this high velocity/high density region as an eclogitic layer, as advocated by Nolet (1977) remains the most plausible one. No density inversion, as observed by Nolet (1977), is resolved at greater depth.
The eclogitic layer near 100 km depth can only be explained by the lithospheric doubling concept: The basalt of the obducted ocean lithosphere is transformed to eclogite. A density inversion that marks the underlying harzburgite layer may not be resolved.
The velocities in the low velocity zone are such that they do not coincide with any major mineralogy and partial melting is assumed. Since a possible Lehmann discontinuity is not

resolved, the gradient between 200 and 400 km depth is not very well determined. It can be observed however that both models, WEPL1 and WEPL2, exhibit the same gradient from 250 to 350 km depth.

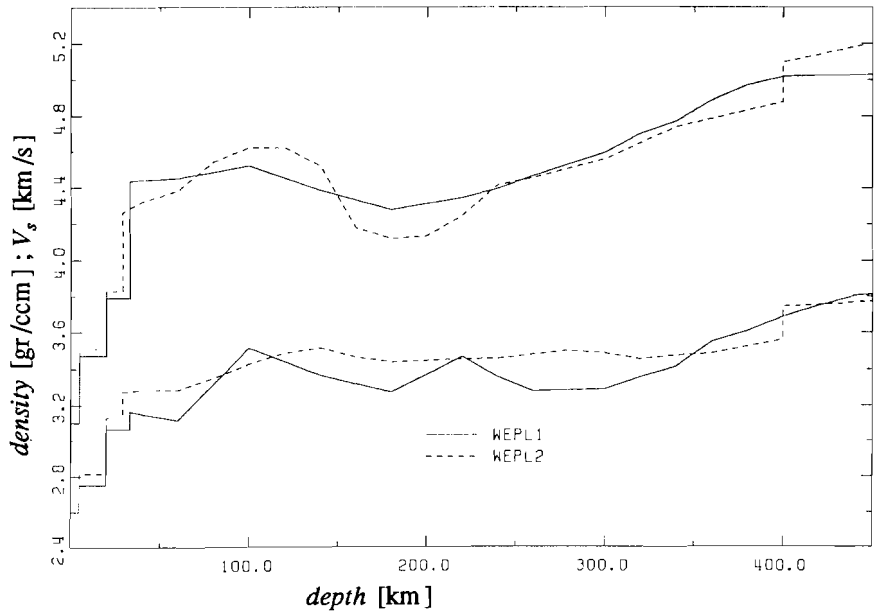

Figure 5.1.1. Density (lower curve) and shear velocity as a function of depth for WEPL1 and WEPL2.

The deeper part of the model can be compared with shear velocity and density models for a pyrolite and piclogite composition by Bass and Anderson (BA ,1984) and Weidner (WE, 1985). This is shown in figures 5.1.2 and 5.1.3. Concerning the shear velocity, it is obvious that the uppermost 350 km can not be fitted by any of these two models, which confirms our previous conclusions. At 400 km depth the jump in velocity agrees well with BA-piclogite and WE-pyrolite. A total disagreement exists with BA-pyrolite. The change in gradient between 500 and 600 km depth is compatible with WE-pyrolite, only at greater depth. This feature is not well resolved, but we are unable to maintain a gradient as in the BA- models in our inversion. Density is not well resolved below 150 km, but we can observe some features. The jump in density at 400 km depth is most likely to be larger than predicted by the BA-piclogite model. Inversions with a density difference smaller than WEPL2 generate a sharp density inversion after the 400 km discontinuity and this is thought to be unrealistic. At greater depths all models coincide with respect to density.

Finally, we can compare our model for the scandinavian shield (SCSH2) with WEPL2. Both

models are displayed in figure 4.1.5, together with SCSH1. SCSH1 and SCSH2 are very similar, except in the vicinity of a discontinuity and around 250 km depth where uncertainty exists related to the possible Lehmann discontinuity.

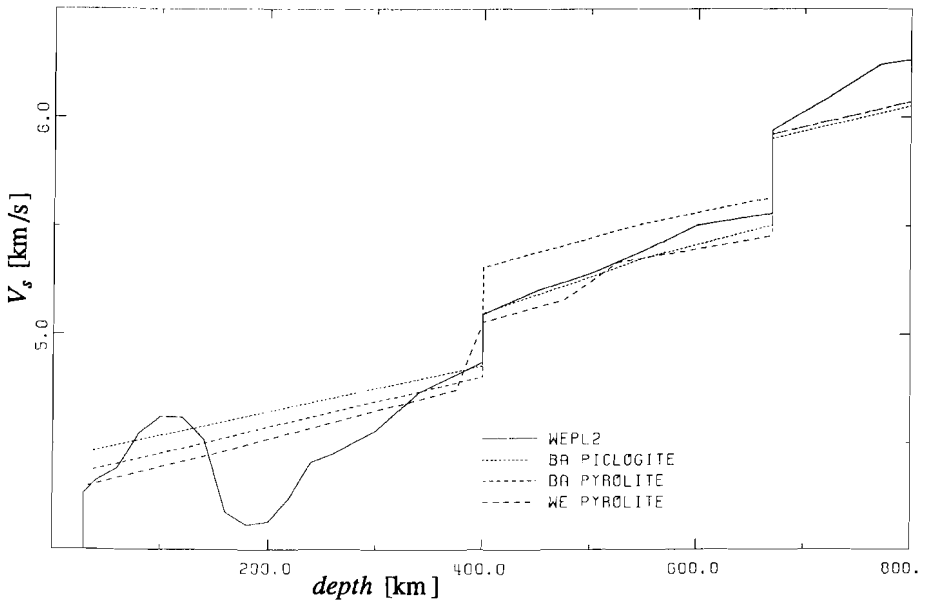

Figure 5.1.2. Shear velocity as a function of depth for WEPL2, Bass and Anderson (BA) piclogite and pyrolite and Weidner (WE) pyrolite.

A general and well resolved difference between SCSH1,2 and WEPL2 is the low velocity layer at 160-220 km depth. This supports the tectosphere hypothesis that there are significant differences between shield and platform structure at least up to 250 km depth. The shield is much cooler, no partial melting seems to occur. In the upper part of the transition zone shear velocity seems to be lower under the shield region, thus suggesting that there are differences in structure between shield and platform down to 500 km depth. This observation can also explain why PREM, as a average global model, exhibits systematically lower shear velocity values than our present inversion results. A difference in depth of the 400 km discontinuity does not influence the shear velocity gradients in the transition zone, as shown in chapter 4.

Regarding density we can only conclude that a possible density inversion exists under the Scandinavian shield between 200 and 350 km depth. This would also be in favour of the tectosphere model: the 'root' is depleted in basaltic components and therefore less dense.

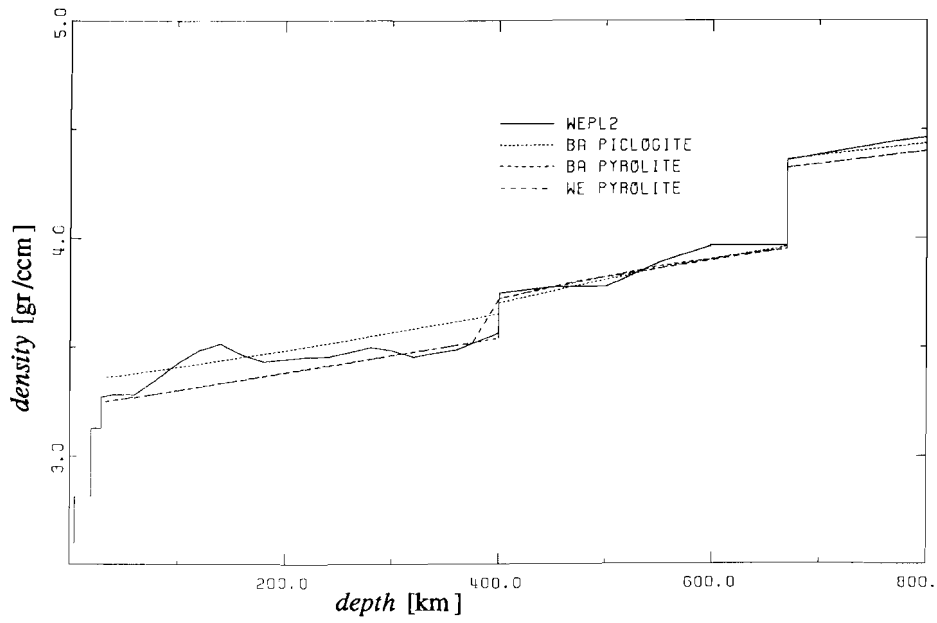

Figure 5.1.3. Density as a function of depth for WEPL2, Bass and Anderson (BA) piclogite and pyrolite and Weidner (WE) pyrolite.

5.4 Conclusions

The interpretation of shear velocity and density models, obtained by inversion of fundamental and higher mode Rayleigh wave phase velocities, has enabled us to investigate the structure and composition of the west-European platform. The most remarkable result is the existence of a layer of high velocity and high density, which is interpreted as an eclogite layer, at approximately 100 km depth. It is followed by a pronounced low velocity layer, which indicates partial melting. The transition zone is characterized by high shear velocities and a change in shear velocity gradient at approximately 600 km depth. An interpretation in terms of a pyrolite or piclogite structure is not possible, because of the uncertainties in elasticity parameters of the high pressure phases. However, the jump in density at the 400 km discontinuity favours a pyrolite composition. The existence of an eclogite layer supports the lithospheric doubling theory.

In the inversion procedure it became apparent that the existence of discontinuities in the starting model is of crucial importance for the inversion result. Introduction of these discontinuities, however, can lead to non-linear effects and as a result the linearized

inversion procedure is not valid any more. Therefore it is recommended to use the models produced in this study in a non-linear inversion procedure and test their validity as average models. A comparison with results from body wave modelling by Paulssen (pers. comm.) shows similarities, not only in the upper part of the model, but also regarding the high shear velocity values in the transition zone.

The model for the Scandinavian shield is less reliable, because we compare a low frequency dataset for shield plus platform with a high frequency dataset for the platform only. As a result we can only look at gross differences. A major feature like the low velocity zone is clearly not present under the shield structure, while density seems to be lower under the shield from 200 to 350 km depth. In the transition layer there is evidence for a difference in shear velocity between shield and platform, suggesting a difference in structure between shield and platform down to 500 km depth. This observation is consistent with the tectosphere hypothesis.

APPENDIX A:
The transfer function of a second order filter

In this appendix the general form of a second order transfer function used in equation (1.3) is derived.

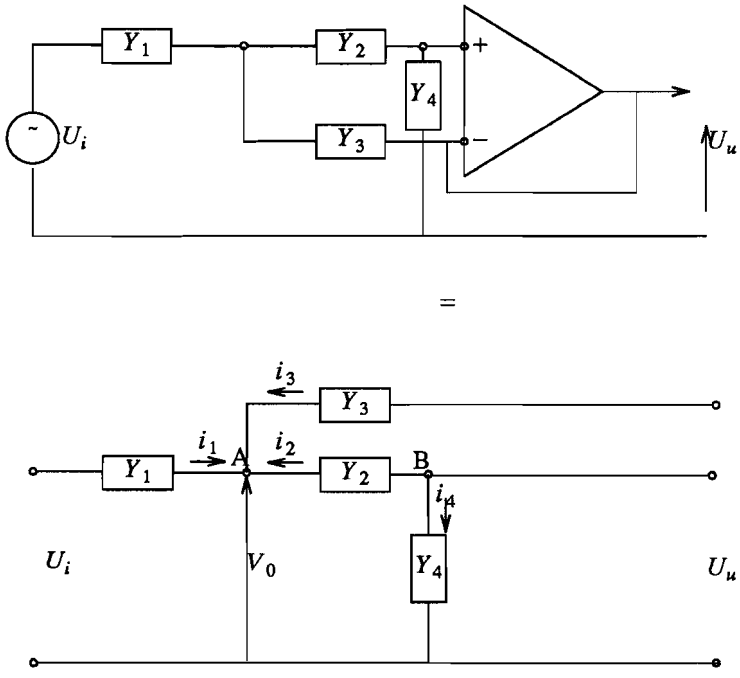

Figure A.1. Circuit diagram of a second order Butterworth filter.

For the voltages in figure A.1 we can write:

$$U_i - V_0 = \frac{i_1}{Y_1} \qquad U_u - V_0 = \frac{i_2}{Y_2}$$

$$U_u - V_0 = \frac{i_3}{Y_3} \qquad U_u = \frac{i_4}{Y_4} \tag{A.1}$$

and for the current distribution:

$$-i_2 = i_1 + i_3$$

$$i_2 = -i_4 \qquad \text{(A.2)}$$

Using (A.1) we can relate i_3 to i_2 :

$$i_3 = \frac{Y_3}{Y_2} i_2$$

and i_1 to i_2 with the aid of (A.2)

$$i_1 = -(1 + \frac{Y_3}{Y_2}) i_2 \qquad \text{(A.3)}$$

Now we can use (A.1) to relate U_u to U_i

$$U_u - U_i = i_2 (\frac{Y_1 + Y_2 + Y_3}{Y_1 Y_2})$$

Substitution of i_2

$$i_2 = -i_4 = \frac{-Y_4}{U_u}$$

finally leads to the response function:

$$\frac{U_u}{U_i} = \frac{Y_1 Y_2}{Y_1 Y_2 + Y_4 (Y_1 + Y_2 + Y_3)} \qquad \text{(A.4)}$$

APPENDIX B:
Optimization of a linear array using non-equidistant station location.

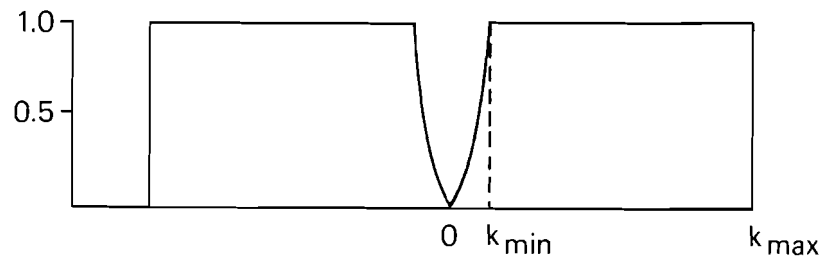

Figure B.1. Penalty function R(k)

In stead of putting weights to array stations or developing more sophisticated estimators, a manipulation that can be carried out in the research center, one can vary station location provided the array is in its design phase. We will use a slightly modified version of the penalty function used by Cara (1978), now minimized with respect to station location:

$$S(\Delta_1,.....,\Delta_n) = B\ \cos\theta + V\ \sin\theta$$

$$B = \int_0^{k_{min}} R(k)\ |H(k)|^2\, dk; \qquad R(k) = [\frac{k}{k_{min}}]^2, \quad k\ in\ [0,k_{min}]$$

$$V = \int_{k_{min}}^{k_{max}} R(k)\ |H(k)|^2\, dk; \qquad R(k) = 1\ , \quad k\ in\ [k_{min},k_{max}] \qquad \text{(B.1)}$$

where $H(k)$ stands for the array response function as a function of wavenumber k. Figure B.1 shows the penalty function R(k). If the interval of interest in higher mode analysis extends to $k_{max} > k_a$, the aliasing wavenumber, and the influence of the mainlobe is limited to k_{min} one can compute the penalty function S. Minimization of this function S with respect to station location will provide a more optimal array response.
For a better understanding of the behaviour of the penalty function we performed a simple excercise. In figure B.2 the array configuration has been modelled by means of two variables x1 and x2, using $x_3 = f(x_1,x_2)$ to keep the total array length constant (In this case for NARS: 2600 km).

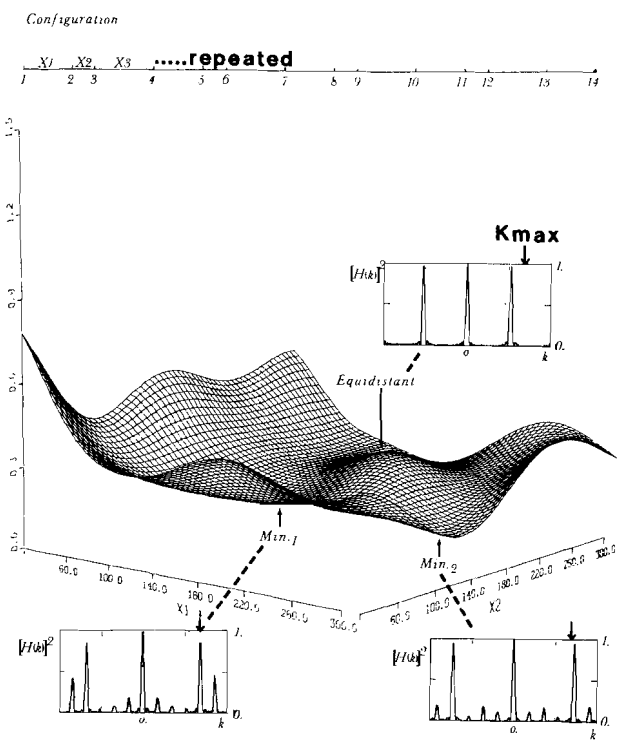

Figure B.2. Penalty function $S(\Delta_1, \ldots, \Delta_n)$ as a function of station separation parameters x_1 and x_2. For two minima and one maximum are the array response functions are plotted.

Clearly a local maximum in S is observed for equidistant spacing, showing aliasing lobes as large as the main lobe itself within the interval of interest. Three local minima are visible, each showing aliasing lobes removed from the specified interval. Furthermore we have been looking at a class of penalty functions in which θ and $k_{\min}$ were varied. The locations of the local minima didn't change, although a trade off between the minimum value of S and $k_{\min}$ exists. As θ goes from 0 to $\frac{\pi}{2}$ the minima become more pronounced. In conclusion we can say that the choise of non-equidistant station location in higher-mode surface wave analysis permits us to diminish the effects of spatial aliasing.

Appendix C:
NARS event catalogue

In this appendix we will present a list of all events recorded by the NARS array that are presently available on event tapes in GDSN format. In the last column the amount of stations that recorded these events is specified. These numbers include all triggers starting within one hour after the reported origin time.

Time	Latitude	Longitude	Depth	mb	nr of stations
1983 01 17 12:41: 29.2	38.092N	20.193E	9.	6.0	4
1983 01 24 08:17: 38.5	16.184N	95.149W	45.	6.3	5
1983 01 24 23:09: 21.5	12.952N	93.640E	79.	6.1	4
1983 01 26 16:02: 21.5	30.355S	179.427W	238.	6.1	5
1983 02 13 01:40: 13.1	39.945N	75.135E	16.	6.2	8
1983 02 14 03:20: 03.3	54.956N	159.191W	33.	5.8	6
1983 02 26 07:10: 59.1	49.231N	155.617E	57.	6.0	5
1983 03 12 01:36: 36.5	4.103S	127.918E	22.	6.0	4
1983 03 18 09:05: 50.0	4.857S	53.507E	88.	6.3	7
1983 03 23 23:51: 06.3	38.333N	20.215E	15.	5.6	7
1983 04 03 02:50: 00.6	8.731N	83.115W	33.	6.5	8
1983 04 04 02:51: 34.8	5.730N	94.811E	85.	6.5	8
1983 04 04 23:12: 47.0	49.399N	155.640E	50.	6.1	7
1983 04 12 12:07: 54.5	4.885S	78.183W	107.	6.5	7
1983 04 18 10:58: 47.8	27.721N	62.058E	37.	6.5	7
1983 04 30 14:03: 49.6	41.523N	143.780E	33.	6.5	6
1983 05 01 18:10: 41.5	46.356N	153.490E	33.	6.1	5
1983 05 02 23:42: 37.8	36.242N	120.300W	12.	6.1	3
1983 05 02 23:42: 37.8	36.242N	120.300W	12.	6.1	3
1983 05 14 23:13: 46.3	38.488N	20.347E	10.	5.0	5
1983 05 15 00:24: 00.5	18.888S	175.710W	36.	5.8	5
1983 05 26 02:59: 58.8	40.480N	139.090E	16.	7.6	6
1983 06 09 12:49: 04.1	40.200N	139.050E	33.	6.3	4
1983 06 21 06:25: 27.5	41.315N	139.136E	13.	6.6	8
1983 06 21 14:48: 5.5	24.253N	122.480E	24.	5.8	5
1983 06 24 09:06: 46.6	24.197N	122.430E	54.	6.0	6
1983 06 24 07:18: 21.9	21.723N	103.380E	18.	6.1	5
1983 07 03 17:14: 23.1	9.658N	83.644W	33.	5.6	5

Time	Latitude	Longitude	Depth	mb	nr of stations
1983 07 05 12:01: 27.3	40.329N	27.228E	10.	5.5	6
1983 07 11 12:56: 28.0	60.896S	52.935W	10.	6.1	6
1983 07 12 15:10: 03.3	61.033N	147.370W	37.	6.1	6
1983 08 06 15:43: 52.5	40.176N	24.728E	10.	6.3	4
1983 08 17 10:55: 52.8	55.786N	161.210E	55.	6.5	5
1983 08 25 20:23: 32.5	33.490N	131.420E	121.	6.1	5
1983 09 07 19:22: 04.8	60.982N	147.500W	42.	6.1	4
1983 09 12 15:42: 08.2	36.525N	71.118E	208.	6.1	4
1983 09 21 19:20: 42.8	24.118N	122.210E	33.	6.0	6
1983 10 04 18:52: 12.8	26.623S	70.767W	18.	6.3	6
1983 10 17 19:36: 21.3	37.616N	17.477W	10.	5.8	7
1983 10 22 04:21: 36.3	60.615S	25.439W	33.	6.3	4
1983 10 28 14:06: 06.3	44.046N	113.880W	10.	6.1	7
1983 10 30 04:12: 27.6	40.290N	42.171E	17.	6.1	7
1983 11 16 16:13: 00.0	19.433N	155.450W	11.	6.3	5
1983 11 24 05:30: 34.8	7.549S	128.240E	187.	6.1	8
1983 11 30 17:46: 00.4	6.888S	72.115E	10.	6.6	6
1983 12 02 03:09: 05.6	14.053N	91.940W	69.	5.8	8
1983 12 22 04:11: 29.2	11.950N	13.605W	10.	6.3	7
1983 12 30 23:52: 40.5	36.318N	70.740E	222.	6.6	10
1984 01 01 09:03:37.5	33.404N	137.320E	374.	6.5	3
1984 02 01 07:28:27.8	49.033N	146.610E	565.	6.0	4
1984 02 01 14:22: 07.6	34.681N	70.544E	33.	5.8	5
1984 02 07 21:33: 20.5	9.924S	160.450E	14.	6.5	11
1984 02 10 16:51: 21.0	28.333N	112.080W	10.	5.6	4
1984 02 11 08:02: 50.0	38.384N	22.066E	15.	5.3	6
1984 02 16 17:18: 42.5	36.422N	70.836E	218.	6.0	9
1984 03 05 03:33: 51.1	8.136N	123.760E	651.	6.6	9
1984 03 06 02:17: 21.0	29.362N	138.870E	457.	6.3	10
1984 03 19 20:28: 39.8	40.288N	63.333E	26.	6.5	11
1984 03 24 09:44: 02.5	44.162N	148.280E	43.	6.1	10
1984 03 27 20:06: 33.3	4.638S	145.844E	28.	5.6	6
1984 04 06 23:08: 23.2	18.933S	168.840E	190.	5.6	5
1984 04 20 06:31: 10.1	50.028N	148.760E	581.	6.0	4
1984 04 22 06:14: 21.6	0.522N	19.860W	10.	5.8	5
1984 04 23 21:40: 35.5	47.460N	146.720E	415.	6.0	5

Time	Latitude	Longitude	Depth	mb	nr of stations
1984 04 23 22:29: 58.3	22.044N	99.147E	17.	5.9	4
1984 04 24 04:11: 30.8	30.792N	138.360E	424.	6.1	5
1984 04 24 21:15: 19.0	37.320N	121.690W	8.	5.8	5
1984 04 29 05:02: 59.8	43.274N	12.571E	14.	5.1	6
1984 05 06 09:12: 01.6	38.817N	25.661E	10.	5.0	3
1984 05 07 17:49: 41.5	41.766N	13.886E	10.	5.5	7
1984 05 11 10:41: 49.8	41.832N	13.948E	13.	5.3	4
1984 05 13 12:45: 53.3	42.927N	17.731E	10.	5.1	5
1984 05 21 15:39: 00.5	32.671N	121.500E	33.	5.6	4
1984 05 26 03:58: 55.5	43.829S	39.142E	10.	5.6	4
1984 05 30 07:49: 43.5	4.878S	151.600E	175.	6.1	6
1984 06 11 02:05: 33.8	30.722S	71.214W	45.	6.1	5
1984 06 15 14:22: 23.0	15.790S	174.860W	247.	6.1	4
1984 06 21 10:43: 40.5	35.349N	23.291E	27.	5.6	8
1984 06 24 11:17: 12.0	17.993N	69.345W	25.	6.0	9
1984 06 24 14:30: 50.4	36.853N	3.768W	10.	4.6	5
1984 07 19 06:56: 11.0	52.912N	4.198W	20.	4.8	5
1984 07 19 23:25: 7.3	28.131N	129.530E	7.	6.1	3
1984 08 06 12:01: 54.1	0.115S	122.520E	260.	6.1	6
1984 08 06 19:06: 38.3	32.396N	131.800E	45.	6.2	6
1984 09 10 03:14: 08.8	40.346N	126.850W	10.	6.1	7
1984 09 14 23:48: 48.6	35.761N	137.480E	5.	6.1	8
1984 09 17 09:08: 52.6	32.068S	178.370W	33.	5.6	6
1984 09 18 17:02: 42.3	33.973N	141.440E	33.	6.6	10
1984 09 22 21:44: 18.3	32.012S	178.390W	58.	5.6	5
1984 09 28 00:03: 35.3	25.795S	176.010W	27.	6.3	8
1984 10 15 10:21: 07.5	15.737S	173.780W	129.	6.5	8
1984 10 26 20:22: 22.0	39.176N	71.340E	33.	6.0	7
1984 11 01 04:48: 49.8	8.147N	38.758W	10.	6.5	9
1984 11 20 08:15: 16.0	5.214N	125.240E	202.	6.3	5
1984 12 02 06:09: 44.0	20.423N	115.750W	10.	6.0	6
1984 12 03 04:08: 35.8	44.237N	148.140E	70.	6.3	9
1984 12 28 10:37: 53.6	56.174N	163.570E	33.	6.1	8
1985 02 28 20:53:47.8	27.462N	128.449E	60.	5.9	5
1985 03 01 17:11:17.5	2.082S	119.670E	17.	5.7	5
1985 03 02 15:47:33.4	1.964S	119.727E	44.	5.8	7

Time	Latitude	Longitude	Depth	mb	nr of stations
1985 03 03 22:47:7.2	33.135S	71.871W	33.	6.7	9
1985 03 04 00.32.21.8	33.207S	71.663W	33.	6.0	9
1985 03 04 03:32:49.1	32.925S	71.793W	33.	5.7	6
1985 03 05 13:40:10.2	1.192N	122.826E	33.	5.6	5
1985 03 09 14:08:4.3	66.239N	150.029W	12.	5.9	3
1985 03 13 19:34:57.6	43.510N	127.561W	10.	6.1	7
1985 03 16 14:54:0.7	17.013N	62.448W	13.	6.3	10
1985 03 17 10:41:38.4	32.633S	71.551W	33.	5.9	8
1985 03 18 19:49:45.8	7.758N	123.544E	33.	6.0	7
1985 03 19 04:01:8.0	33.198S	71.653W	42.	5.9	9
1985 03 25 05:14:35.1	34.254S	72.185W	45.	6.0	8
1985 03 28 16:07:06.8	40.310N	140.362E	166.	6.1	3
1985 04 03 13:06:20.2	32.584S	71.656W	33.	5.8	2
1985 04 09 01:56:59.4	34.131S	71.618W	38.	6.3	7
1985 04 19 17:43:10.8	11.848N	86.651W	72.	5.3	5
1985 04 19 17.55.34.6	11.766N	86.851W	60.	5.3	5
1985 04 20 18:23:48.0	9.004N	77.460W	38.	5.6	3
1985 04 23 16:15:12.0	15.344N	120.610E	188.	6.3	7
1985 04 24 01:07:14.5	16.498N	120.815E	33.	5.6	5
1985 04 30 18:14:12.7	39.266N	22.810E	27.	5.5	10
1985 05 01 13:27:56.1	9.196S	71.230W	600.	6.0	6
1985 05 02 08:55:16.3	48.871N	156.329E	43.	5.9	9
1985 05 06 03:04:22.7	30.885N	70.269E	37.	5.6	3
1985 05 09 19:05:21.5	51.465N	177.913E	33.	5.7	4
1985 05 10 15:35:50.5	5.599S	151.045E	27.	6.3	11
1985 05 14 13:24:57.8	10.610S	41.423E	10.	6.0	6
1985 05 14 18.11.08.9	10.562S	41.424E	10.	6.4	7
1985 05 15 20:12:45.8	56.637S	25.330W	33.	5.8	6
1985 05 16 14:20:25.1	29.081S	77.735E	10.	5.9	3
1985 05 19 08:07:48.2	53.611N	160.526E	63.	6.1	3
1985 05 19 18.09.15.6	30.253S	71.329W	39.	5.9	4
1985 05 20 15:11:40.6	35.489N	87.173E	33.	5.2	3
1985 05 31 07:24:34.1	12.246N	144.280E	32.	5.5	3
1985 06 03 02:45:32.0	13.175N	90.138W	66.	5.2	4
1985 06 03 12.06.21.1	15.289S	173.516W	33.	6.2	5
1985 06 06 02:40:12.9	0.932N	28.432W	10.	6.3	4

Time	Latitude	Longitude	Depth	mb	nr of stations
1985 06 10 15:37:03.3	28.112S	67.185W	180.	5.8	2
1985 06 12 17:22:52.2	24.485N	122.078E	33.	5.2	3
1985 07 03 04:36:52:4	4.463S	152.823E	41.	6.2	6
1985 07 22 09:26:52.1	6.281S	148.725E	33.	5.9	5
1985 07 28 22:59:54.5	60.312S	26.910W	33.	5.8	3
1985 07 29 07:54:44.3	36.186N	70.890E	101.	6.7	3
1985 08 02 07:46:51.4	36.173N	70.811E	103.	6.1	4
1985 08 04 02:36:23.6	7.445N	123.463E	35.	5.8	4
1985 08 11 00:19:02.4	11.157N	140.207E	33.	5.7	5
1985 08 12 00:04:50.9	38.420S	73.490W	33.	5.5	5
1985 08 12 03:49:17:9	37.739N	141.733E	51.	6.0	5
1985 08 15 04:28:47.1	47.051N	18.063E	10.	4.8	5
1985 08 21 11:26:28.8	9.211S	78.908W	61.	6.1	3
1985 08 23 12:41:59.7	39.423N	75.274E	33.	6.4	9
1985 08 28 20:50:48.4	21.012S	179.011W	625.	5.9	4
1985 09 10 04:07:50.1	6.450S	149.888E	33.	5.7	5
1985 09 11 20:45:51:7	39.328N	75.416E	33.	5.8	5
1985 09 15 07:57:53.7	17.975N	97.183W	67.	5.9	2
1985 09 19 13:17:47.8	18.182N	102.573W	33.	7.0	9
1985 09 21 01:37:13.8	17.823N	101.671W	33.	6.3	11
1985 09 26 07:27:48.9	34.627S	178.694W	33.	6.5	10
1985 09 27 03:39:08.2	09.805S	159.844E	30.	6.3	8
1985 09 27 10:10:19:6	21.944S	174.804W	33.	5.8	3
1985 09 27 16:39:48:6	34.507N	26.588E	59.	5.5	4
1985 10 05 15:24:02.2	62.257N	124.312W	10.	6.5	7
1985 10 09 09:33:32.8	54.801N	159.573W	31.	6.3	8
1985 10 12 22:20:37.6	0.857NS	29.876W	10.	5.3	8
1985 10 13 15:59:53.5	40.317N	69.840E	33.	5.8	6
1985 10 18 04:19:08.3	46.300N	146.287E	291.	6.0	2
1985 10 27 19:34:57.0	36.402N	6.746E	10.	5.5	8
1985 10 29 13:13:42.7	36.720N	54.805E	33.	6.0	4
1985 10 29 14:10:39:5	9.564S	150.992E	10.	6.0	3
1985 10 31 19:33:07.1	53.258N	166.924W	33.	5.8	2
1985 10 31 21:49:20:0	28.747S	63.186W	595.	5.8	3
1985 11 07 19:12:29.8	35.198S	179.357W	33.	6.2	6
1985 11 17 09:40:21.7	1.591S	135.012E	13.	5.9	6

Time	Latitude	Longitude	Depth	mb	nr of stations
1985 11 21 21:57:14.9	41.720N	19.320E	22.	5.4	4
1985 11 28 02:25:42.5	13.976S	166.209E	33.	5.9	6
1985 11 28 03:49:54:1	13.932S	166.167E	33.	5.8	6
1985 12 14 06:46:13.3	3.651N	126.699E	33.	5.7	3
1985 12 16 02:44:35.6	11.719N	85.854W	21.	5.9	6
1985 12 16 08:04:06:1	14.153S	166.356E	33.	6.0	7
1985 12 21 01:13:21.0	14.035S	166.508E	33.	6.1	8
1985 12 23 05:16:03.9	62.207N	124.302W	10.	6.4	7
1986 01 15 20:17:31.4	21.376S	170.284E	145.	6.1	8
1986 02 03 20:47:35.8	27.889N	139.402E	516.	5.7	3
1986 02 07 03:54:58.6	45.408N	27.865W	10.	4.9	3
1986 02 10 18:33:46.7	39.521N	143.186E	33.	5.5	5
1986 02 12 02:59:31.8	36.352N	140.932E	44.	6.0	3
1986 02 21 05:39:56.6	43.346N	25.954E	25.	4.7	5
1986 02 27 06:23:12.4	24.069N	122.303E	33.	5.8	3
1986 03 03 01:24:05.7	41.945N	20.265E	23.	5.0	3
1986 03 06 00:05:38.3	40.393N	51.534E	33.	6.2	5

APPENDIX D
Dataset used in inversion.

Rayleigh wave phase velocity measurements (in km/s)

mode 0

T [s]	26/5/83	21/6/83	22/12/83	24/3/84	18/9/84	**mean**	**st. dev.**
160.00	4.34	4.34	-	4.27	-	**4.32**	**.03**
142.22	4.24	4.24	-	-	-	**4.24**	**-**
128.00	4.21	4.17	-	4.13	-	**4.17**	**.03**
116.36	4.15	4.14	-	4.14	-	**4.14**	**.01**
106.67	4.12	4.11	-	-	4.12	**4.12**	**.01**
98.46	4.09	4.08	-	4.08	-	**4.08**	**.01**
91.43	4.06	4.03	-	4.04	4.04	**4.04**	**.01**
80.00	3.99	3.96	4.04	4.01	4.03	**4.01**	**.02**
75.29	3.99	3.98	4.01	4.02	4.01	**4.00**	**.01**
71.11	3.99	3.98	4.00	4.01	4.01	**4.00**	**.01**
67.37	3.99	3.98	-	4.01	4.00	**4.00**	**.01**
64.00	3.98	3.96	3.97	4.02	4.01	**3.99**	**.01**
60.95	3.99	3.95	-	4.02	3.98	**3.99**	**.02**
58.18	3.98	3.95	3.95	4.02	3.96	**3.97**	**.02**
53.33	3.95	3.95	3.95	3.99	3.93	**3.95**	**.01**
49.23	3.96	3.95	3.95	3.96	3.93	**3.95**	**.01**
45.71	3.94	3.94	3.95	3.95	3.92	**3.94**	**.01**
42.67	3.93	3.94	3.94	-	-	**3.94**	**.01**
40.00	3.92	3.92	3.92	3.96	3.92	**3.93**	**.01**
37.65	3.89	3.91	3.91	3.92	3.88	**3.90**	**.01**
35.56	3.88	3.89	3.90	3.90	3.86	**3.89**	**.01**
33.68	3.86	3.89	3.87	3.88	3.84	**3.87**	**.01**
32.00	3.87	3.88	3.85	3.85	3.83	**3.86**	**.01**
30.47	-	3.87	3.85	3.83	3.82	**3.84**	**.01**
29.09	3.83	3.85	3.83	-	3.80	**3.83**	**.01**
27.83	3.78	3.82	3.81	3.81	3.78	**3.80**	**.01**
26.67	3.75	3.80	3.79	3.78	3.75	**3.77**	**.01**
25.60	3.70	3.76	3.77	3.75	3.72	**3.74**	**.02**
24.62	3.68	3.73	3.73	3.72	3.70	**3.71**	**.01**
23.70	3.65	3.70	3.70	3.69	-	**3.69**	**.01**
22.86	3.62	3.66	3.66	-	-	**3.65**	**.02**

mode 1

T [s]	21/6/83	22/12/83	6/3/84	24/3/84	18/9/84	21/6+26/5/83	mean	st. dev.
45.71	4.98	4.95	-	4.84	4.98	4.99	**4.94**	**.04**
42.67	4.94	4.90	-	4.77	4.84	4.98	**4.87**	**.05**
40.00	4.90	4.83	-	4.72	4.75	4.77	**4.77**	**.03**
37.65	4.89	4.81	4.80	4.68	-	4.71	**4.75**	**.04**
35.56	4.81	-	4.76	4.67	4.64	4.69	**4.69**	**.03**
33.68	-	-	4.72	-	-	-	**4.72**	**-**
32.00	-	-	4.65	-	-	-	**4.65**	**-**
30.47	-	-	4.59	-	-	-	**4.59**	**-**
29.09	-	-	4.58	4.54	4.65	-	**4.59**	**.04**
27.83	-	-	4.60	4.55	4.60	-	**4.58**	**.03**
26.67	4.65	-	-	4.53	4.57	-	**4.58**	**.05**
25.60	-	-	-	4.56	4.57	-	**4.57**	**.01**
24.62	-	-	-	-	4.53	-	**4.53**	**-**
23.70	-	4.53	-	4.52	4.52	-	**4.52**	**.01**
22.86	4.49	4.47	-	-	4.51	-	**4.49**	**.02**

mode 2

T [s]	21/6/83	22/12/83	6/3/84	24/3/84	18/9/84	21/6+26/5/83	mean	st. dev.
45.71	5.62	-	-	5.42	5.40	5.66	**5.49**	**.11**
42.67	5.53	-	-	5.39	5.35	5.51	**5.42**	**.06**
40.00	5.47	-	-	5.35	5.31	5.40	**5.35**	**.03**
37.65	5.40	5.41	5.29	5.28	5.29	5.30	**5.31**	**.03**
35.56	5.33	-	5.24	5.20	5.27	5.19	**5.23**	**.02**
33.68	-	-	5.18	5.15	5.19	-	**5.17**	**.02**
32.00	-	-	5.16	5.09	5.13	-	**5.13**	**.03**
30.47	-	-	5.11	-	-	-	**5.11**	**-**
29.09	-	-	5.09	5.02	4.99	5.02	**5.03**	**.03**
27.83	4.98	-	5.06	4.99	4.94	4.89	**4.97**	**.04**
26.67	4.94	4.86	5.04	4.98	4.90	-	**4.94**	**.04**
25.60	4.91	-	-	4.93	-	-	**4.92**	**.02**
24.62	4.86	4.79	-	4.87	4.80	-	**4.83**	**.02**
23.70	4.84	-	4.90	4.82	4.75	-	**4.83**	**.04**
22.86	4.77	4.77	4.81	4.80	-	-	**4.79**	**.01**
21.33	-	4.76	-	4.76	-	-	**4.76**	**-**
20.00	-	4.69	-	4.70	4.65	-	**4.68**	**.02**
18.82	-	-	-	4.66	4.62	-	**4.64**	**.04**
17.78	-	-	-	4.63	4.60	-	**4.62**	**.03**
16.84	-	-	-	4.59	-	-	**4.59**	**-**

mode 3

T [s]	21/6/83	22/12/83	6/3/84	24/3/84	18/9/84	**mean**	**st. dev.**
45.71	6.30	-	6.32	6.19	6.24	**6.26**	**.04**
42.67	6.20	-	6.07	6.00	6.02	**6.07**	**.05**
40.00	6.04	-	5.96	5.82	-	**5.94**	**.09**
35.56	-	-	5.63	5.73	5.73	**5.70**	**.04**
33.68	-	-	5.61	5.62	5.57	**5.60**	**.02**
32.00	-	5.65	5.56	5.54	5.48	**5.56**	**.04**
30.47	-	5.47	5.51	-	-	**5.49**	**.04**
29.09	5.36	5.39	5.43	5.41	-	**5.40**	**.02**
27.83	5.30	5.36	5.42	5.36	-	**5.36**	**.03**
26.67	5.28	5.30	5.37	5.32	5.27	**5.31**	**.02**
25.60	5.23	-	5.31	5.26	-	**5.27**	**.03**
24.62	5.16	5.17	5.30	-	5.13	**5.19**	**.05**
23.70	5.12	5.14	-	-	-	**5.13**	**.02**
22.86	5.10	4.99	-	5.08	5.07	**5.06**	**.03**
21.33	-	4.97	5.00	-	4.98	**4.98**	**.01**
20.00	-	-	-	4.97	4.92	**4.95**	**.05**
16.84	-	4.79	-	4.85	-	**4.82**	**.05**

mode 4

T [s]	21/6/83	22/12/83	6/3/84	24/3/84	18/9/84	**mean**	**st. dev.**
17.78	5.06	5.04	-	-	5.12	**5.07**	**.03**
16.84	5.03	5.00	5.09	5.10	5.06	**5.08**	**.04**
16.00	5.00	-	5.06	-	-	**5.03**	**.05**
15.24	-	-	5.03	4.99	4.98	**5.00**	**.02**

mode 5

T [s]	21/6/83	22/12/83	6/3/84	24/3/84	18/9/84	**mean**	**st. dev.**
33.68	-	-	6.38	6.42	6.50	**6.43**	**.05**
32.00	-	-	6.37	6.36	6.40	**6.38**	**.02**
30.47	-	-	6.23	6.24	6.26	**6.24**	**.01**
29.09	-	-	6.11	6.14	-	**6.13**	**.03**
22.86	5.92	6.00	5.94	5.90	5.90	**5.93**	**.02**
21.33	5.79	5.89	-	5.79	5.77	**5.81**	**.03**
20.00	-	5.74	5.68	5.67	5.67	**5.69**	**.02**

mode 6

T [s]	21/6/83	22/12/83	6/3/84	24/3/84	18/9/84	**mean**	**st. dev.**
40.00	7.09	7.10	7.18	7.19	7.29	**7.17**	**.04**
37.65	7.06	7.07	-	7.17	7.25	**7.14**	**.05**
35.56	7.01	-	-	7.16	7.18	**7.12**	**.07**
33.68	6.96	7.03	7.07	7.10	7.07	**7.05**	**.03**
32.00	6.86	6.93	6.95	7.02	6.91	**6.93**	**.03**
30.47	6.74	6.83	6.81	6.75	6.71	**6.77**	**.03**
29.09	6.58	6.74	6.70	6.57	6.64	**6.65**	**.04**
27.83	6.53	6.58	6.58	6.49	6.40	**6.52**	**.04**
26.67	-	6.40	6.47	-	-	**6.44**	**.04**
23.70	6.46	-	-	6.23	6.37	**6.35**	**.09**
22.86	6.34	-	-	6.27	6.31	**6.31**	**.03**
21.33	6.20	6.26	-	6.18	6.17	**6.20**	**.02**
18.82	6.01	6.05	-	6.04	6.00	**6.03**	**.01**
17.78	5.89	5.91	5.93	-	5.91	**5.91**	**.01**
16.84	5.77	5.79	5.83	5.89	-	**5.82**	**.03**
16.00	5.72	-	5.75	-	-	**5.74**	**.03**
15.24	-	-	5.68	-	5.72	**5.70**	**.04**

Love wave phase velocity measurements (in km/s)
for event 24/3/84 (84) and 18/9/84 (262).

T [s]	*mode 0*		*mode 1*		*mode 2*		*mode 3*	
	84	262	84	262	84	262	84	262
106.67	-	4.63						
98.46	4.65	4.60						
91.43	4.62	-						
85.33	4.58	4.61						
80.00	4.56	4.59						
75.29	4.56	-						
71.11	4.55	4.58						
67.37	4.54	4.56						
64.00	4.57	-						
60.95	4.58	4.50						
58.18	4.55	4.47						
53.33	4.53	4.43						
49.23	4.51	-						
47.07	-	4.38						
45.71	4.50	4.36	4.97	4.99	5.56	-	6.38	-
42.67	4.48	4.32	4.92	4.94	5.42	5.40	-	6.06
40.00	4.41	4.56	4.94	4.83	-	-	5.83	5.82
37.65	4.37	4.47	4.94	4.76	-	5.23	5.71	5.69
35.56	4.32	4.40	4.91	4.72	-	5.16	5.61	-
33.68	4.28	4.33	4.89	4.71	-	5.11	5.54	-
32.00	4.24	4.28	-	4.70	-	-	5.48	-
30.47	-	-	4.67	-	4.98	-	-	-
29.09	4.17	4.15	4.67	4.69	4.93	5.03	5.37	-
27.83	4.13	4.14	4.68	4.69	4.89	4.98	5.31	-
26.67	4.09	4.12	4.65	4.67	4.88	4.95	-	5.26
25.60	4.05	4.10	4.62	4.64	4.87	4.91	-	5.22
24.62	4.03	4.08	4.60	4.62	-	4.89	5.18	5.19
23.70	4.00	4.06	4.59	4.61	4.82	4.83	5.15	5.17
22.86	-	-	-	4.59	-	-	5.14	5.13

Sn traveltime dataset used in inversion.

Δ [*rad*]	T [s]
.0524	82.4
.0698	107.2
.0873	130.4
.1047	153.9
.1222	177.6
.1396	201.5
.1571	225.5
.1745	249.6
.1920	272.8
.2094	296.0
.2269	319.2
.2443	342.4
.2690	375.8

REFERENCES

Agnew, D. C., Berger J., Farrell, W. E., Gilbert, J. F., Masters, G. and Miller, D., 1986. Project IDA, a decade in review. *EOS, Trans. Am. Geophys. Union*, **67**, 203-219.

Akaogi, M. and Akimoto, S., 1977. Pyroxene-garnet solid solution equilibria in the system $Mg_4Si_4O_{12} - Mg_3Al_2Si_3O_{12}$ and $Fe_4Si_4O_{12} - Fe_3Al_2Si_3O_{12}$ at pressures and temperatures. *Phys. Earth Planet. Inter.*, **15**, 90-106.

Akaogi, M. and Akimoto S., 1979. High-pressure phase equilibria in a garnet lherzolite, with special reference to Mg^{2+}-Fe^{2+} partitioning among constituent minerals *Phys. Earth Planet. Inter.*, **19** 31-51.

Aki, K. and P. Richards, 1980. Quantitative Seismology, Theory and Methods. W.H. Freeman, San Francisco.

Anderson, D. L., 1979a. The upper mantle transition region: eclogite? *Geophys. Res. Lett.*, **6**, 433-436.

Anderson, D.L., 1979b. The deep structure of continents. *J. Geoph. Res.*, **84**, 7555-7560.

Anderson, D. L. and Bass J. D., 1984 Mineralogy and composition of the upper mantle *Geophys. Res. Lett.*, **11**, 637-640

Anderson, D. L. and Bass J.D., 1986. Transition region of the Earth's upper mantle. *Nature*, **320**, 321-328.

Bass, J. D. and Anderson D. L., 1984. Composition of the upper mantle: geophysical tests of two petrological models. *Geophys. Res. Lett.*, **11**, 237-240.

Bina, G. R. and Wood B. J., 1984. The eclogite to garnetite transition -- experimental and thermodynamic constraints. *Geophys. Res. Lett.*, **11**, 955-958.

Byrne, C. L. and Fitzgerald R. M., 1982. Reconstruction from partial information, with applications to tomography. *SIAM J. Appl. Math.*, **42**, 933-940.

Byrne, C. L. and Fitzgerald R. M., 1984. Spectral estimators that extend the maximum likelihood methods. *SIAM J. Appl. Math.*, **44**, 425-442.

Calcagnile, G., 1982. The lithosphere-asthenosphere system in Fennoscandia. *Tectonophysics*, **90**, 19-35.

Cara, M., 1978. Regional variations of higher Rayleigh mode phase velocities, a spatial filtering method. *Geophys. J. R. Astron. Soc.*, **54**, 439-460.

Cara, M., Nercessian, A. and Nolet, G., 1980. New inferences from higher mode data in Western Europe and Northern Eurasia. *Geophys. J. R. Astron. Soc.*, **61**, 459-478.

Dost, B., A. van Wettum and G. Nolet, 1984. The NARS array. *Geol. Mijnbouw*, **63**, 381-386.

Dost, B., 1986. Preliminary results from higher-mode surface-wave measurements in western europe using the NARS array. *Tectonophysics*, **128**, 289-301.

Dziewonski, A.M. and D.L. Anderson, 1981. Preliminary reference Earth model. *Phys. Earth Planet. Inter.*, **25**, 297-356.

Anonymus, 1981. Universele tijdsein processor. *Elektuur* **215**, 950-960.

Grand, S.P. and Helmberger, D.V., 1984. Upper mantle shear structure of North America. *Geophys. J. R. Astron. Soc.*, **76**, 399-438.

Hoffman, J.P., 1980. The Global Digital Seismograph Network Day Tape. *USGS open file report*, 80-289.

Irifune, T., Sekine T., Ringwood A.E. and Hibberson, W.O., 1986. The eclogite-garnetite transformation at high pressure and some geophysical implications. *Earth Plan. Sc. Lett.* **77** 245-256.

IRIS, 1984a. Science plan for a new global seismograph network. *report, IRIS inc.* Washington, D.C.

IRIS, 1984b. Program for Array Seismic Studies of the Continental lithosphere (PASSCAL). *report, IRIS inc.* Washington, D.C.

Jarosh, H. and A.R. Curtis, 1973. A note on the calibration of the electromagnetic seismograph. *Bull. Seism. Soc. America*, **63**, 1145-1155.

Jeanloz, R., and Thompson A. B., 1983. Phase transitions and mantle discontinuities. *Rev. Geophys. Space Phys.*, **21**, 51-74,

Jordan, T. H., 1975. The continental tectosphere., *Rev. Geophys. Space Phys.*, **13**, 1-12.

Jordan, T. H., 1978. Composition and development of the continental tectosphere. *Nature.*, **274**, 544-548.

Jordan, T. H., 1981. Continents as a chemical boundary layer. *Phil. Trans. R. Soc. Lond.*, b A301 , 359-373.

Kennett, B. L. N., 1985. On regional S. *Bull. Seism. Soc. America*, **75**, 1077-1086.

Lees, A. C., Bukowinski M. S. T. and Jeanloz R., 1983. Reflection properties of phase transition and compositional change models of the 670 km discontinuity, *J. Geoph. Res.*, **88**, 8145-8159,

Lehmann, I., 1961. S and the structure of the upper mantle *Geophys. J. R. Astron. Soc.*, **4**, 124-138.

Lerner-Lam, A. L. and Jordan, T. H., 1983. Earth structure from fundamental and higher-mode waveform analysis. *Geophys. J. R. Astron. Soc.*, **75**, 759-798.

Lerner-Lam, A. L., 1985. Tradeoff between lid thickness and anisotropy using linearized waveform inversion. *EOS, Trans. Am. Geophys. Union*, **66**, 966-967. (Abstract).

Leven, J.H., 1985. The application of synthetic seismograms to the interpretation of the upper mantle P-wave velocity structure in northern Australia. *Phys. Earth Planet. Inter.*, **38**, 9-27.

Leveque, J-J. and Cara, M., 1983. Long-period Love wave overtone data in North America and the Pacific Ocean: new evidence for upper mantle anisotropy. *Phys. Earth Planet. Inter.*, **33**, 164-179.

Liu, L., 1980. The mineralogy of an eclogitic earth mantle. *Phys. Earth Planet. Inter.*, **23**, 262-267.

Malin, P. E. and Phinney R. A., 1985. On the relative scattering of P- and S- waves.

Geophys. J. R. Astron. Soc., **80**, 603-618.

Mantovani, E., Schwab, F., Liao, H. and Knopoff, L., 1977. Teleseismic Sn: a guided wave in the mantle. *Geophys. J. R. Astron. Soc.*, **51**, 709-726.

Mayer-Rosa, D. and Mueller, St., 1973. The gross velocity-depth distribution of P and S waves in the Upper Mantle of Europe from earthquake observations. *Z. Geophys.*, **39**, 395-410.

Michette, A. G., Darling, A. M., Fiddy, M. A., Ward, W. A. and Franklin E., 1984. Resolution enhancement of Well log and Seismic data. *Geophys. Prosp.*, **32**, 564-580.

Mitchell, B. J., 1984. On the inversion of Love and Rayleigh-wave dispersion and implications for Earth structure and anisotropy. *Geophys. J. R. Astron. Soc.*, **76**, 233-242.

Moore R.O. and Gurney, J. J., 1985. Pyroxene solid solution in garnets included in diamond. *Nature*, **318**, 553-555.

Nakada, M. and Hashizume, M., 1983. Upper mantle structure beneath the canadian shield derived from higher modes of surface waves. *J. Phys. Earth.*, **31**, 387-405.

Nolet, G., 1975. Higher Rayleigh modes in Western Europe. *Geophys. Res. Lett.*, **2**, 60-62.

Nolet, G., 1976. Higher modes and the determination of upper mantle structure. *Ph-D Thesis*, Utrecht, 90pp.

Nolet, G. and Panza, G. F., 1976. Array analysis of seismic surface waves, limits and possibilities. *Pure appl. Geophys.*, **114**, 775-790.

Nolet, G., 1977. The upper mantle under Western Europe inferred from the dispersion of Rayleigh modes. *Z. Geophys.*, **43**, 265-286.

Nolet, G. and Vlaar, N. J., 1982. The NARS project, Probing the Earth with a large seismic antenna. *Terra Cognita*, **2**, 17-25.

Nolet, G., Dost, B. and Paulssen H., 1986a. Intermediate wavelength seismology and the NARS experiment. *Ann. Geoph.*, **4**, 305-314.

Nolet, G., Dost, B. and Paulssen H., 1986b. The upper mantle under Europe: an interpretation of some preliminary results from the NARS project. *Geol. Mijnbouw*, **65**, 155-165.

Nolet, G., Romanovicz, B.,Kind, R. and E. Wielandt. 1986c. ORFEUS science plan, Reidel, Dordrecht, 45pp.

Nolet, G., van Trier, J. and Huisman, R., 1986d. A formalism for nonlinear inversion of seismic surface waves., *Geophys. Res. Lett.*, **13**, 26-29.

Oldenburg, D. W., 1981. A comprehensive solution to the linear deconvolution problem. *Geophys. J. R. Astron. Soc.*, **65**, 331-358.

Oxburgh, E.R., 1980. Mantle Mineralogy and Dynamics, in *Proceedings of the Enrico Fermi International School of Physics* **LXXVIII**, 247-269, eds. Dziewonski, A. and Boschi, E., North Holland.

Panza, G. F., Mueller, St. and Calcagnile, G., 1980. The Gross Features of the Lithosphere-Asthenosphere System in Europe from Seismic Surface Waves and Body Waves.,

Pageoph., **118**, 1209-1213.

Panza, G. F., Schwab, F. A. and Knopoff, L., 1973. Multimode Surface Waves for Selected Focal Mechanisms 1. Dip-Slip Sources on a Vertical Fault Plane *Geophys. J. R. Astron. Soc.*, **34**, 265-278.

Papoulis, A., 1975. A new algorithm in spectral analysis and band-limited extrapolation. *IEEE Trans. Circuits and Systems, CAS-22*, **4**, 735-742.

Paulssen, H., 1987. Lateral heterogeneity of Europe's upper mantle by body wave modelling. Submitted to *Geophys. J. R. Astron. Soc.*,

Prothero W.A., 1980. Earthquake signal processing and logging with a battery powered microcomputer. *Bull. Seism. Soc. America*, **70**, 2275-2290.

Rasson, J. and F. de Meyer., 1983. Calibration of long period seismic channels. *Inst. Roy. Meteor. Belg., Publ. Ser. A* **110**, 49pp.

Ringwood, A.E., 1975. Composition and petrology of the Earth's mantle. *McGraw-Hill (New York)*, 618 pp.

Ringwood, A.E., 1979. Origin of the Earth and Moon. *Springer-Verlag (New-York)*, 295 pp.

Ringwood, A. E., 1982. Phase transformations and differentiation in subducted lithosphere: implications for mantle dynamics, basalt petrogenesis and crustal evolution. *J. Geology*, **90**, 611-643.

Robinson, E.A. and Treitel S., 1980. Geophysical signal analysis. *Prentice Hall, inc*, 466 pp.

Sawamoto, H., 1986. Single crystal growth of the modified spinel (β) and spinel (γ) phases of $(Mg,Fe)_2SiO_4$ and some geophysical implications. *Phys. Chem. Minerals*, **13**, 1-10.

Schwartz U. J., 1978. Mathematical-statistical description of the iterative beam removing technique (method CLEAN). *Astron. Astrophys.*, **65**, 345-356.

Seidl, D., 1971. Spezielle Probleme der Ausbreitung Seismischer Oberflachenwellen mit Beobachtungsbeispielen aus Europa. *Ph. D. Thesis.*, Karlsruhe.

Seidl, D. and Stammler W., 1984. Restoration of broad band seismograms 1. *Z. Geophys.*, **54**, 114-122.

Sipkin, S. A. and Jordan T. H., 1975. Lateral heterogeneity of the upper mantle determined from travel times of ScS. *J. Geoph. Res.*, **80**, 1474-1484.

Sipkin, S. A. and Jordan T. H., 1976. Lateral heterogeneity of the upper mantle determined from the travel times of multiple ScS. *J. Geoph. Res.*, **81**, 6307-6320,

Sipkin, S. A. and Jordan, T. H., 1980. Multiple ScS travel times in the western Pacific: Implications for mantle heterogeneity. *J. Geoph. Res.*, **85**, 853-861.

Snieder, R., 1986. 3D linearized scattering of surface waves and a formalism for surface wave holography. *Geophys. J. R. Astron. Soc.*, **84**, 581-605.

Spakman, W., 1986. Subduction beneath Eurasia in connection with the mesozoic Tethys. *Geol. Mijnbouw*, **65**, 145-153.

Vlaar, N.J., 1982. Lithospheric doubling as a cause of intra-continental tectonics. *Proc. Roy. Neth. Ac. Sc.* **B85**, 469-483.

Vlaar, N.J., 1983. Thermal anomalies and magmatism due to lithospheric doubling and shifting. *Earth Plan. Sc. Lett.* **65**, 322-330.

Vlaar, N. J. and Cloetingh S. A. P. L., 1984. Orogeny and ophiolites: plate tectonics revisted with reference to the Alps, *Geol. Mijnbouw*, **63**, 159-164,

Weidner D.J., 1985. A mineral physics test of a pyrolite mantle. *Geophys. Res. Lett.*, **12**, 417-420.

Weidner D.J., 1986. Mantle model based on measured physical properties of minerals. (preprint).

Wielandt, E. and Knopoff, L., 1982. Dispersion of Very Long-Period Rayleigh Waves along the East-Pacific Rise: Evidence for S wave velocity anomalies to 450 km depth. *J. Geoph. Res.*, **87**, 8631-8641.

Wielandt, E. and W. Mitronovas.,1976. An electronic long period seismograph for surface wave dispersion studies. *Bull. Seism. Soc. America*, **66**, 987-996.

Willmore, P.L.,1979. Manual of Seismological Observatory Practice- World Data Centre A for Solid Earth Geophysics. 165pp.

Wiggins, R.A., 1972. The general linear inverse problem: Implication of surface waves and free oscillations for Earth structure. *Rev. Geophys. Space Phys.*, **10**, 251-285.

ACKNOWLEDGEMENTS

Een ieder die heeft bijgedragen aan de opzet en uitvoering van het NARS experiment en de totstandkoming van dit proefschrift ben ik veel dank verschuldigd.

In de eerste plaats mijn promotor Professor Guust Nolet, die NARS in samenwerking met Professor N.J. Vlaar heeft opgezet, voor de vele stimulerende discussies en zeer aktieve betrokkenheid bij de uitvoering van NARS.

Professor N.J. Vlaar voor zijn grote inzet bij het opbouwen van de vakgroep.

Arie van Wettum, wiens technische kennis, inzet en goed humeur van essentieel belang waren voor het slagen van het NARS project.

The assistance of Dr. Wielandt in the design of the NARS instrumentation has been of great importance.

Mijn overige collega's, in het bijzonder Hanneke Paulssen met wie ik drie jaar lang de kamer deelde. Zij nam een substantieel deel van de dataverwerking voor haar rekening. Gordon Shudofsky bedank ik voor zijn hulp bij de data conversie. Roel Snieder heeft nuttige suggesties voor verbeteringen van het manuscript aangedragen.

Hoewel de laserprinter een uitkomst was heeft De Pattynama steeds geholpen bij de administratie van NARS.

Vele student-assistenten heben geholpen met de dataverwerking, onder wie Reina Huisman, Jos van Trier en Vincent Nijhof.

Discussies met Hein Haak over de instrumentatie, zijn hulp bij het zoeken van lokaties in Groningen en de gastvrijheid van zijn gezin werden zeer gewaardeerd.

Ko van Gend en Wim Zenden van het KNMI waren zeer behulpzaam bij het verzamelen van gegevens omtrent recente aardbevingen.

I like to acknowledge the work and generous hospitality of all station managers. Several institutions in Europe offered us their help in finding station locations and facilitated the communication between station managers and the data center. Of crucial importance was the generous offer from the ministry of foreign affairs, represented by Mr. J.A.S. Kleefstra, that we could rely on the cooperation of Dutch Embassies in clearing the customs problems. A list of people that were involved is given on the next page.

Mijn ouders hebben mij steeds gestimuleerd om te studeren, waarvoor mijn dank.

Sweden:	Dr. G. Lind (Chalmers University), M. Jansen (Embassy)
Denmark:	J. Sorensen, V.A. Glargaard, E. Jensen (Aarhus university) Dr. S. Gregersen (Geodaetisk institute Charlottelund) and J.C. Henneman (Embassy).
Netherlands:	L. Beuving, T. Jipping, P.J.M. Wit (all KNMI) and F.L.M.V. Bergsteijn.
Belgium:	Dr. J. Rasson (Institut Physique du Globe, Dourbes), W.J.J.D. Baron thoe Schwartzenberg, H. Heijnen, R.C. Hoffmann and C Wels (all at the Embassy).
France:	A. Simonin (IPG, Paris), M. Vadell (IPG, Toulouse), J-H Pelletier, J. Fourvel, J. Esprabens, J. Bouillon, Dr. R. and B. Darchen, M. Bages, Dr. J. Dorel (IPG, Clermont-Ferrand), Prof. N. Jobert and Prof. R. Madariaga (both IPG, Paris). R.J.M. Engels and Mw. Smit (both at the Embassy).
Spain:	M.A. and M-J Bordeje Muguerza, G. Cremades, M. Diez, D. Hergueta, Dr. M. Herraiz and Prof. A. Udias (both at University Complutense de Madrid), Prof. Lopes-Arroyo (Instituto Geographico National), Dr.'s G. Alguacil, J.M. Guirao, F. de Miguel, G. Olivares and Prof. F. Vidal-Sanchez (all at University de Cartuja, Granada).

NARS is mogelijk gemaakt mede door de financiele steun van de stichting AWON, de aardwetenschappelijke tak van de Nederlandse Organisatie voor Zuiver Wetenschappelijk Onderzoek (ZWO) en van het Koninklijke Shell Exploratie en Productie Laboratorium.

CURRICULM VITAE

Bernard Dost werd geboren op 15 januari 1956 te Haarlem. In deze stad behaalde hij in 1974 het diploma Gymnasium β aan het Karel van Mander lyceum. In september van ditzelfde jaar werd begonnen met de studie Geologie (G4) aan de Rijksuniversiteit Utrecht. Het kandidaatsexamen G4 legde hij af in juni 1977, gevolgd door het doctoraalexamen Geofysica met bijvakken numerieke Wiskunde en Sedimentologie in december 1980. Van 1977 tot en met 1980 vervulde hij student-assistentschappen bij de afdelingen theoretische en exploratie Geofysica. Hij was wetenschappelijk assistent in dienst van de Rijksuniversiteit Utrecht bij de afdeling theoretische Geofysica van januari 1981 tot en met december 1986. Vanaf 1 januari is hij manager van het ORFEUS Data Centrum.